Multi-modal Data Synthesis from Organotypic Whole Hemisphere Brain Slice Models to Investigate Cellular-Extracellular Interactions

Nels Wightman Schimek

A dissertation

submitted in partial fulfillment of the

requirements for the degree of

Doctor of Philosophy

University of Washington

2026

Reading Committee:

Elizabeth Nance, Chair

David A.C. Beck

Joshua Vaughan

Program Authorized to Offer Degree:

Chemistry

University of Washington

Abstract

Multi-modal Data Synthesis from Organotypic
Whole Hemisphere Brain Slice Models
to Investigate Cellular-Extracellular Interactions

Nels Wightman Schimek

Chair of the Supervisory committee:
Elizabeth Nance
Department of Chemical Engineering

The brain microenvironment is exceedingly complex and governed by interactions between and functions of cellular and extracellular components. These interactions and functions change across age, region, and under pathological conditions. Understanding how the brain microenvironment differs across these variables enables the development of therapeutics for neurological injuries and disorders. Microglia, the resident immune cells of the brain, and the extracellular matrix (ECM), a scaffold that supports tissue structure, are both implicated in disease and injury and offer therapeutics targets. While it is known that microglia and the ECM interact, the extent and mechanisms of interactions in injury and pathology is unclear, necessitating the development of tools and methods that can simultaneously detect changes of microglia and the ECM.

In this dissertation, we first develop a suite of open-source software tools that apply data science and statistical methods to data collected in the brain microenvironment. By developing these tools, we increase the complexity of the analysis that can be done on these datasets while maintaining the reproducibility of the analysis and enabling other research to build from our software. We use these tools to then demonstrate the capability of multiple particle tracking as a proxy for changes to the ECM. We show that multiple particle tracking can detect changes to

diffusion in the extracellular space (ECS) that vary with biological age and region and align with known changes to the ECM during neurodevelopment and across regions. In the same study, we demonstrate that multiple particle tracking can detect changes in an oxygen-glucose deprivation (OGD) brain slice model of hypoxic-ischemic injury and explainable machine learning can be used to determine region and treatment severity changes to nanoparticle diffusion. Next, we use confocal microscopy to investigate the heterogeneity of microglia morphologies in healthy brain tissue across six species, including human. We demonstrate that while the change in microglia morphology is conserved during neurodevelopment across species, there is regional heterogeneity based on species. We then compare microglia morphologies from white matter and gray matter regions at sexual maturity. Our results show that the differences between white and gray matter microglia in humans is distinct from the difference in rats and mice, an important translational finding. Lastly, we develop a collagen-based hydrogel mimic of brain tissue to demonstrate the feasibility of simultaneously and specially aligned multiple particle tracking and confocal microscopy of microglia. The work presented in this thesis establishes a computational framework for characterizing changes to the brain microenvironment across aging, region, and pathology at the microstructural and cellular level, and provides an experimental methodology for simultaneously investigating the interactions of microglia with the local extracellular environment in a tunable hydrogel mimic of brain tissue.

`

ACKNOWLEDGEMENTS

Thank you to my Doctoral committee for spending your time and effort giving me feedback on my work.

To my parents, Margaret and Gary, and my sister, Maren: Thank you for always inspiring me. Your support and interest in all the research I have done have helped so much over the past 6 years. Maren, your journey as a scientist has been a joy to watch, and I can't believe we both work on neonatal brain disease. Thank you to my extended family in Washington, California, Wisconsin, Minnesota, Ottowa, and Pennsylvania. I am so grateful to have such a fun, supportive, loving, huge family.

Thank you to my friends, who have supported me and spent so much time with me in person and virtually. All of your friendships have helped me maintain balance in my life that was critical for getting to the end of graduate school. A special thanks to my best friend, Adi Rao. I don't know how you still manage to put up with me, but I am grateful for it.

Thank you to my labmates past and present, in the Nance lab and in the Mourad lab. You have all made me look forward coming into the office, and my continued enthusiasm for science and research is because of the people I have gotten to work with.

Thank you to Dr. Pierre Mourad, my undergraduate mentor. Your support and passion for teaching and growing undergraduate scientists inspired me to apply to graduate school.

Thank you to Dr. David Beck. Even though I have never officially been your student, you have dedicated so much time to advancing my knowledge. The trinkets you have given me (including a literal mouse skill found on the ground) have brightened up my desk wonderfully.

Thank you to my PI and mentor Dr. Elizabeth Nance. Your guidance during the course of my graduate school education has enabled me to explore so many different aspects of science and I have grown so much as a scientist because of you.

Table of Contents

LIST OF FIGURES

LIST OF TABLES

APPENDICES

CHAPTER 1 INTRODUCTION

1.1 The Cellular and extracellular Brain Microenvironment

Brain tissue is a complex microenvironment where function is determined by interactions between cellular and extracellular components. The primary cells within the brain parenchyma are neurons and glia. Neurons are the basis of the nervous system, sending and receiving electrical signals through a complex network of connections with other neurons. Within glial cells are astrocytes, oligodendrocytes, and microglia. Astrocytes provide structural support by interacting with vasculature[1], regulating synapses[2], and maintaining the blood-brain barrier[3]. Oligodendrocytes continuously myelinate neurons[4], deliver nutrients[5], and provide axonal repair[6]. Microglia serve as the immune cell of the brain, surveying brain tissue[7] and rapidly responding to injury[8]. While the cells of brain tissue are dynamic and serve many roles, the space between cells – known as the extracellular space – is itself a dynamic microenvironment.

The extracellular space (ECS) of the brain is a critical component that affects many aspects of the brain including neurodevelopment[9], neuronal health[10,11], and transport of substances[12,13]. Within the ECS is the brain extracellular matrix (ECM), a negatively charged scaffold-like structure made of proteoglycans and glycosaminoglycans[14–18]. Specific components of the ECM have also been shown to play a crucial role in the maintenance of the homeostatic brain including memory[19] and regulation of cellular processes[9]. The structure and composition of the ECM not only differs temporally during development and aging[15], but also spatially, with known differences in structure[20] and protein expression[21] across different regions. In addition to being a complex microenvironment, both the cellular and extracellular components of brain tissue change uniquely during neurodevelopment, aging, and under pathological conditions.

1.2 Brain Microenvironment During Neurodevelopment, Aging, and Pathological Conditions

1.2.1 Neurodevelopment

During neurodevelopment, the brain tissue changes rapidly and dramatically. Microglia play a critical role in neuronal development during this time. Microglia are highly proliferative and their density rapidly increases during postnatal development[22]. Microglia transition from an ameboid morphology during early developmental stages to highly ramified morphologies[23–25]. Gene expression of microglia also changes during neurodevelopment, expressing genes related to proliferation and the cell cycle in the embryonic stage while during post-natal development expresses genes related to synaptic pruning and neurogenesis[26]. Cytokines released by microglia regulate other cells during development[27].

The ECS also shifts during neurodevelopment where ECS volume decreases[28] and the structure of the ECM increases in density and complexity[29]. Specific components of the ECM are highly involved in neurodevelopment. Proteoglycans of the ECM have been shown to regulate neuronal progenitor proliferation[30]. Laminins similarly regulate neuronal progenitor proliferation[31] as well as being a critical components of basement membranes[32]. Proteoglycans, laminins, and hyaluronic acid are involved with cell migration in developing brain[33,34]. ECM components have even been shown to induce the formation of cortical folds[35].

Changes in the expression levels of ECM components highlight the importance of the ECM during neurodevelopment. Perineuronal nets (PNNs) develop and mature during neurodevelopment[36] and the expression of PNN components is dependent on developmental stage, being higher at earlier postnatal ages[37,38]. Laminin, a glycoprotein critical to the basement membrane, has been shown to be highly expressed in the cortex of mice and humans in early

develop but not at later points in development[39]. Collagen is similarly expressed at early stages of neurodevelopment[40], with multiple isoforms contributing to processes such as neuronal outgrowth and synapse development[41,42]. Hyaluronan, a molecule that serves as the backbone of the ECM and is also involved with synapse formation[43], is also highly regulated during neurodevelopment but decreases by nearly 25% at adulthood[44]. After the brain reaches adulthood, the controlled and regulated composition of the ECM and microglia remain just as important to maintaining brain health during the aging process.

1.2.2 Aging

A significant role microglia have as the brain ages is maintenance of the myelin sheets of neurons. Microglia have been shown to regulate both demyelination and remyelination while also helping to prevent hypermyelination. Specific white-matter associated microglia have been identified during aging that clear degenerated myelin[45]. Microglia also engulf and eliminate synapses by a process called synaptic pruning[46]. Transcriptomic analysis of microglia have shown that they take on a pro-inflammatory phenotype during aging[47] leading to cytokine release, tissue remodeling, and clearing of cellular debris[48]. The changes to microglia during aging also have a direct impact on the ECM, regulating PNN formation[49] and releasing ECM-degrading enzymes[50].

Changes to the ECM during aging are caused both by the function of microglia and ECM composition dynamics. There is a reduction in chondroitin 6-sulphates, a key component of PNNs, leading to inhibition of axon growth and plasticity[51]. Hyaluronan has been shown to degrade into lower molecular weight fragments[52], which have been shown to be pro-inflammatory[53]. The degradation of hyaluronan can lead to increased solubility of another ECM component, aggrecan[52]. A reduction in the presence of collagen and laminin across different

regions also occurs during aging resulting in changes to the composition and function of basement membrane[54].Taken together, the changes to microglia and the ECM during aging reflect a progressive dysregulation of homeostasis leading altered cellular function, increased inflammation and reduced plasticity. In both neurodevelopment and aging, any pathological conditions can also result in significant changes to the brain microenvironment.

1.2.3 Pathological Conditions

As resident immune responses cells, microglia activate, recruit, and migrate to areas of pathology in a process called microgliosis, where they phagocytose cellular debris and release both pro and anti-inflammatory cytokines[55]. In response to acute injury such as ischemic stroke and traumatic brain injury, it has been shown that microglia change morphological phenotype and elevate the level of inflammatory cytokines within 3 hours[56]. Microglia then release anti-inflammatory cytokines[57,58] and growth factors[59,60] in order to preserve the damaged region. However, microglial activation in response to acute injury like stroke and traumatic brain injury results in increased matrix metalloproteinase expression and continued release of inflammatory cytokines[61,62], leading to secondary injury[63,57]. Overall, the research suggests that the response of microglia is initially protective but leads to continued inflammation in the acutely injured brain, driving chronic pathology.

Protective roles of microglia as well as dysregulation and dysfunction of microglia have been implicated in chronic brain disease and neurodegeneration. In Alzheimer's disease, microglia activation has been shown in brain tissue and specifically near plaques[64], while in Parkinsons, microglia modulate the toxic accumulation of alpha-synuclein[65], aiding in neuroprotection. However, microglial dysregulation has been shown in both conditions. In

Alzheimer's, microglia end up propagating the pathology to unaffected parts of the brain tissue[66], disrupting synapses[67], and contributing to PNN loss[67]. In Parkinsons, microglia excess secretion of pro-inflammatory cytokines appears to contribute to neurodegeneration[68,69]. While microglia respond to and phagocytose toxic buildup of alpha-synuclein[70], but may also process non-toxic alpha-synuclein, negatively impacting the microenvironment[71]. In addition to microglial changes in the presence of pathology, the ECS and ECM are also affected by pathological conditions.

The ECS and ECM are involved in a wide variety of processes, and it is unsurprising that changes to the structure and composition of the ECS and ECM have been implicated in numerous disease conditions. For example, an increase in extracellular water as well as activity of proteins associated with ECM remodeling have been connected to the pathophysiology of psychosis[72,73]. Neurodegenerative disease such as Parkinson's and Alzheimer's have shown altered parameters of diffusion in the ECS[74–78] and involvement of ECM components in pathological processes[79]. Changes to fluid flow and expression of ECM components have shown to occur in response to traumatic brain injury[80,81].

Overall, the changes in the brain microenvironment during neurodevelopment, aging, and pathology are expansive in complexity while occurring at the micro- and nanoscale. Understanding these changes across health and disease is critical for identifying biological signatures that distinguish normal development and aging from pathological states. Biophysics, the application of methods that leverage concepts from physics to study biological systems, has become a prominent framework for quantifying changes that occur within the brain microenvironment in these different settings.

1.3 Biophysics in Brain Tissue

Biophysics has been used to investigate the brain microenvironment by measuring diffusion in the brain ECS. Early studies of brain microstructure focused on relating diffusion to two key parameters of ECS microstructure: volume fraction and tortuosity. Volume fraction is defined as the total volume of the ECS divided by the total volume of the entire brain tissue[82], and experiments using real-time iontophoresis (RTI) of tetramethylammonium ions (TMA+) demonstrated that the ECS contributed to 20% of brain tissue volume[83]. Tortuosity is calculated as the ratio between diffusivity in free media compared the local ECS diffusivity[83], and measures the hindrance to diffusion caused by cellular obstruction and ECS connectivity[82]. Both parameters were demonstrated to vary during brain development[28,84]. However, a critical finding was a level of independence between the two parameters when ECS geometry changes. A study analyzing the effects on both parameters due to change in the size of the ECS through altered NaCl content showed that when the volume fraction decreased the tortuosity increase, but when volume fraction increased the tortuosity value came to a plateau[85]. Volume fraction and tortuosity were also characterized across a number of disease and injury conditions[86–89], demonstrating that diffusion in the brain ECS can be used to detect changes in brain microstructure due to pathological conditions.

The recent success in tracking the diffusion of polystyrene nanoparticles coated with polyethylene glycol (PS-PEG)[90] and single walled carbon nanotubes (SWCNTs)[91] in the brain ECS highlights the potential for nanoparticle-based probes to uncover the nanoscale structure of the ECS. Although both are nanoparticle probes, a different technique was used to track these probes. Single particle tracking (SPT) was used to track nanoparticles such as SWCNTs, while multiple particle tracking (MPT) was used to track PS-PEG coated nanoparticles. SPT and MPT are both microscopy techniques capable of measuring diffusion in living tissue. Both methods leverage

fluorescently labeled nanoparticles that are introduced into the biological system of interest. Diffusing nanoparticles are then tracked, and the mean squared displacement of a trajectory is calculated. A key difference between the two techniques is the length and number of trajectories collected for each technique. For SPT, there are a low number of trajectories collected but they can be tracked for several to tens of minutes[92] (**Figure 1.1A**). SPT methods have been used extensively to assess the organization of the brain ECS[91,93,94], detect pathological changes[95], and determine local rheological properties[91]. MPT tracks trajectories at much shorter time lengths but collects many more trajectories for a given video (**Figure 1.1B**). MPT has enabled the study of ECS structure such as the distribution of pore sizes[90] and the effect of surface coating on nanoparticle diffusion[90], changes to diffusion due to ischemic brain injury[96,97], changes to the ECM during development[29], and enzymatic degradation of the ECM[29]. In this dissertation, multiple particle tracking was used for all studies of nanoparticle diffusion.

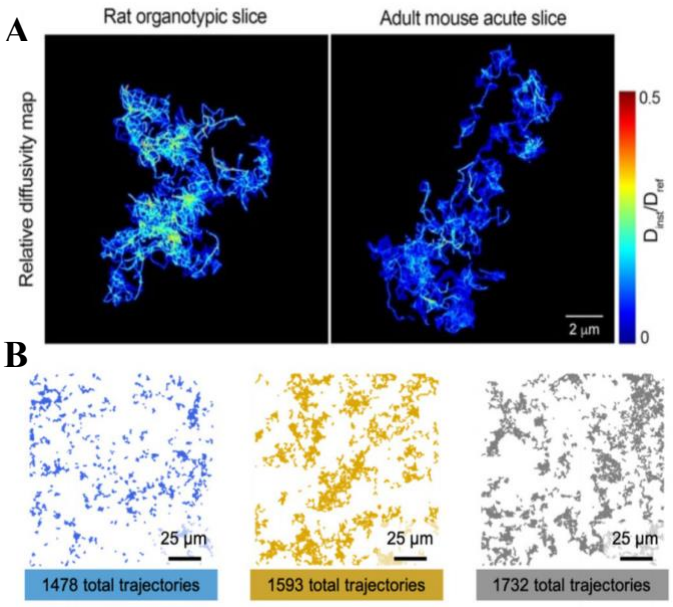

Figure 1.1 Trajectories from Single Particle Tracking and Multiple Particle Tracking experiments
A) Example of SPT trajectories tracked in rodent and mouse brain slices, taken from Paviolo et al[91]. B) Example of trajectories captured in MPT videos, taken from McKenna et al[29].

1.4 Models to Study the Brain Microenvironment

There are a wide range of models to study the brain microenvironment depending on the needed level of complexity, reproducibility, and the ability to replicate or incorporate key biological features of the brain microenvironment. In this thesis, we focus on the use of hydrogels and cultured living brain tissue slices, which are briefly introduced in 1.4.1 and 1.4.2.

1.4.1 Hydrogels

Hydrogels are biomaterials that can be engineered to have distinct properties to mimic biological environments, including brain tissue. Types of commonly used hydrogels include agarose, collagen, alginate, polyacrylamide, polyethylene glycol, hyaluronic acid, and polypeptides[98]. Hydrogels can be designed to mimic the ECM[99] and then used as a 3D cell culture[100] and are used to study interactions between cells and ECM materials through metabolic labeling[101].

Advances in biomaterials research has enabled the design of hydrogels that can be tuned to specifically mimic brain tissue. Hydrogels have been used to study neuronal cell growth[102], neurogenesis[103], and the influence of gel stiffness on cell fate[104]. They have been used to study astrocyte behavior[105] and microglia morphology, motility, and function[106]. Hydrogels can also be used as models of pathology researchers have used them to study glioblastoma[107,108] and neuroinflammation[109]. Collagen gels seeded with BV2 microglia have also been used to study the morphological and gene expression response of microglia after LPS stimulation[110]. Despite the many use cases of hydrogels, it is also critical for effective translational research to be able to directly evaluate changes in brain tissue from a living species, which retains the native composition and structure of the brain microenvironment.

1.4.2 Organotypic Whole Hemisphere Brain Slices

In the Nance lab, we have developed the organotypic whole hemisphere (OWH) brain slice model to analysis the brain microenvironment in response to development[29], disease[96,97], and treatment[111]. OWH brain slices maintain the 3D microstructure of the brain, are viable for long enough to probe temporal aspects of disease and provide access to multiple regions of the brain on a single slice, including deep brain regions[96,112,113]. Furthermore, OWH brain slices can be probed to detect changes at multiple scales of the brain tissue and using multiple modes for data collection. We can measure microrheological changes to the brain extracellular environment using MPT[29,96]. We can capture cellular changes including morphology, proliferation and density through confocal microscopy imaging and biological assays[114,115]. OWH brain slices can also be processed to capture changes to biomarkers of pathology through methods such as QT-PCR[111]. Overall, OWH brain slices present a platform that can enable the collection of multiple modalities of biological data while accurately representing the complex microenvironment of brain tissue.

1.5 Analysis of Biophysics and Microenvironmental Data

Because of the complexity of data collected studying the brain microenvironment, software and data science are critical for determining the changes in these systems. Processing videos of diffusing probes is typically done through Fiji/ImageJ, using plugins such as TrackMate. The output is processed with MatLab or Python to calculate statistical and geometric features, including measures of diffusion and features related to the shape of the trajectory. Machine learning has become a prominent tool for analyzing particle tracking data. Neural networks and decision trees have been applied to MPT data to predict aspects of the microenvironment

including gel stiffness and viscosity[116], and biological age of brain slices[29]. The most common application has been to predict diffusion modes in a sample from particle trajectories[117,118,119]. Processing of immunofluorescent microscopy images of microglia is highly varied between studies and is often not reported[120]. Similar to particle tracking, common methods include using software like Fiji/ImageJ or using Python. Features of microglia morphology that can be calculated include measures of size, geometry, and complexity[121,122]. Both supervised and unsupervised machine learning methods can be used to quantify distinct morphologies[121,123–130].

1.6 Thesis Objectives

The objectives of this dissertation are 1) develop open-source software for reproducible analysis of complex biological microenvironments such as the brain, 2) demonstrate the capability of MPT and machine learning to assess diffusion in the brain microenvironment based on age, region, and pathology, 3) assess the effects of age, region, and species on the distribution of microglia morphologies and 4) evaluate a biomaterial platform for localized collection of multiple particle tracking and microglia morphologies to investigate microglia-ECM interactions.

Chapter 2 introduces the software packages that are used and created for the analysis done in this dissertation. The chapter first contains the software used for processing multiple particle tracking videos, calculating mean squared displacement, calculating geometric features, visualizing features, and applying machine learning models to the data. The chapter then shows software package for microglia morphology analysis and spatial analysis between microglia and nanoparticle diffusion data. Lastly, the chapter summarizes the statistical methods used throughout chapters 3, 4, and 5.

Chapter 3 and 4 comprise published or soon to be submitted work related to multiple particle tracking and microglia in OWH brain slices. In chapter 3, we apply explainable machine learning to three multiple particle tracking datasets and demonstrate that between datasets there is variance across which features are driving differences in diffusion, meaning MPT can detect microenvironmental changes that are specific to the system of interest. In Chapter 4, we compare the distribution of microglia morphologies across species that span a wide range of brain complexity, including human microglia. Our work demonstrates changes in morphology that are conserved across species while revealing other changes that vary between species and should be considered for translational research.

In Chapter 5, we motivate the need for methods that will enable direct assessment of cellular-extracellular interactions, a current knowledge gap in the field. We demonstrate that the two techniques discussed in Chapter 3 and 4 – MPT and confocal imaging of microglia – can be applied simultaneously in hydrogels seeded with live cells. In chapter 6, I summarize the work and critical findings presented in this dissertation and discuss potential future steps to further our understanding of the brain microenvironment leveraging multiple particle tracking and confocal microscopy.

CHAPTER 2 SOFTWARE AND DATA SCIENCE TOOLS

The software presented in this chapter is published on GitHub with contributions from Nels Schimek, Hawley Helmbrecht, David Shackelford, Brendan Butler, Colin Landis, Assaf Golan, Ali Toghani, Manasvini Calmidi, and Mia Yamada-Heidner.

2.1 Need for Scientific Software for Analyzing Cellular-Extracellular Interaction in the Brain

Reproducible research is a cornerstone of science[131,132], and in the age of big data developing scientific software that aids in reproducibility is a critical need[133,134]. Best practices do exist, such as the FAIR principles for research software[135,136] and the 5 Rs[137]. FAIR research principles focus on software that is easy to find, retrievable, interacts well with other software, and is usable and re-usable[136]. The 5 Rs are re-runnable, repeatable, reproducible, reusable, and replicable[137]. The development of software based on these principles enables reproducibility[138] and has the ability to advance the work of other researchers. For example, publishing code on GitHub lets it reach researchers who can build off of it[139]. Code published in this way is known as Open Source Software[133]. To ensure our contribution to a healthy open source and reproducible ecosystem, all software developed for the work in this dissertation were turned into open-source software packages hosted on GitHub.

2.2 Automation of Trackmate in Python

A small software tool called pytrackmate was written to facilitate the automation of processing MPT videos. To demonstrate the feasibility of automating the ImageJ processing workflow, an

initial version of pytrackmate has been written and is hosted publicly on GitHub: https://github.com/Nance-Lab/pytrackmate/tree/main. The software runs locally or on a high-performance computing cluster and can successfully process a folder of MPT videos using settings that are defined ahead of time, stored in a json file in the same folder. When running locally the software leverages Docker[67] to ensure the compute environment will work, and when running on an HPC uses Apptainer[68] for the same purpose.

2.3 Diff_illustrator

Diff_illustrator will take in the outputted MSD CSVs from Pytrackmate, as well as the feature CSVs generated by diff_classifier, and generate plots that are commonly used in particle tracking research. Diff_illustrator primarily uses the software packages matplotlib, Seaborn, and Altair to make visualizations. MSD vs Tau plots can be made for an individual video or for an entire experimental group. Statistical feature distributions can be made for each experimental group or each video. Video level heatmaps can be made to show the spatial distribution of features and whether certain areas have more high magnitude or low magnitude features values. Plots to show the distribution of particles undergoing super-diffusive, Brownian, or sub-diffusive motion can be made by using the alpha coefficient feature for an experimental group or a single video. For each plot that can be made, the GitHub package has a Jupyter Notebook that a user can use to run a small amount of MPT data through in order to see the functions that make the visualizations.

2.4 Diff_predictor

Diff_predictor is a Python based package that uses supervised machine learning and explainable machine learning models to predict biological variables from MPT data and calculate the most

predictive features. Diff_predictor used the Scikit-Learn software package for data processing and cleaning [69], gradient boosted decision trees through XGBoost for training and predictions [70], and calculates feature importance using the SHAP software package[61]. Detailed descriptions of these methods are described in Chapter 3.

2.5 TURMorIC

To quantify cellular morphological changes in OWH slices, we assess microglia morphology using a ML based pipeline. TURMorIC was developed as a software wrapper around the pipeline to enable modular running of the pipeline, reproducible analysis pipelines, and integration with cloud computing for parameter optimization. Microglia morphology is calculated by using the Visual aided Morphology Phenotyping Image Recognition (VAMPIRE) software methodology[72] on confocal microscopy images of microglia stained with Iba1. Prior to analysis with VAMPIRE, the images are segmented using the scikit-learn software package[73]. The segmented images are divided into training and testing data with an 80:20 split, with the testing data containing at least two images from all different combinations of sex, region, and treatment condition. VAMPIRE uses principal components analysis (PCA) on 50 shape coordinates of each segmented cell to and reconstructs the shape of each cell using the eigen-shape vectors calculated by PCA. The number of eigen-vectors used is chosen such that 95% of shape variation across the assessed cells is captured. K-means clustering is then used to determine 5 representative shape modes. After using this method on the training data to determine the 5 shape modes, the shape mode of each segmented microglia in the testing images is predicted. Scikit-image is then used to capture geometric features of microglia morphology including perimeter, circularity, area coverage, and aspect ratio.

2.6 SAFFRON

SAFFRON is a small, open-source python package for spatial alignment and analysis of fluorescent imaging data. SAFFRON takes in binary masks of cells as Numpy arrays and CSVs of nanoparticle trajectory data and first uses the micron per pixel values of each to scale and align the X and Y range and values of each input. To ensure proper alignment, a visualization of the overlay of the segmented cells and the nanoparticles is saved. For each trajectory, SAFFRON calculates the distance from the centroid of the trajectory to the nearest cell boundary, as well as recording the unique label of the cell. Using the TrackID, the features from diff_classifier are concatenated to the output. Using the unique label of each cell, the output data can be linked to cell morphology data calculated from TURmorIC.

2.7 Conclusion

The software tools described in this chapter form a modular suite of tools that can be used for processing and analyzing nanoparticle diffusion data, cellular morphology data, and data sets that combine both data modalities. Starting with Pytrackmate, raw MPT videos can be processed in an automated fashion. The outputs are then passed to diff_classifier, an open-source software package previously published by the Nance lab and generates features of diffusion and geometric features of the trajectories. The output data can then be passed to diff_illustrator for initial visualizations and exploratory analysis. Diff_predictor can then be used to make predictions and determine predictive features that separate biological outcomes or variables. TURmorIC provides a modular and reproducible pipeline for applying VAMPIRE to new microglia morphology datasets. Finally, SAFFRON is able to connect multiple particle tracking and cellular morphology data by aligning simultaneously collected and spatially aligned datasets.

These tools combine to decrease time spent processing and analyzing new MPT and cellular morphology datasets while increasing the reproducibility of any analysis that is done. Publishing the tools on GitHub also enables other researchers to apply the methodologies to their own research or build upon the existing codebases.

CHAPTER 3 HIGH-FIDELITY PREDICTIONS OF DIFFUSION IN THE BRAIN MICROENVIRONMENT

This chapter is adapted from: Schimek, N., Wood, T.R., Beck, D.A.C., McKenna, M., and Nance, E. "High-fidelity predictions of diffusion in the brain microenvironment." *Biophysical Journal* (2024). DOI: 10.1016/j.bpj.2024.10.005

3.1 Introduction

The extracellular space (ECS) is a critical component of the brain that affects neurodevelopment[9], neuronal health[10,11] and transport of substances[12,13]. Within the ECS is the brain extracellular matrix (ECM), a negatively charged scaffold-like structure made of proteoglycans and glycosaminoglycans[14–18], Specific components of the ECM play a crucial role in the maintenance of brain homeostasis including memory[19] and regulation of cellular processes[9]. The structure and composition of the ECM not only differs temporally during development and aging[15], but also spatially, with known differences in structure[20] and protein expression[21] across brain regions.

Changes to the structure and composition of the ECS and ECM have been implicated in numerous disease conditions. For example, an increase in extracellular water as well as activity of proteins associated with ECM remodeling have been connected to the pathophysiology of psychosis[72,73]. Neurodegenerative diseases such as Parkinson's and Alzheimer's have shown altered parameters of diffusion in the ECS[74–76,78] and involvement of ECM components in pathological processes[79]. Changes to fluid flow and expression of ECM components have been shown to occur in response to traumatic brain injury[80,82]. Developing methods to detect changes

in the brain microstructure can therefore be critical to understanding how pathological processes alter the brain ECS and the ECM.

Early studies that measured diffusion in the brain ECS to explore brain microstructure focused on two key parameters of ECS microstructure: volume fraction and tortuosity. Volume fraction is defined as the total volume of the ECS divided by the total volume of the entire brain tissue[82]. Experiments using real-time iontophoresis of tetramethylammonium ions (TMA+) demonstrated that the ECS contributed to 20% of brain tissue volume[83]. Tortuosity is calculated as the ratio between diffusivity in free medium compared the local ECS diffusivity[83], and measures the hindrance to diffusion caused by cellular obstruction and ECS connectivity[82]. Both volume fraction and tortuosity vary during brain development[28]; however, a critical finding by Kume-Kick et al. showed that there was a level of independence between the two parameters when ECS geometry changes[85]. When the size of the ECS was altered by manipulation of NaCl content, the tortuosity increased as the volume fraction decreased, but when volume fraction increased the tortuosity value plateaued[85]. Volume fraction and tortuosity have also been characterized across a number of disease and injury conditions[86,87,89] demonstrating that diffusion in the brain ECS can be used to detect changes in brain microstructure due to pathological conditions.

Advancements in the probes used for diffusion experiments have led to deeper understanding of the brain microstructure. Analysis of fluorescent dextran molecules revealed that dead space domains in the ECS exist in greater quantities when the rat neocortex becomes ischemic, leading to greater hindrance to diffusion due to increased tortuosity[86]. In 2006, diffusion analysis of dextran molecules and quantum dots provided one of the first estimations of ECS pore sizes in living tissue, predicting the widths of pores to be between 38 and 64 nm[140]. In 2012, diffusion of

polystyrene-polyethylene glycol (PS-PEG)-coated nanoparticles revealed that 30% of pore widths in human brain tissue were greater than 110 nm with the largest having a width of 225 nm, a significant increase compared the previously reported value[90]. The 2012 study showed that the surface functionalization of the probe influenced the probe's ability to diffuse, by taking the quantum dots used in the 2006 PNAS study and refunctionalizing them with a dense layer of PEG. These 2012 findings were later independently confirmed using single-walled carbon nanotubes, where the researchers demonstrated that pore sizes in the rodent neocortex can reach a width upward of 1 μm[91,93].

The recent success in tracking the diffusion of PS-PEG-coated nanoparticles and single-walled carbon nanotubes in the brain ECS highlights the potential for nanoparticle-based probes to uncover the nanoscale structure of the ECS, even with the use of two different tracking techniques: single-particle tracking (SPT) and multiple-particle tracking (MPT). SPT and MPT are both microscopy techniques capable of measuring diffusion in living tissue. Both methods track fluorescently labeled nanoparticles that are introduced into the biological system of interest. A key difference between SPT and MPT is the length and number of trajectories collected for each technique. For SPT, there are a low number of trajectories collected but they can be tracked for several to tens of minutes[92]. SPT methods have been used extensively to assess the organization of the brain ECS[94], detect pathological changes[95], and determine local rheological properties[91]. MPT tracks trajectories at much short time lengths but collects hundreds to thousands of trajectories for a given video. MPT has enabled the study of ECS structure such as the distribution of pore sizes[90] and the effect of surface coating on nanoparticle diffusion[90], changes to diffusion due to ischemic brain injury[29,97], changes to the ECM during development[29], and enzymatic degradation of the ECM[29].

Both SPT and MPT present opportunities for the use of machine learning (ML) due to the high dimensionality of data generated. For SPT, the high dimensionality of the data is not the number of trajectories, but the length of trajectories. The long length and timescale of diffusing particles captured by SPT has led to accurate predictions of diffusion modes from interpretable models such as linear discriminant analysis, random forests, and gradient boosted decision trees[118], and most prominently by using neural networks[117]. Due to the number of nanoparticles that can be tracked during MPT experiments, ML models can be trained directly on trajectories tracked in biological environments. For example, artificial neural networks were trained on MPT and accurately predicted nanoparticle size, surface functionality, stiffness, and viscosity based on nanoparticle behavior in hydrogels and rodent ex vivo brain slices[116]. Neurodevelopmental age of rodent ex vivo brain slices was then predicted using a gradient boosted decision tree model[29] trained on trajectories from MPT videos captured in rodent ex vivo brain slices. Both studies demonstrate that ML can be used to detect changes in MPT data that relate to the microenvironment of the ECS.

Driven by these earlier studies using ML, more work is needed to ensure that additional complex biological variables can be accurately predicted using MPT data, and that further optimization of the tools and methods can glean insightful information from these robust data sets. Whereas MPT has previously been used to characterize changes in diffusion as a result of an induced disease condition[97], it is unknown whether a ML algorithm can accurately distinguish between healthy and diseased tissue states based on MPT data. In addition, aside from the diffusion coefficient, which has been shown to change because of a disease condition, it is not known whether other features of nanoparticle trajectories are different between a healthy and diseased state.

To address these questions, we develop and validate an explainable ML pipeline to predict changes to the ECS due to age differences, regional differences, and enzymatic degradation. We then use the pipeline to predict between healthy tissue and two disease states in two different regions and determine subsets of predictive features. By applying explainable ML to multiple different systems, we determine whether supervised ML models can learn unique nonlinear relationships between features for different biological states that are not identified by traditional linear statistics.

3.2 MATERIALS AND METHODS

3.2.1 Data acquisition

All data utilized in this study exist in published databases as described in the results. No animal studies were performed in this study; however, all published data collected were performed in animal studies in strict accordance with the recommendations in the Guide for the Care and Use of Laboratory Animals of the National Institutes of Health (NIH). All animals were handled according to approved institutional animal care and use committee (IACUC) protocols (no. 4383-02) of the University of Washington. The University of Washington has an approved Animal Welfare Assurance (no. A3464-01) on file with the NIH Office of Laboratory Animal Welfare (OLAW), is registered with the United States Department of Agriculture (USDA, certificate no. 91-R-0001), and is accredited by AAALAC International. OWH brain slices were prepared from male Sprague-Dawley rat pups (Charles River, Wilmington, MA) at varying ages for the age data set[29] and at postnatal day 10 (P10) for all other data sets.

After euthanasia, brains were extracted, immersed in room temperature (22°C) dissection medium, and cut into hemispheres with a razor blade. Coronal slices (300 μm thick) were

prepared from each hemisphere using a Mcllwain tissue chopper (Ted Pella, Redding, CA)[96]. Individual OWH slices were plated on 30 mm cell culture inserts (MilliporeSigma, Burlington, MA) in nontreated 6-well plates (USA Scientific, Ocala, FL) filled with 1 mL slice culture medium and incubated in sterile conditions at 37°C and 5% CO_2. For OWH slices obtained from P14, P35, and P70 pups for the age data set, MPT was preformed within 6 h (acute) after slice explantation. For OWH slices from P10 rats to assess regional differences in diffusion, slices were cultured for 4 days in vitro (DIV) before MPT. For OWH slices exposed to enzymes, slices were obtained from P35 rats and immediately after explantation were treated with either chondroitinase ABC (ChABC) for 120 min before MPT[29]. For oxygen glucose deprivation (OGD) exposure in OWH slices, OGD medium was made by adding 120 mM sodium chloride (NaCl, MilliporeSigma), 2.8 mM potassium chloride (KCl, Sigma), 1 mM calcium chloride ($CaCl_2$, MilliporeSigma), and 10 mM 4-(2-hydroxyethyl)piperazine-1-ethanesulfonic acid buffer solution (HEPES, Gibco, Waltham, MA) to deionized water, which was then titrated using 1 M hydrochloric acid (Thermo Fisher Scientific, Waltham, MA) or 1 M sodium hydroxide (Thermo Fisher Scientific) to a pH of 7.4. The medium was then bubbled with nitrogen gas (Praxair, Danbury, CT) for 10 min. OGD was performed by adding 1 mL OGD medium to OWH samples, which were then incubated at 37°C while in a nitrogen-purged Hypoxia Incubator Chamber (STEMCELL Technologies, Vancouver, British Columbia, Canada) for 0.5 or 1.5 h. At the end of OGD exposure, OGD medium was removed and slices were returned to normal slice culture medium and 5% CO_2 conditions at 37°C.

For MPT analysis for all studies, nanoparticle probes were applied topically to slices and incubated for 30 min before imaging. Nanoparticle probes were 40 nm fluorescent carboxylate (COOH)-modified PS nanoparticles (PS-COOH) (Fisher Scientific, Hampton, NH) covalently

modified with methoxy (MeO)-PEG-amine (NH_2) (5 kDa MW, Creative PEG Works, Winston-Salem, NC) by carboxyl amine reaction[141]. The MPT videos used in this study were collected through fluorescent microscopy using a CMOS camera (Hamamatsu Photonics, Hamamatsu City, Japan) mounted on a confocal microscope. Each MPT video was collected using a frame rate of 33.3 frames per second for 651 frames at 100× magnification (oil immersion, 1.45 numerical aperture, Nikon, Melville, NY).

3.2.2 Statistical analysis

To compare individual MPT features between different OGD groups, linear mixed effects models were performed using the lme4 software package in R. A model was fit for each locally averaged feature for each individual MPT trajectory to determine fixed effects of the OGD group using the healthy control (HC) condition as the reference group. Each model included random effects of both slice and MPT video to account for correlation between individual MPT trajectories taken from the same slice as well as trajectories from particles whose data were collected in the same video at the same time. When comparing across multiple groups, differences were compared using linear combinations derived from the emmeans package, and p values < 0.05 were defined as statistically significant.

3.2.3 eXtreme Gradient Boosting

XGBoost (eXtreme Gradient Boosting) is a ML software package that uses boosted decision trees for its models[142]. A boosted decision tree model is built by sequentially adding weak prediction models fit to a subset of the full data set, continuing until a specific number of weak models is reached or the loss function of the model converges. Final predictions of the model are made through a weighted average of the predictions of each of the weak learners. XGBoost was

chosen, as tree-based models, including XGBoost, have been shown to be successful at ML tasks related to particle tracking predictions both for classification accuracy, as well as interpreting which statistical features of MPT data contributed the most to predictions[29,117,118].

3.2.4 Shapley additive explanations

Shapley additive explanation (SHAP) values were calculated for each statistical feature in each of the data sets to determine the contribution of each feature to model predictions across each data set[143]. SHAP values originate from the game theory approach of Shapley values, and are calculated for each feature by averaging how much that feature contributes to each prediction instance. Calculating SHAP values for MPT data is useful as each of the 33 features used to train the model captures a unique aspect of the data. Determining which subsets of features are most important for different MPT data sets can inform which aspects of nanoparticle trajectory diffusion are being impacted by the microenvironment they experience.

3.2.5 XGBoost predictions

The XGBoost software package generated classification predictions on each of the four data sets. Data were cleaned by removing trajectories that had missing or infinite values for any of the features. To prevent overfitting, data sets were rebalanced through majority class under sampling to ensure that each class had the same number of data points. To ensure that there was no data leakage between the training and testing data, trajectories from the same local environment were binned together such that, when split for training and testing, trajectories from the same bin were only in the training set or test set, never both. Training and testing data sets were chosen by randomly assigning bins to each such that the split is 80:20. During model training, 10% of the

training data were used for internal validation, which left a total of 70% of the class balanced data set for training.

Feature data consisted of the statistical features (**Appendix A.1**) generated with *diff_classifier*, and the target variable was either age, region, or treatment type. A cross-validation hyperparameter search was used to determine the optimal hyperparameters of an XGBoost model for each of the different data sets (**Appendix A.2)**. SHAP values were used to determine the importance of each feature to the model's predictive ability. Y-scrambling, where the target variables were randomly reassigned for each feature row, was used in conjunction with XGBoost to determine the likelihood of chance predictions.

3.3 Results

3.3.1 Data collection

For this study, we developed an explainable ML pipeline capable of predicting between injury states based on nanoparticle diffusion. We used linear effects modeling to compare features of MPT data between conditions in the injury model. Before predicting between injury states, we validated the pipeline on three sets of MPT data collected from distinct biological conditions in OWH slices—nanoparticles tracked in the cortex at different brain ages, nanoparticles tracked in different brain regions at the same age, and nanoparticles tracked in the HC or in enzymatically degraded ECM conditions in the cortex. We then applied the linear mixed models and the explainable ML pipeline to MPT data from an OGD injury model in OWH slices.

Nanoparticle diffusion data were previously obtained using MPT in rat 300 μm OWH thick brain slices from three independent experiments. Although no new raw data were generated in this article, the experimental methods that produced the data sets are briefly described in the

materials and methods. In the first experiment, age-dependent diffusion data were acquired from OWH slices collected from the cortex of male pups at P14, P35, and P70 (41), defined as the age data set. In the second experiment, brain region-dependent diffusion data were acquired from OWH brain slices from P10 male pups that included the cortex, striatum, and hippocampus, defined as the region data set. The third experimental data set contains diffusion data from P35 male pup brain slices exposed to enzymatic degradation of ECM structures using ChABC and HC slices, defined as the treatment data set. The fourth experimental data were from P10 male pup slices from the striatum or cortex from HC slices, slices treated with 0.5 h OGD or 1.5 h OGD treatment. Data from OGD-treated slices were chosen due to it being a well-characterized disease state, where OGD increases cell death and cell proliferation regionally and temporally[96], reduces glutathione production[97], drives changes to the morphology of microglia[144], and increases proinflammatory and oxidative stress markers[144]. From the acquired diffusion data, we generated statistical features for each nanoparticle trajectory with the open-sourced *diff_classifier* package. A list and description of the features is provided in Appendix A.1.

3.3.3 XGBoost accurately predictions complex biological variables across multiple data sets

To establish the likelihood of correct predictions occurring by chance, XGBoost models were trained on Y-scrambled data for each data set and had accuracy scores close to that of random guessing for the age data set (**Table 3.1**), the region data set (**Table 3.2**), and the treatment data set (**Table 3.3**), Precision, recall, and F1 score metrics of the Y-scrambled models show the lack of any predictive capacity for these models. Predictions on the age data set (**Table 3.1**), and region data set (**Table 3.2**), with the normal XGBoost model are higher than predictions with the Y-scrambled XGBoost model (+0.52 and +0.56, respectively). Predictions using normal

XGBoost of the treatment data set (**Table 3.3**), were also higher by +0.19 compared with the Y-scrambled XGBoost model. A confusion matrix of a model trained on all five regions showed that trajectories from the thalamus were almost equally likely to be predicted as hippocampus as they were thalamus, which is one possible reason that interchanging hippocampus for thalamus led to similar model accuracy. The hippocampus was chosen over the thalamus for the final model because it was predicted correctly at a higher rate when a model was trained on all five regions.

Table 3.1 XGBoost metrics for each class in the age dataset, and for the overall model, reported as median and interquartile range from 50 models trained on random, down sampled subsets of data

Evaluation	**P14**	**P35**	**P70**	**Total**
Normal model				
Accuracy	0.88 ± 0.02	0.80 ± 0.03	0.90 ± 0.04	0.86 ± 0.02
Precision	0.91 ± 0.03	0.79 ± 0.03	0.89 ± 0.02	0.86 ± 0.01
Recall	0.88 ± 0.02	0.80 ± 0.03	0.90 ± 0.04	0.86 ± 0.01
F1 Score	0.89 ± 0.02	0.80 ± 0.03	0.89 ± 0.02	0.86 ± 0.02
Y-Scrambled model				
Accuracy	0.34 ± 0.02	0.34 ± 0.04	0.33 ± 0.02	0.34 ± 0.01
Precision	0.33 ± 0.02	0.34 ± 0.02	0.34 ± 0.02	0.34 ± 0.01
Recall	0.34 ± 0.02	0.34 ± 0.02	0.33 ± 0.02	0.34 ± 0.01
F1 Score	0.34 ± 0.02	0.34 ± 0.02	0.34 ± 0.02	0.34 ± 0.01

Table 3.2 XGBoost metrics for each class in the region dataset, and for the overall model, reported as median and interquartile range from 50 models trained on random, down sampled subsets of data

Evaluation	**Cortex**	**Hippocampus**	**Striatum**	**Total**
Normal model				
Accuracy	0.88 ± 0.08	0.96 ± 0.01	0.86 ± 0.02	0.90 ± 0.03
Precision	0.85 ± 0.04	0.98 ± 0.01	0.86 ± 0.04	0.90 ± 0.03
Recall	0.88 ± 0.08	0.96 ± 0.01	0.86 ± 0.02	0.90 ± 0.03
F1 Score	0.86 ± 0.06	0.97 ± 0.01	0.86 ± 0.02	0.90 ± 0.03
Y-Scrambled model				
Accuracy	0.34 ± 0.02	0.33 ± 0.02	0.33 ± 0.02	0.34 ± 0.01
Precision	0.33 ± 0.02	0.34 ± 0.02	0.33 ± 0.02	0.34 ± 0.01
Recall	0.33 ± 0.02	0.34 ± 0.02	0.34 ± 0.02	0.34 ± 0.01
F1 Score	0.34 ± 0.02	0.33 ± 0.02	0.34 ± 0.02	0.34 ± 0.01

Table 3.3 XGBoost metrics for each class in the treatment dataset, and for the overall model, reported as median and interquartile range from 50 models trained on random, down sampled subsets of data

Evaluation	ChABC Treated	Non-Treated	Total
Normal Model			
Accuracy	0.66 ± 0.02	0.72 ± 0.03	0.69 ± 0.02
Precision	0.70 ± 0.03	0.68 ± 0.02	0.69 ± 0.02
Recall	0.67 ± 0.02	0.72 ± 0.03	0.69 ± 0.02
F1 Score	0.69 ± 0.02	0.70 ± 0.02	0.69 ± 0.02
Y-scrambled Model			
Accuracy	0.48 ± 0.01	0.52 ± 0.03	0.50 ± 0.01
Precision	0.50 ± 0.01	0.50 ± 0.01	0.50 ± 0.01
Recall	0.48 ± 0.01	0.52 ± 0.03	0.50 ± 0.01
F1 Score	0.49 ± 0.01	0.51 ± 0.02	0.50 ± 0.01

3.3.4 SHAP Shows Mean Diffusion as Most Important Feature

A significant benefit of using a boosted decision tree model on MPT data is that, in addition to seeing whether a model can predict complex biological variables, feature importance methods can be used to determine which features were used to generate predictions and learn patterns in the data. By finding the most important features in an MPT data set, it is possible to gain insight into how the trajectories differ between independent classes. We can begin to understand the biological and chemical differences that led to the model being able to generate predictions much higher than random guessing.

SHAP feature importance from an XGBoost model trained on the age data set showed that the mean diffusion coefficient at 0.33 s (mean Deff1) was the most important feature, with a magnitude of 2.4 (**Figure 3.1A**). That magnitude was more than double that of the second most important feature, the mean fitted anomalous diffusion coefficient (mean D_fit), which had a magnitude of 1.1. Four other features had a magnitude above 0.5: mean boundedness, mean trappedness, mean straightness, and mean fractal_dim. The top 12 features were all locally average mean features, demonstrating the value that local averaging of the trajectory data adds to

predictive capacity. These magnitude values were all much higher than the SHAP values determined for the Y-scrambled XGBoost model (**Figure 3.1B**). In the Y-scrambled model the top feature, kurtosis, had a magnitude of 0.086, only greater than the 15th ranked feature by 0.026. The low-magnitude SHAP values and similarity in magnitude across the top 15 features indicates that the high magnitudes found in the normal XGBoost model are representative of key components of the data that differentiate trajectories from different age groups.

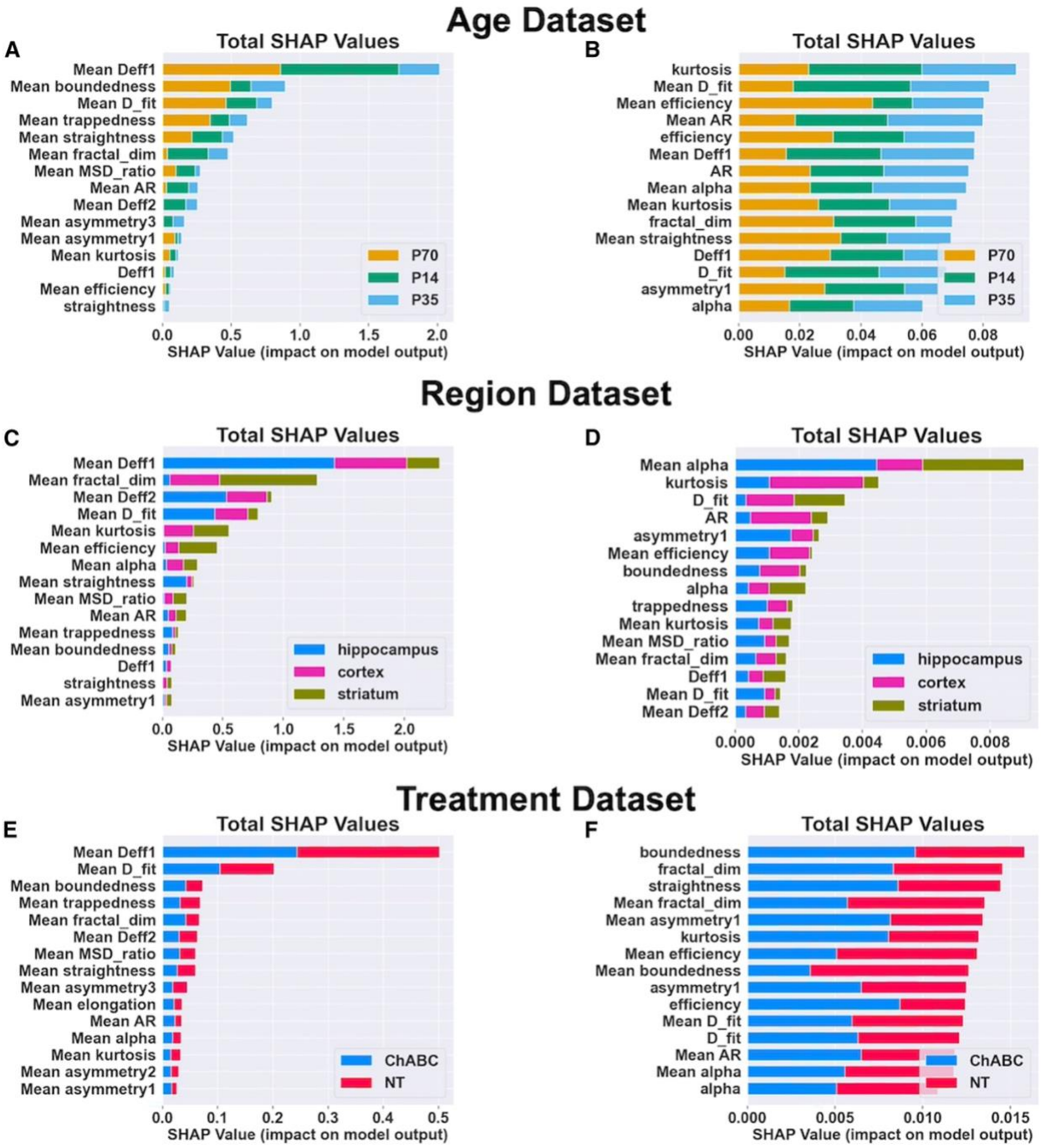

Figure 3.1 SHAP values of normal and Y-scrambled models for each data set.

(A) Ranked SHAP features for XGBoost model trained on age data set with all features. **(B)** Ranked SHAP features for XGBoost model trained on Y-scrambled age data set with all features. **(C)** Ranked SHAP features for XGBoost model trained on region data set with all features**. (D)** Ranked SHAP features for XGBoost model trained on Y-scrambled region data set with all features. **(E)** Ranked SHAP features for XGBoost model trained on enzyme-treated data

set with all features. **(F)** Ranked SHAP features for XGBoost model trained on Y-scrambled enzyme-treated data set with all features.

Similar to the results from the age data set, the top feature for the region data set was mean Deff1with a magnitude of 2.3 (**Figure 3.1C**). Mean fractal_dim was the only other feature above 1.0 with a magnitude of 1.3 and mean Deff2 (mean diffusion coefficient at 3.3 s), mean D_fit, and mean kurtosis were all above 0.5, indicating the key features driving differentiation between trajectory motion in the different regions. SHAP values of an XGBoost model trained on Y-scrambled data showed features with magnitudes all below 0.04 (**Figure 3.1D**), demonstrating the lack of predictive power from the Y-scrambled features.

SHAP feature importance for an XGBoost model trained on the treatment data showed much lower magnitudes compared with the age and region data sets (**Figure 3.1E**), which was unsurprising due to the comparatively lower prediction accuracies on the treatment data set. Mean Deff1 was again the top feature but had a magnitude of only 0.55. Mean D_fit, with a magnitude of 0.12, was the only other feature with a magnitude above 0.1. SHAP values from an XGBoost model trained on Y-scrambled data from the treatment data set all fell below 0.015 (**Figure 3.1F**), again showing no predictive power from the Y-scrambled data. The low magnitudes of the SHAP values from the normal XGBoost model on the treatment data set indicate that mean Deff1 was the only feature the model could consistently use to differentiate between trajectories from the two classes. Despite the low magnitude, the even lower SHAP values of the Y-scrambled model indicate there are true differences in the diffusion coefficients of trajectories from HC and ChABC-treated slices that can be identified by the XGBoost model.

3.3.5 SHAP Captures Statistically Significant Features Across Age

To validate that the most important features determine by SHAP were indicative of regional and neurodevelopmental differences, a linear mixed effects model was used to determine whether features differed between age groups and brain regions when accounting for potential random effects due to slice variability. Three of the top 6 most important features—mean Deff1, mean straightness, and mean D_fit—followed the same trend, where the mean value of the feature was highest in the P14 group and decreased in each of the P35 and P70 groups (**Figure 3.2A-C**), with each age group being statistically significant from each other for each feature. For mean Deff1, the mean value was 22.84 for P14 (95% confidence interval of [19.94, 25.74]), which decreased to 7.56 ([4.66, 10.45], $p < 0.001$) for P35 and was lowest for P70 at 2.20 ([−0.733, 5.12], $p < 0.001$ compared with P14 and $p < 0.05$ compared with P35) (**Figure 3.2A**). The mean value at P14 for mean straightness was 0.34 ([0.317, 0.364]), 0.217 ([0194, 0.241], $p < 0.001$ compared with P14) at P35, and 0.146 ([0.122, 0.170], $p < 0.001$ compared with both P14 and P35) at P70 (**Figure 3.2B**). Mean D_fit had a mean value of 29.52 ([26.24, 32.8]) at P14, which decreased to 17.19 ([13.93, 20.5], $p < 0.01$ compared with P14) at P35 and 6.48 ([3.15, 9.8], $p < 0.001$ compared with both P14 and P35) at P70 (**Figure 3.2C**). Mean trappedness and mean boundedness followed similar trends where there P14 and P35 did not differ significantly, while P70 was lower compared with both other ages (**Figure 3.2D, Figure 3.2E**). For mean trappedness, the mean values for P14 and P35 were both −0.194 ([−0.193, −0.195]) while the mean value for P70 was −0.204 ([−0.203, −0.205], $p < 0.001$ compared with both P14 and P35). For P14 and P35, the mean values of mean boundedness were 0.110 ([0.107, 0.114]) and 0.109 ([0.106, 0.133]), respectively, decreasing to 0.0758 ([0.072, 0.080], $p < 0.001$ compared with both P14 and P35) for the P70 group. Mean fractal_dim was lowest in the P14 group with a value of 1.53 ([1.48, 1.59]) and was significantly different compared with both P35 at 1.75

([1.70, 1.81], $p < 0.001$) and P70 and 1.81 ([1.75, 1.87], $p < 0.001$) (**Figure 3.2F**). Mean fractal dimension was not significantly different between the P35 and P70 groups.

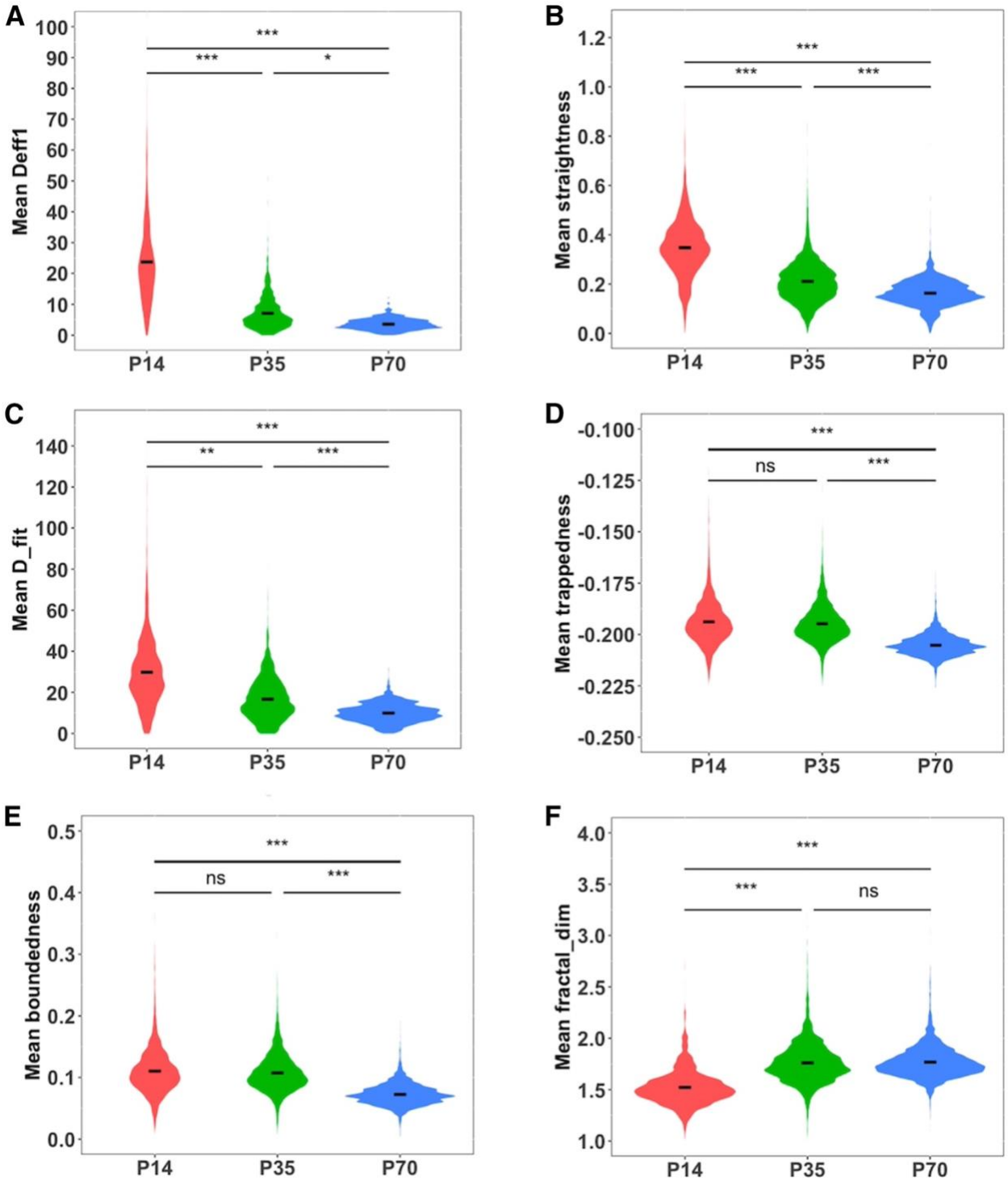

Figure 3.2 Distributions of statistically significant features for age data set when accounting for fixed effects.

(A) Violin plots showing the distributions of the mean Deff1 feature for each age. **(B)** Violin plots showing the distribution of the mean straightness feature for each age. **(C)** Violin plots showing the distributions of the mean Deff1 feature for each age. **(D)** Violin plots showing the

distribution of the mean straightness feature for each age. **(E)** Violin plots showing the distributions of the mean Deff1 feature for each age. **(F)** Violin plots showing the distribution of the mean straightness feature for each age. Statistical significance is indicated by $^{*}p < 0.05$, $^{**}p < 0.01$, $^{***}p < 0.001$.

The most important SHAP features for the region data set also captured regional differences that were found to be statistically significant. Mean Deff1, mean D_fit, and mean efficiency showed similar trends where all regions where comparisons between all regions showed statistically significant differences with data the value from the hippocampus being the highest across each feature. Mean Deff1 was lowest in the striatum with a mean value of 0.66 ([0.34, 0.97], $p < 0.001$), slightly higher in the cortex at 0.81 ([0.49, 0.1.12], $p < 0.001$), and had a value of 11.55 ([11.23, 11.87], $p < 0.001$) in the hippocampus (**Figure 3.3A).**The mean value of mean D_fit was lowest in the cortex at 1.69 ([−0.322, 3.7], $p < 0.001$), increased in the striatum at 2.49 ([0.49, 4.5], $p < 0.001$) and was 16.44 ([14.43, 18.40], $p < 0.001$) in the hippocampus (**Figure 3.3B**). Mean efficiency was lowest in the striatum at 0.26 ([0.14, 0.39, $p < 0.001$]), with a value of 0.44 ([0.31, 0.56], $p < 0.001$) in the cortex and 1.02 ([0.89, 1.14], $p < 0.001$) in the hippocampus (**Figure 3.3C**). Mean values for mean kurtosis and mean fractal_dim differed across each region with each feature following similar trends. Mean kurtosis was lowest in the hippocampus at 3.32 ([2.22, 4.42], $p < 0.001$), increased to 4.10 ([3.00, 5.20], $p < 0.001$) in the cortex, and was highest in the striatum at 4.55 ([3.45, 0.32], $p < 0.001$) (**Figure 3.3D**). Similarly, mean fractal_dim had a value of 1.80 ([1.36, 2.25], $p < 0.001$) in the hippocampus, 2.18 ([1.74, 2.63], $p < 0.001$) in the cortex, and was 2.31 ([1.87, 2.76], $p < 0.001$) in the striatum (**Figure 3.3E**). Mean Deff2 was found to be not significant between the cortex and striatum with mean values of 0.141 (−0.03, 0.31) and 0.143 ([−0.03, 0.32]), respectively, while the value of mean

Deff2 hippocampus was significantly different compared with both cortex and striatum at 1.098 ([0.92, 1.27], $p < 0.001$) (**Figure 3.3F**).

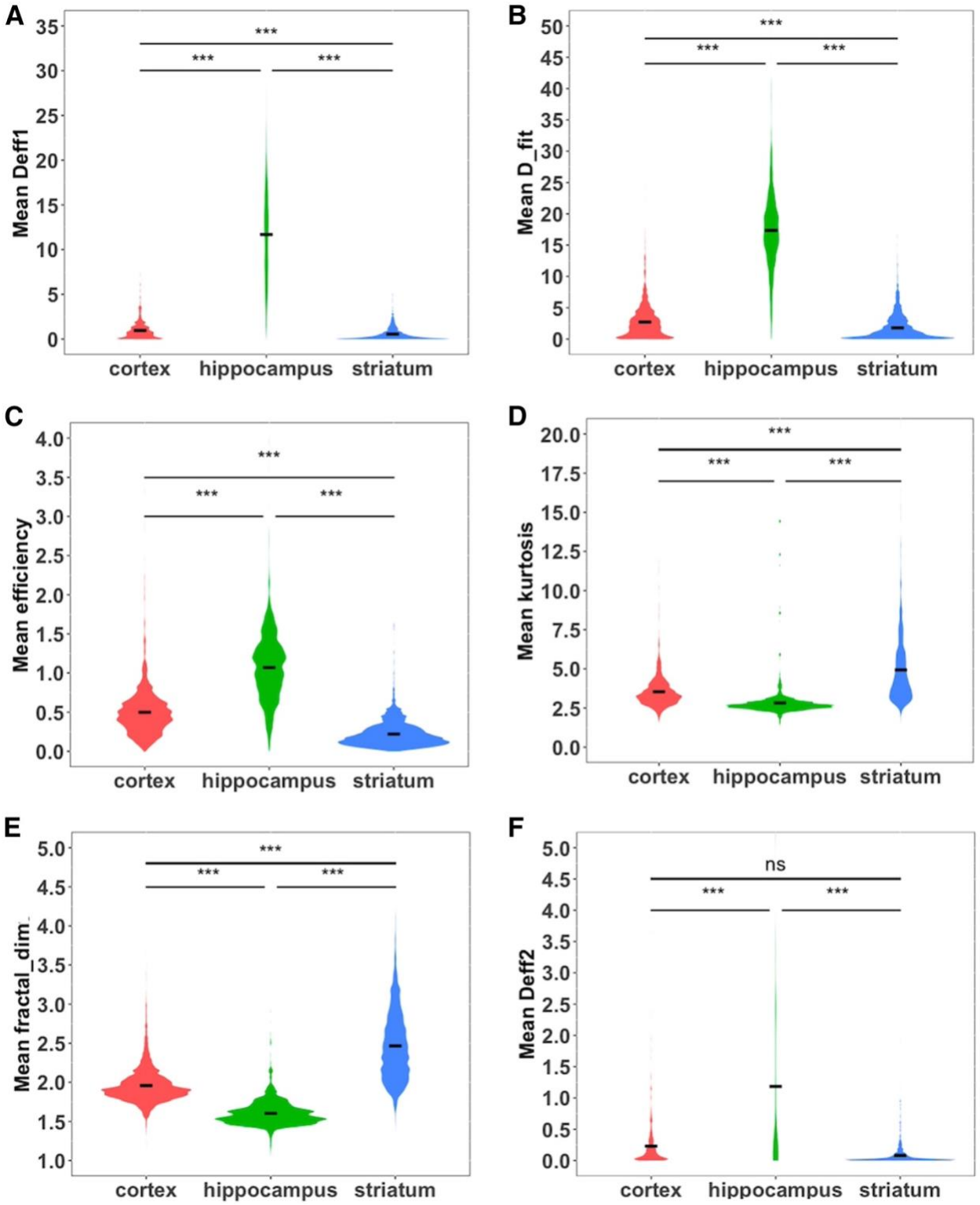

Figure 3.3 Distributions of statistically significant features for region data set when accounting for fixed effects.

(A) Violin plots showing the distributions of the mean Deff1 feature for each region. **(B)** Violin plots showing the distribution of the mean D_fit feature for each region. **(C)** Violin plots showing the distributions of the mean efficiency feature for each region. **(D)** Violin plots showing the distribution of the mean kurtosis feature for each region. **(E)** Violin plots showing the distributions of the mean fractal_dim feature for each region. **(F)** Violin plots showing the distribution of the mean Deff2 feature for each region. Statistical significance is indicated by $^{*}p < 0.05$, $^{**}p < 0.01$, $^{***}p < 0.001$.

3.3.6 Distribution of Geometric Features Shows Differences Between Healthy and Disease Conditions

To decrease model complexity and increase interpretability, we used a decreased number of features published in previous literature (43). The features fall under three primary categories: those related to the MSD data (Deff1 and mean Deff1, MSD_ratio mean MSD_ratio, alpha and mean alpha, trappedness and mean trappedness), those related to the radius of gyration tensor (kurtosis and mean kurtosis, asymemetry1, and mean asymmetry1), and those related to the steps in a trajectory (fractal_dim and mean fractal_dim, straightness and mean straightness, efficiency and mean efficiency). To determine any effects due to brain slice variability and trajectory length, we used a linear mixed effects model and assessed whether the mean of each locally averaged feature was significantly different between the HC data and each treatment condition while accounting for slice effects and trajectory length effects. Correlation plots between each feature and trajectory length are shown in **Appendix A.2**, where there was not a common directionality of effect of the trajectory length on individual features. For the cortex data, mean MSD_ratio feature was significant for the 0.5 and 1.5 h OGD conditions when accounting for slice effects, while mean fractal_dim was significant for the 0.5 h OGD condition. The mean of the mean MSD_ratio feature was 0.88 for the HC, which decreased to 0.60 (95% confidence interval of [0.528, 0.672], $p = 0.037$) in the 0.5 h OGD condition and to 0.633 ([0.561, 0.706], $p = 0.037$) in the 1.5 h OGD condition (**Figure 3.4A**). The mean of the mean fractal_dim

feature was 1.98 in the HC condition, decreasing to 1.74 (95% confidence interval of [1.63, 1.82], $p = 0.041$) in the 0.5 h OGD condition and to 1.76 ([1.66, 1.84], $p = 0.051$) in the 1.5 h OGD condition (**Figure 3.4B**)

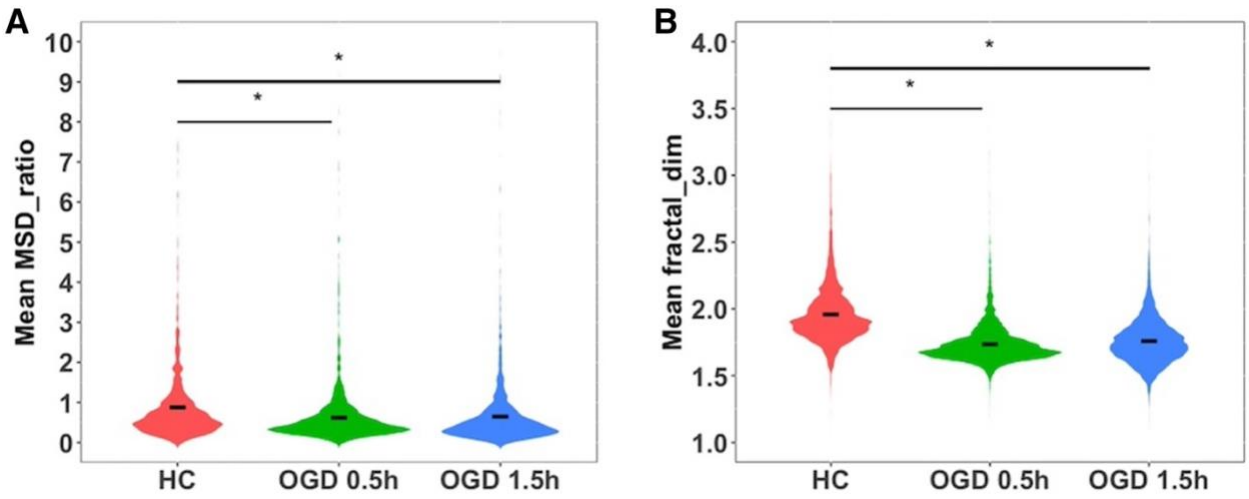

Figure 3.4 Distributions of statistically significant features from cortex when accounting for fixed effects.

(A) Violin plots showing the distributions of the mean MSD_ratio feature for HC, OGD 0.5 h, and OGD 1.5 h conditions in the cortex. **(B)** Violin plots showing the distribution of the mean fractal_dim feature for HC, OGD 0.5 h, and OGD 1.5 h conditions in the cortex. Statistical significance compared with HC ($^{*}p < 0.05$).

For the striatum data, mean straightness and mean efficiency were statistically significant for both treatment groups, while mean fractal_dim and mean alpha were only significant for the 1.5 h OGD treatment condition. The mean of the mean alpha feature was 0.76 for the HC, increasing to 0.9 (95% confidence interval of [0.863, 0.937], $p = 0.055$) in the 0.5 h OGD condition and to 0.94 ([0.889, 0.963], $p = 0.036$) in the 1.5 h OGD condition (**Figure 3.5A**). Mean straightness had a mean of 0.09 in the HC, which increased to 0.19 ([0.164, 0.208], $p = 0.021$) in the 0.5 h OGD condition and was 0.21 ([0.184, 0.229], $p = 0.011$) in the 1.5 h OGD condition (**Figure 3.5B**). The mean of the mean efficiency feature was 0.22 in the HC, 0.78

([0.661, 0.877], $p = 0.012$) in the 0.5 h OGD condition, and 0.89 ([0.743, 0.959], $p = 0.008$) in the 1.5 h OGD condition (**Figure 3.5C**). For mean fractal_dim the mean was 2.46 in the HC, which decreased to 1.78 ([1.61, 2.02], $p = 0.058$) in the 0.5 h OGD condition and further to 1.71 ([1.57, 1.98], $p = 0.046$) in the 1.5 h OGD condition (**Figure 3.5D**).

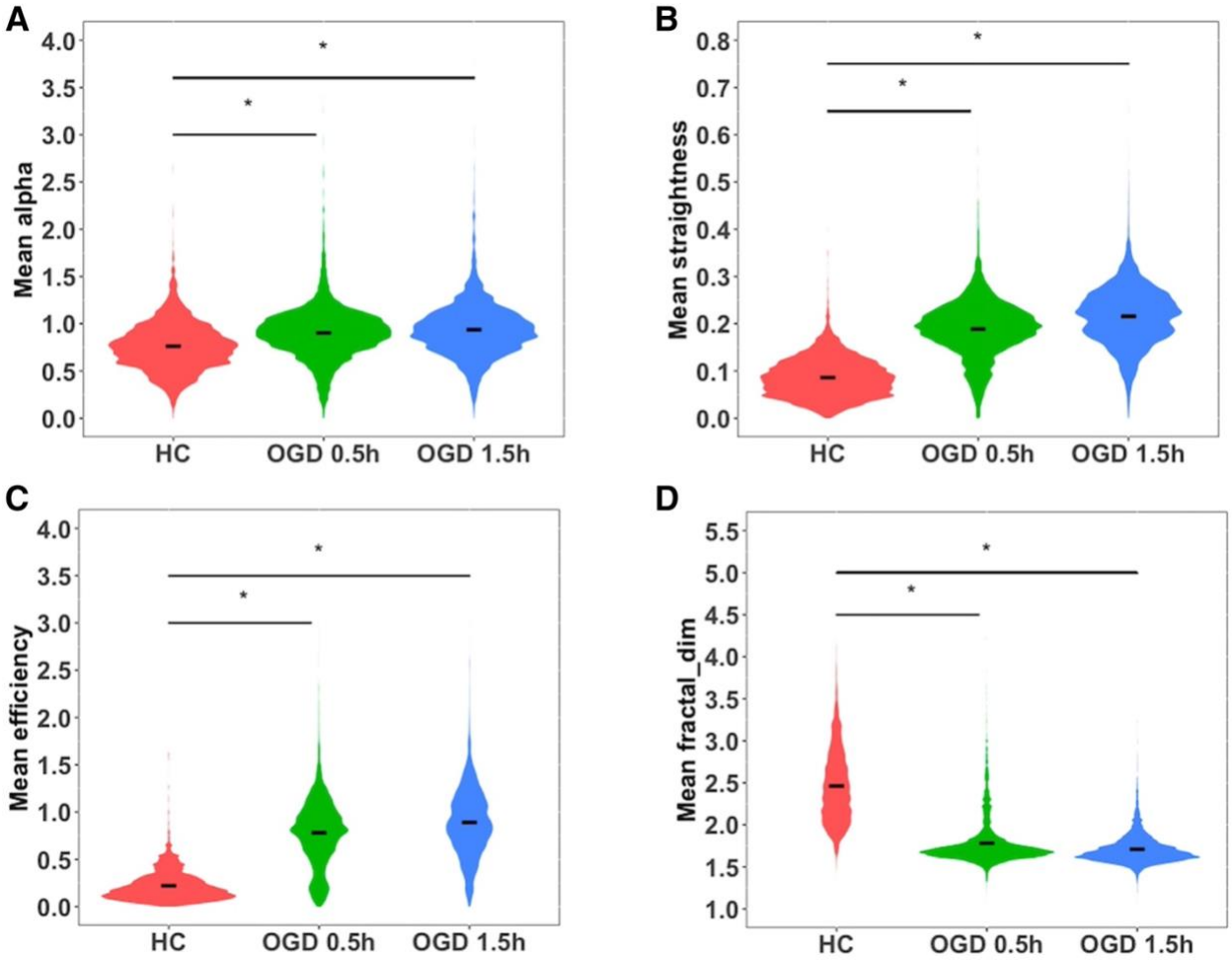

Figure 3.5 Distributions of statistically significant features from striatum when accounting for fixed effects.

(A) Violin plots showing the distributions of the mean alpha feature for HC, OGD 0.5 h, and OGD 1.5 h conditions in the striatum. **(B)** Violin plots showing the distribution of the mean straightness feature for HC, OGD 0.5 h, and OGD 1.5 h conditions in the striatum. **(C)** Violin plots showing the distributions of the mean efficiency feature for HC, OGD 0.5 h, and OGD 1.5 h conditions in the striatum. **(D)** Violin plots showing the distributions of the mean fractal_dim feature for HC, OGD 0.5 h, and OGD 1.5 h conditions. Statistical significance compared with HC ($^*p < 0.05$).

3.3.7 XGBoost and SHAP predict healthy and OGD-treated data and determine key features

To ensure that slice effects of non-statistically significant features did not impact the XGBoost model predictions, all trajectories from one slice for each condition were held out as the test set during model training and the remaining data were used for training. Model accuracy was then calculated based on predictions on the held-out data. Fifty models were trained for each region, with the mean accuracy on the cortex data being 58.70 ± 0.06% and the mean accuracy on the striatum data being 66.46 ± 0.05%. By training an XGBoost model on the MPT data and using SHAP values to determine feature importance, we aimed to determine whether the model could accurately distinguish between nanoparticles diffusing in disease compared with healthy conditions and find features that could be further investigated to understand changes to the ECM with disease onset.

XGBoost models were able to accurately classify trajectories from healthy brain slices in both the cortex (**Figure 3.6A**) and striatum (**Figure 3.6C**), rarely predicting trajectories from healthy slices as from an injured slice. While the accuracy of the XGBoost models did decrease when making predictions on the two injury conditions in both the cortex and striatum, the predictive accuracy for each class was still well above random guessing. In addition, the mistakes were primarily the model predicting one injury condition as the other injury condition, rather than incorrectly classifying a trajectory from an injury condition as one from a healthy condition. These results demonstrate that an XGBoost model can accurately determine the trends on the data that differentiate trajectories moving in healthy brain slices compared with ones treated with OGD and can detect enough differences between the two OGD conditions to predict at an accuracy above random guessing.

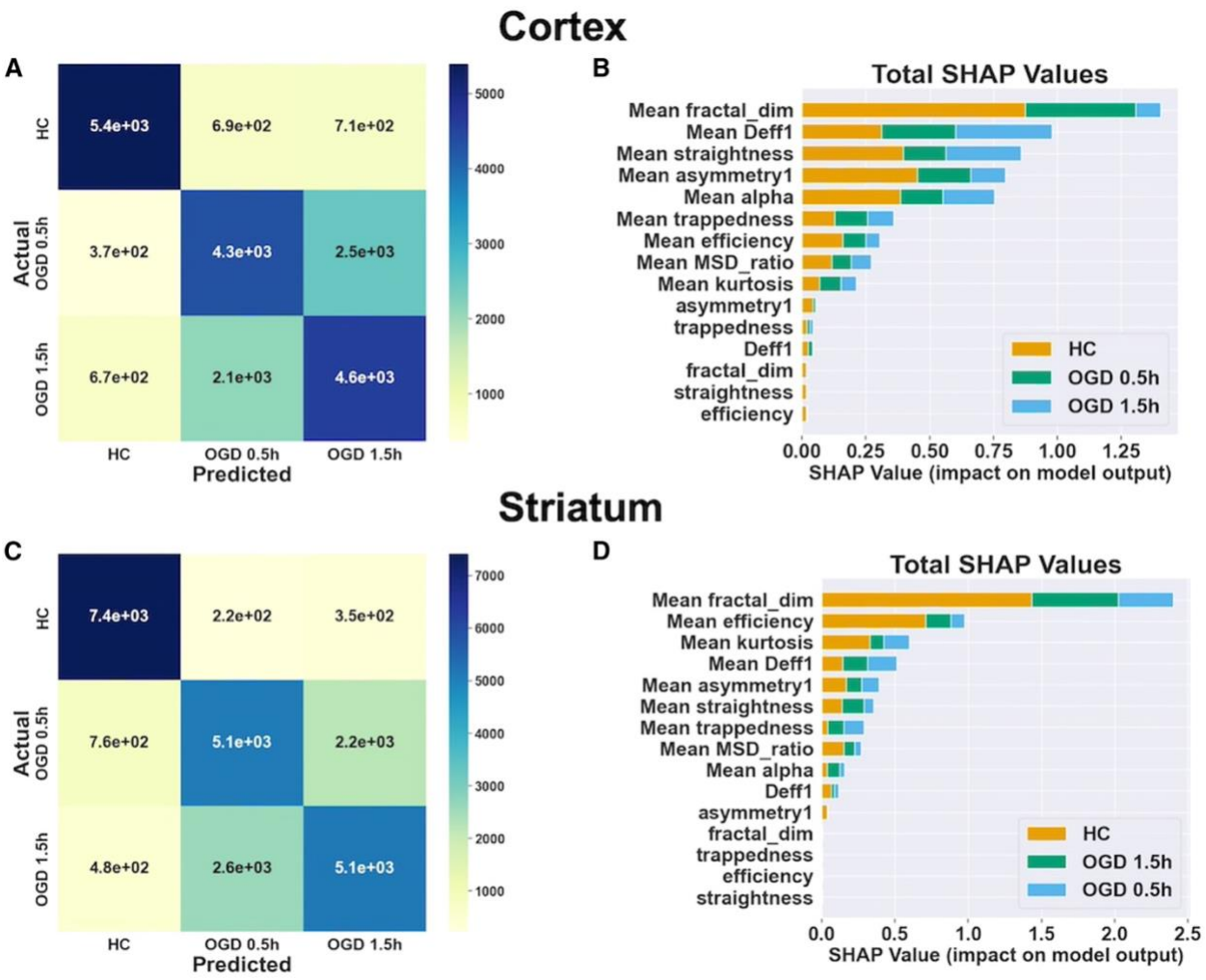

Figure 3.6 Confusion matrices and feature importance values for disease progression predictions

(A) XGBoost predictions of 0.5 h OGD, 1.5 h OGD, and nontreated brain slices in the cortex. (B) SHAP feature importance values of 0.5 h OGD, 1.5 h OGD, and nontreated brain slices in the cortex. (C) XGBoost predictions of 0.5 h OGD, 1.5 h OGD, and nontreated brain slices in the cortex. (D) SHAP feature importance values for 0.5 h OGD, 1.5 h OGD, and nontreated brain slices in the cortex.

Calculating SHAP values for each feature reveals regional differences in what features most contribute to an XGBoost model's predictions. For the striatum data, the total magnitude of the mean fractal dimension is more than three times greater than the second most important feature (**Figure 3.6D).** While mean fractal dimension was also the top feature for the cortex data set

(**Figure 3.6B**), the magnitudes of the top 5 features were much closer compared with the striatum data. These results indicate that changes to the brain microenvironment as a result of OGD treatment are regionally dependent, supporting prior biological characterization of regional diffusion data (39).

3.3.8 SHAP analysis demonstrates region- and treatment-condition-specific changes to diffusion

By further analyzing the top features as determined by SHAP for each condition from each region, it is possible to gain increased insight into how diffusion changes in each unique microenvironment. This approach enables a deeper understanding of how the magnitude of each feature helps distinguish healthy data from OGD-treated data, and differences between each OGD condition.

For the cortex data, a high mean fractal dimension value, high value of mean asymmetry, and high value of mean alpha, were key features used to distinguish between healthy and either of the OGD classes (**Figure 3.7A-C**). Mean straightness appeared to specifically be useful in differentiating between HC (**Figure 3.7A**) and 1.5 h OGD (**Figure 3.7C**) treatment data. Low values of mean straightness were highly important for HC (**Figure 3.7A**) and high values for 1.5 h treatment (**Figure 3.7C**), but it does not appear as a top 5 feature for 0.5 h OGD treatment (**Figure 3.7B).** Mean Deff1 was the most important feature for the 1.5 h OGD treatment condition, second most important for 0.5 h OGD treatment condition, and also appeared in the top 5 for the HC. Medium to high values of mean Deff1 were indicative of both the 0.5 and 1.5 h OGD treatment conditions (**Figure 3.7B, Figure 3.7C**), which could help explain why the model struggled to differentiate between the two conditions, while low values of mean Deff1 (**Figure 3.7A**) were associated with the HC condition.

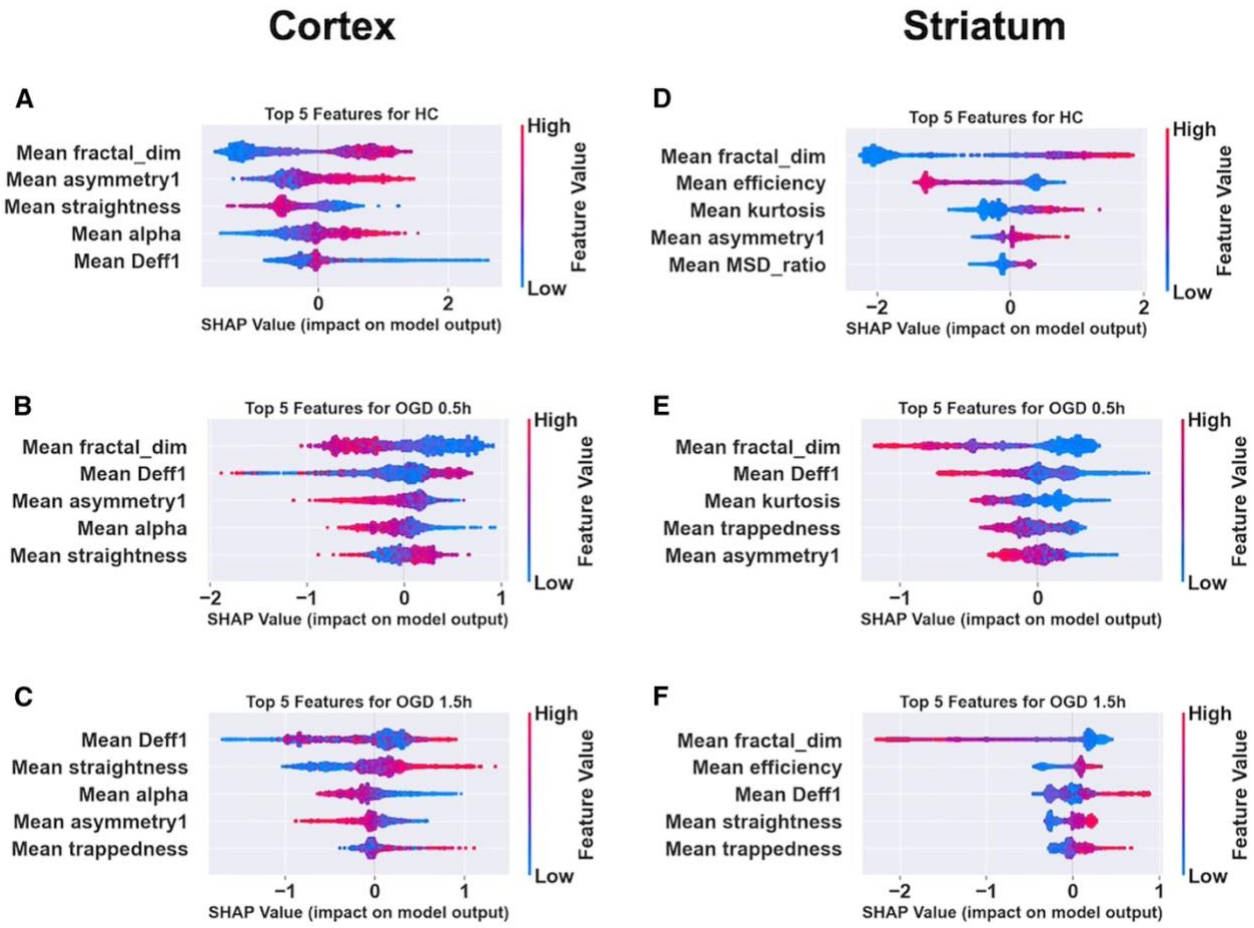

Figure 3.7 SHAP analysis of XGBoost models for each data set shows that mode of injury can be differentiated by unique subsets of trajectory features.

Top 5 features determined by SHAP for the cortex for **(A)** HC, **(B)** 0.5 h OGD treatment, and **(C)** 1.5 h OGD treatment. **(D)** Top 5 features determined in the striatum by SHAP for **(D)** HC, **(E)** 0.5 h OGD treatment, and **(F)** 1.5 h OGD treatment.

For the striatum data, a high value of mean fractal_dim was also associated with HC compared with low values associated with both OGD conditions (**Figure 3.7D-F**), with mean kurtosis having the same trend. Mean asymmetry1 appeared to help distinguish specifically between HC (**Figure 3.7D**) and 0.5 h OGD (**Figure 3.7E**), where high values were associated with HC and low values associated with 0.5 h OGD data. To further distinguish between HC and 1.5 h OGD data, the model found the mean efficiency to be important, with low values

associated with HC (**Figure 3.7D**) and average to high values being associated with 1.5 h OGD (**Figure 3.7F**). Mean Deff1 and mean trappedness were in the top 5 features for both OGD conditions (**Figure 3.7E, Figure 3.7F**) but not the HC, indicating that these features may indicate an exposure time difference in the response to OGD treatment.

Notably, feature distributions of the top predictors in the SHAP plots show that many predictors have nonlinear relationship with the outcome being predicted (**Figure 3.7**). For example, when predicting HC in the cortex, SHAP values for mean Deff1 are near zero when mean Deff1 is high, but non-zero (both negative and positive) SHAP values are seen when mean Deff1 is low. This is one example of how SHAP analyses allow for better visualization of complex nonlinear relationships that exist between the predictors and the outcome variables.

Overall, these results align with the distributions of the features used (**Figure 3.4 and Figure 3.5**), highlighting that the XGBoost model is correctly detecting the trends that exist within the data. While this is unsurprising, it is important to confirm that the XGBoost model is picking up on trends in the data known to be present. More importantly, these results demonstrate that SHAP values can be used to go further than the trends shown by the feature distributions and find subsets of statistical features of diffusion, which may be indicative of different responses in brain tissue due to increased OGD exposure time, or due to how different regions respond to OGD. While the results do not directly reveal how the tissue has changed due to OGD treatment, these results highlight aspects of diffusion that could be probed with future experiments.

3.4 DISCUSSION

Determining changes to the brain microenvironment in models of disease or injury is critical for the characterization of ECS pathology. While diffusion has been shown to change due to

injury[74,86,87], studies have focused on bulk changes to diffusion and changes to pore size[96,144]. To increase the depth at which changes to diffusion can be analyzed in injury states, we aimed to build a ML pipeline to predict between heathy and injury states and to investigate region and exposure time-specific changes to statistical features of diffusion. To ensure the validity of ML predictions, we first used a pipeline to make predictions under three conditions: biological age, brain region, and enzymatic degradation of ECM components. Because injury across groups is typically measured with traditional statistical approaches, we used linear effects models to compare MPT features across OGD conditions. This approach additionally presents a novel and robust approach to control for correlation between related MPT trajectories when analyzing MPT data. We then show that the ML pipeline predicts between healthy and OGD conditions with good accuracy and helps identify nonlinear relationships and predictors that traditional linear statistics cannot.

The consistency of the ML pipeline described in this paper across multiple data sets demonstrates the feasibility of applying a ML approach to MPT studies for pattern identification in the data that may be informative of biological underpinnings. The application of the Y-scrambling method shows that the technique can properly ensure that the accuracy of the supervised learning models is indeed caused by the model uncovering patterns in the data. The random-guess accuracy and low SHAP values of the XGBoost model trained on Y-scrambled age data further indicate that there are clear differences in diffusion between the P14, P35, and P70 microenvironments that the model can detect. Studies looking at changes in diffusion during the neurodevelopmental process in rats has shown that the ECS volume fraction decreases with age (26). In this study, a large decrease in volume fraction between postnatal days 10 and 21 was observed, but not between P21 and adults aged 90–120 days. Since some of the most important

features for the age data set are mean boundedness, mean trappedness, and mean straightness, which relate to the confinement of the nanoparticle trajectory, the model may be picking up changes in nanoparticle diffusion related to in ECS volume fraction between P14, which would have a relatively large volume fraction, and P70, which would have a smaller volume fraction.

Regional volume in the OWH slices used in these studies and more limited data sampling may also be a contributing factor to distinguishing between different brain regions. In this study, 10 videos were recorded and quantified from both the striatum and cortex, but only 6 were collected from each of the hippocampus, basal ganglia, and thalamus. As a result, highlighted by the output of the Y-scrambled model, the data collected from those three regions may have provided enough of a difference in feature values for a model to separate one of the classes from the striatum and cortex, but not enough to differentiate between the three regions that had lower data sampling. Future experimental work could increase video collection in the regions that contain the least number of particles tracked for a more even sample size across brain regions, or account for subregions within the specified brain regions.

That each age or region class had a unique subset of important features determined by SHAP demonstrates that applying explainable ML techniques to SHAP values can elucidate structural information, as it aligned with established knowledge of perineuronal net (PNN) development during aging[145]. These results confirm that this method detects known differences in ECM structure. Key important features other than those related to diffusion are also likely to pick up differences in the ECM other than PNNs. McKenna et al. suggested that the variance of composition of ECM proteins across development[146] could play a role in changing ECM viscosity and obstruction of nanoparticle motion. In addition to effecting features relating to diffusion, these changes could also impact important geometric features relating to nanoparticle

travel distance and motion within a confined space[118]. Regional differences in diffusion align with results from MRI data in rodents, where diffusivity is different across brain regions in rats[147] and mice[148]. Analysis of MRI data from cortex and striatum in adolescent rats showed differences in four measure of diffusivity—T2, mean, axial, and radial—as well as differences in volume and myelination[147]. In addition, studies have shown regional differences in microglia populations[149] and brain capillary density[150]. Altogether, these differences would alter the space and local structure of the microenvironment through which nanoparticles diffuse for each region, which could cause differences in geometric features that relate to the space taken up by the trajectory, such as mean fractal dimension and mean kurtosis[156].

For the enzyme treatment data set, each enzyme may have different mechanisms of action but degrade the same components of the ECM. When brain slices are treated with ChABC, the effective diffusion coefficient has been shown to increase; however, the degree of degradation may not be sufficient enough for a ML model to detect differences in microstructural changes. The loss of PNNs due to ChABC treatment may also result in neuronal cell death, an inflammatory response, and activation of cells such as microglia[1], which could alter the ECS and ECM, mitigating the effects of the loss of ECM structure. ECM degradation may not be severe enough to cause the statistical features to be different for many of the nanoparticle trajectories. We see this highlighted when looking at Y-scrambled model results and the SHAP values, as the best XGBoost model accuracy was only 19% above random guessing, and only one feature (mean Deff1) had a high impact on the model.

Studies of OGD treatment in rodent brain slices have shown clear differences in diffusion between HC and OGD conditions. OGD treatment has shown an increase in the effective diffusion coefficient[96,97], as well as changes to the distribution of diffusion modes and ECM pore

sizes[97]. As these measurements are all made from the statistical features that are related to the mean-squared displacement that the model is trained with, it is unsurprising that mean Deff1 and mean alpha were important for the cortex data, while mean Deff1 and mean trappedness were used for both OGD conditions in the region data. Unlike the age, region, and treatment data sets, the top SHAP feature for the OGD data set in both regions was not the mean effective diffusion coefficient, but rather the mean fractal dimension feature, which takes a value near 1 for straight trajectories and direction motion, near 2 for random, Brownian diffusion, and 3 for constrained trajectories[152]. One possible explanation is that changes to the fractal dimension of the trajectories are related to conditions of cytotoxic and oxidative stress. OGD slices have greater cytotoxicity[97], which could lead to less cell density and straighter, less-confined nanoparticle motion in the OGD conditions compared with HC, as well as the age and region data sets.

Regional differences in the brain ECS also seem to play a role in the SHAP analysis of the XGBoost models trained on the OGD data set, as each of the six classes had a unique subset of top features. The difference in the top 5 features between the cortex and striatum for both the 0.5 h OGD condition and the 1.5 h OGD condition suggests that XGBoost models are able to detect regional differences in the ECS environment after OGD exposure. Regional differences in features due to OGD exposure align with regional differences of diffusion parameters in the ECS due to hypoxia, namely volume fraction and tortuosity. Volume fraction refers to the percentage of volume of the brain ECS relative to the volume of the entire tissue, while tortuosity measures the degree of hindrance to diffusion in tissue relative to free medium. In the striatum of adult rats, volume fraction has been shown to decrease due to hypoxia with no change to tortuosity[87], while in the cortex volume fraction has been shown to decrease while tortuosity increases[153].

A benefit of training XGBoost models on MPT data from OWH slices is that other modalities of data are collected, allowing for comparison of changes to the extracellular environment and other impacts of disease. OGD is known to effect microglia populations[154], and cellular-extracellular interactions may influence the environment through which nanoparticles are diffusing. Previous work showed that the morphology of microglia became more heterogeneous compared with a healthy microglia population, as well as a reduced overall number of microglia[97]. A study looking at changes to microglia over the course of 48 h shows changes to morphological parameters such as perimeter, area, circularity, and aspect ratio differed from normal conditions[144]. The reduced density of microglia due to OGD and change in shape in response to disease could explain the high values of features such as mean straightness in the cortex and mean efficiency in the striatum were important to OGD conditions, where reduced cellular density would reduce hindrance to diffusing nanoparticles. Microglia may also contribute to differences in important features across regions. A study in ex vivo ferret brain treated with OGD found region-dependent changes to microglia morphology features such as perimeter, circularity, and area across the cortex, corpus callosum, hippocampus, basal ganglia, thalamus, and subcortical matter[114]. While it is unclear whether microglia impact the SHAP features in this study, future studies may collect particle tracking data and microglia or other cell morphology data from the same OWH slice to better understand the relationship between nanoparticle diffusion and cellular changes under pathological conditions.

The importance of locally averaged features across all four data sets indicate that local averaging is a significant contributor to model performance and can be beneficial to include in future MPT ML work. It may also highlight that it is not individual trajectories that provide robust information to a data set, but the distribution and diversity of nanoparticle motion within a

given subspace. Research into the structure of the brain ECS has shown there to be void spaces connected via tortuous channels[12,140] and reservoirs of space next to cells[155]. As noted in McKenna et al.[29], it is likely that neighboring nanoparticles diffusing in these voids will be experiencing nearly identical environments and have similar diffusive behavior, while trajectories moving in an ECS channel of varying width will have different diffusive behavior. The ECS is also known to vary across age, brain region, and disease[12]. Locally averaged features as the top feature across all four data sets supports the idea that these features are capturing changes in the motion of neighboring nanoparticles resulting from structural differences in the ECM.

One limitation in this study is our identification of classes for each data set that are not able to be differentiated with high accuracy with the chosen ML models. Past research has shown that a deep learning approach can be used for nanoparticle trajectory classification tasks by applying a convolutional neural network to the raw trajectory data[156]. For each of these data sets, future work can investigate whether or not a deep learning approach on raw trajectory data, as opposed to the statistical features used in this study, can improve the accuracy of predictions on classes with which these current methods struggle. Synthetic data can also be generated using a generative adversarial network deep learning approach, which has been shown to improve convolutional neural network accuracy in medical classification tasks[157]. The mechanism relating locally average features to specific structural and microenvironmental changes also remains unclear. Future work could combine MPT with live-slice staining and imaging to determine how cellular- and protein-level changes influence nanoparticle diffusion, both at the individual trajectory level and over locally averaged domains. ML integration into MPT data analysis could also be applied in a nonbrain context, such as making predictions on nanoparticles moving in

other biological environments such as the mucosal membrane[157], or for tracking the diffusion of viruses and viral vectors[158]. While our analysis indicates that XGBoost can be used to predict between healthy and disease states, we are unable to directly relate differences in the most important features between healthy slices and OGD slices directly to the known changes due to OGD exposure. Future work will incorporate an increased amount of data relating to the disease condition to find correlations between features extracted from MPT experiments and macroscopic changes to the ECS.

3.5 CONCLUSION

We outline a methodology to apply data science and ML tools to MPT data to probe underlying biological changes using four distinct experimental data sets. While MPT has long been a technique used to understand complex biological environments, our methodology increases the insights extracted from a given MPT data set. Specifically, we validate the use of supervised learning and feature importance techniques by detecting microenvironmental changes in the brain ECS that align with previous characterizations of age and regional differences in tissue. We then demonstrate that XGBoost and SHAP can be applied to MPT data collected in models of disease to detect specific changes to the ECS microstructure based on treatment condition, treatment exposure time, and regional responses to injury.

CHAPTER 4 AGE, SPECIES, SEX, AND REGION DEPENDENT MORPHOLOGICAL FEATURES OF MICROGLIA

This chapter is being prepared for publication, with contributions from Nels Schimek, Hawley Helmbrecht, Teng-Jui Lin, Phuong Nguyen, Mia Onodera, Kylie Correy, Thomas Wood, Pernilla Svedin, Carina Mallard, Julie Wixey, Kirat Chand, Nirnath Sah, Sujatha Kannan, Katherine Prater, and Elizabeth Nance.

4.1 Introduction

Microglia, the immune cells of the brain, are major cells of interest during neurodevelopment due to their role in brain maturation, function, and injury response[159]. During brain maturation, microglia regulate neuronal circuit development through synapse pruning, debris clearing, and cell death or proliferation signaling[160]. Dysfunctional microglia during neurodevelopment are associated with various diseases and disorders, including autism spectrum disorder[161], schizophrenia[161], hypoxic-ischemic encephalopathy[114,162], and cerebral palsy[163]. During adulthood, microglia play a critical role in homeostasis[164], in particular through self-renewal[165], modulating synapse activity[166], and responding to acute injury[129] or neurodegenerative disease[167]. Microglia are heavily involved in aging[168], neuroinflammation[168], and neurodegenerative diseases including Alzheimer's disease[169] and Parkinsons disease[170].

A variety of methods exist to characterize microglia. Advances in transcriptomic methods have enabled characterization of changes in microglia gene expression at single cell resolution, such as through single cell RNA sequencing[171] and spatial transcriptomics[172,173]. Measuring microglia activation can be quantified by immunohistochemistry and positron emission tomography[174]. Electron microscopy has been used to relate spatial transcriptomics data and structural features of microglia[173]. Morphological characterization of microglia can be done

through immunohistochemical staining and fluorescent staining and imaging, although no one standard approach currently exists in the field.

Quantifying microglia morphology has included a wide range of methods. Extracting features can be done through manual processes, semi-automated processes[129,128], or fully automated methods[175,125]. Extracted features typically fall under categories of geometric values like area, perimeter, or aspect ratio, or calculations from the images such as number of processes or lacunarity. Categorization into types of microglia can be done using supervised[127] or unsupervised machine learning methods[176,121], ranging from linear components analysis to deep learning[177,123]. Analyses, then, can include changes in the distribution of the categories and changes to the geometric values. While many studies of microglia focus on clinical and translational applications, these studies typically only include a single species, reducing the potential translational aspect of the findings when relating microglia changes to aging, sex, or regional comparisons.

Multi-species analysis of microglia have also centered gene expression characterization[178,179] not morphology. Recent studies have analyzed microglia morphology in rats and sheep but with a focus on aging[180]. There also exists a lack of morphological studies in species with gyrified brains during neurodevelopment. In this study, we bridge this gap by characterizing healthy microglia morphology across six species. First, we compare differences between species at term and at sexual maturity. Second, we compare region and sex-based changes of microglia during development across species. Finally, we compare region and sex-specific differences across species at sexual maturity between cortex and corpus callosum to investigate white versus gray matter differences.

4.2 Materials and Methods

4.2.1 Tissue sample acquisition.

Tissue samples were acquired from a group of national and international collaborators: ferret tissue from Dr. Tommy Wood, University of Washington; pig tissue from Dr. Julie Wixey, University of Queensland; rabbit tissue from Dr. Sujatha Kannan, Johns Hopkins University; rat tissue from the Nance lab, UW; human tissue from the brain bank at the Alzheimer's Disease Coordinating Center via Dr. Katie Prater, UW; and mouse tissue from Dr. Carina Mallard, University of Gothenburg.

Table 4.1 Tissue collection and sample preparation

Species	Animals (P = postnatal day)
Rat	P13: Healthy male (n=3) and healthy female (n=3). P70: Healthy male (n=3) and healthy female (n=3)
Mouse	P12: Healthy male (n=3) and healthy female (n=3). P45: Healthy male (n=3) and healthy female (n=3)
Ferret	P21: Healthy male (n=3) and healthy female (n=3)
Pig	P1: Healthy males (n=3) and females (n=3). Adult: Healthy females (n=2)
Rabbit	P49: Healthy males (n=3) and healthy females (n=3)
Human	Young adult males (n=3) and females (n=3)

4.2.1 Immunofluorescent staining of microglia

A primary antibody solution (1:250) rabbit anti-Iba in PBS g++, a solution of PBS (Corning), 1% Triton X-100 (Sigma), and goat serum (Thermo Fisher) was applied to each slide for 5 hours. Slices were washed with 1000 *u*L three times for 3 minutes. A secondary antibody solution (1:500) of goat anti-rabbit IgG conjugated to AlexaFluor488 (Fisher) was prepared in a solution of PBS (Corning) and 1% Triton X-100 (Sigma), which was applied to each slide for 2 hours. Slices were then washed in 1000 *u*L PBS three times for three minutes. Nuclear staining was done with (1:999) DAPI in PBS applied to each slide for 15 minutes. Slides were then washed in

1000 *u*L pbs three times for three minutes. After drying, slides were mounted with Daki fluorescent mounting media.

Table 4.2 Staining procedure for slices of each species.

Species	Method
Mouse	Followed procedure outlined in Materials and Methods
Rat	Followed procedure outlined in Materials and Methods
Rabbit	Followed procedure outlined in Materials and Methods
Pig	Staining completed by collaborators at the University of Queensland according to the same staining protocol in Materials and Methods with an AlexaFluor 568 instead of AlexaFluor 488
Ferret	Staining completed by the University of Washington Histology and Imaging core with the same protocol outlines in Materials and Methods
Human	Staining completed by the Prater lab using the methods described in Prater et al[181]

4.2.2 Image acquisition and pre-processing

A Nikon A1R confocal microscope was used for imaging. For each slice, three Z-stack images were captured for each region analyzed except the hippocampus. Four images were captured for each slice in the hippocampus from the CA1, CA2, CA3, CA4 (if identifiable) and DG regions. All images were captured at 60x magnification without zoom using the Alexa Fluor 488 (Alexa Fluor 568 for pig samples) laser channels with the same settings including pinhole and gain across all images. Z-stack images from each ROI were converted from .nd2 file format to .tiff file format. Cells in images were segmented using the Li threshold from Scikit-Image in Python. Objects smaller than 25 pixels were removed and holes were filled. Segmented cell images were saved as .png files.

4.2.3 Microglial morphology analysis

Geometric features for each cell in each image were calculated using the regionprops function from Scikit-Image[182] in Python. The geometric features calculated were area, convex area,

bounding box area, perimeter, major axis length, minor axis length, circularity, solidity, extent, eccentricity, and aspect ratio. Morphological shape modes were determined using the VAMPIRE methodology (Visually Aided-Morpho-phenotyping Image Recognition)[130]. Segmented images are given to VAMPIRE and N coordinates equally spaces across each cell contour are determined, normalized, and aligned. For this study, we used an N of 50. Principal components analysis (PCA) is applied to the shape coordinates for dimensionality reduction. Shape objects are then reconstructed from the eigen-shape vectors from PCA. Finally, K means clusters analysis is used to separate shapes into N distinct shape mode clusters.

4.2.4 Cluster Estimation

To estimate the number of distinct morphologies across all species, a 5-fold cross validation was run at K cluster values of 2 to 30 clusters, repeated 20 times. For each K, silhouette score, Davies-Buildin index, Inertia, and BIC were calculated, plotted, and used to estimate potential cluster values. ARI, pairwise contour distances, mean CV of pairwise distances, and Mean Jaccard metrics were calculated across each of the 20 seeds for each value of K and plotted to determine the consistency of each K. After determining potential K clusters based on the metrics, the mean contours from each of the 20 seeds at each K were overlaid and visualized to determine at what K models trained on different subsets of the data would begin disagreeing on what morphologies were present.

To make changes to microglia shape mode distributions interpretable, for each K that was within a standard deviation of the of the lowest DB score and the calculated elbow, we tested for statistical significance between the animal level means of geometric feature of each shape mode using the Kruskal-Wallis test with Dunn's test for post hoc testing and Bonferroni for multiple comparisons correction.

Table 4.3 Metrics used to estimate the number of clusters to use for VAMPIRE.

Metric	**Evaluation**
Silhouette Score	Values range from 0 to 1, with higher values being indicative of better clustering
Davies Bouldin Index	Values range from 0 to infinity, with lower values
Inertia Elbow	Look for "elbow" in the data, where the drop in inertia plateaus after an initial steep to decrease as K increases
Gap statistic	Higher values of gap statistic indicate that the clustering structure is more distinct from what would be expected by chance

4.2.5 Calculation of geometric features medians

The median values and 95% confidence intervals for the geometric features were calculated using 1000 bootstrapped where data for each iteration was generated by sampling with replacement.

4.2.6 Linear mixed effects model comparing geometric features at term and at sexual maturity

Linear mixed effects models for comparing geometric features across species at term and sexual maturity were done using the LMER package. A linear mixed effects model with fixed effects for the geometric feature was built to estimate the fixed effect of the feature for each species when accounting for fixed effects of sex and region and random effects of slice and image. Testing for statistical significance between two species was done using the LmerTest package, with Bonferroni correction used to correct for multiple comparisons. A p-value less than 0.05 was considered statistically significant.

To compare geometric features within species during development, a linear mixed effects model was built to estimate the fixed effect of each geometric feature for the term and sexual maturity ages for each region with random effects for slice and image.

4.2.7 Pairwise comparison for difference between Shape modes

Differences across shape modes for seven features – circularity, solidity, area, eccentricity, aspect ratio, major axis length, and minor axis length – were assessed using the Kruskal-Wallis test. To determine differences between specific shape modes, pairwise post-hoc comparisons using Dunn's test with Bonferroni correction for multiple comparisons were used. Bonferroni-adjusted p-values less than 0.05 were considered statistically significant.

4.2.8 Effect size calculation for cortex vs corpus callosum

A linear mixed effects model was fit for six features – solidity, circularity, aspect ratio, area, major axis length, and minor axis length – with a fixed effect of region and random effects of slice and image for each species × sex × feature combination. The species included mouse, rat, pig, and human, all at sexual maturity, and the regional comparison was between the cortex and corpus callosum. P values for each model were calculated by the Satterthwaite degrees of freedom approximation, with Benjamini-Hochberg correction for multiple comparisons. Adjusted p-values < 0.05 were considered statistically significant.

4.3 Results and Discussion

4.3.1 Geometric feature analysis identifies distinct morphologies across species and age

We first segmented all microglia and analyzed basic geometric features across species at equivalent time points to explore the qualitatively subtle microglial morphology differences (**Figure 4.1**). Rabbit and rat had the largest microglia by area, with rabbit having the highest median measures of bounding box area, convex area, perimeter, and major and minor axis lengths. At sexual maturity, mouse, pig, and human all had similar median measures of size, but

at term the pig microglia had lower median values across bounding box area, convex area, perimeter, and major axis length. Ferret had the smallest microglia at term, with the lowest median values of all three measures of area, perimeter, and major and minor axis lengths. At term, ferret and pig microglia had higher median values of extent, solidity, and circularity compared to mouse and rat microglia. Pig and human at sexual maturity had the highest median values of aspect ratio.

Due to the availability of samples at both time points, we have the most extensive dataset from the mouse and the rat at human-term equivalent and sexual maturity ages (mouse: p12 and p45 and rat: p13 and p70, respectively). The representative images (**Appendix B.1**) show differences in microglial branching complexity. Both rats and mice exhibit extensive branching, with the rat qualitatively appearing to exhibit larger cell somas. Additionally, the microglia in the hippocampus and cortex were densely populated across groups and the cerebellum and corpus callosum qualitatively displayed less dense microglial signals in both the mouse and rat. In the rat p70 rat corpus callosum, microglia appear to align in directionality.

In representative images from the ferret and pig, microglia still display highly branched cells where the pig microglia appear to be more tortuous compared to the ferret, and the ferret exhibits more pronounced soma (**Appendix B.2**). The rabbit samples display extensively branched microglia with some directionality in the corpus callosum with higher aspect ratio microglia. The rabbit cortex and striatum display more radial branching. The rabbit corpus callosum and cerebellum appear to have lower microglial densities.

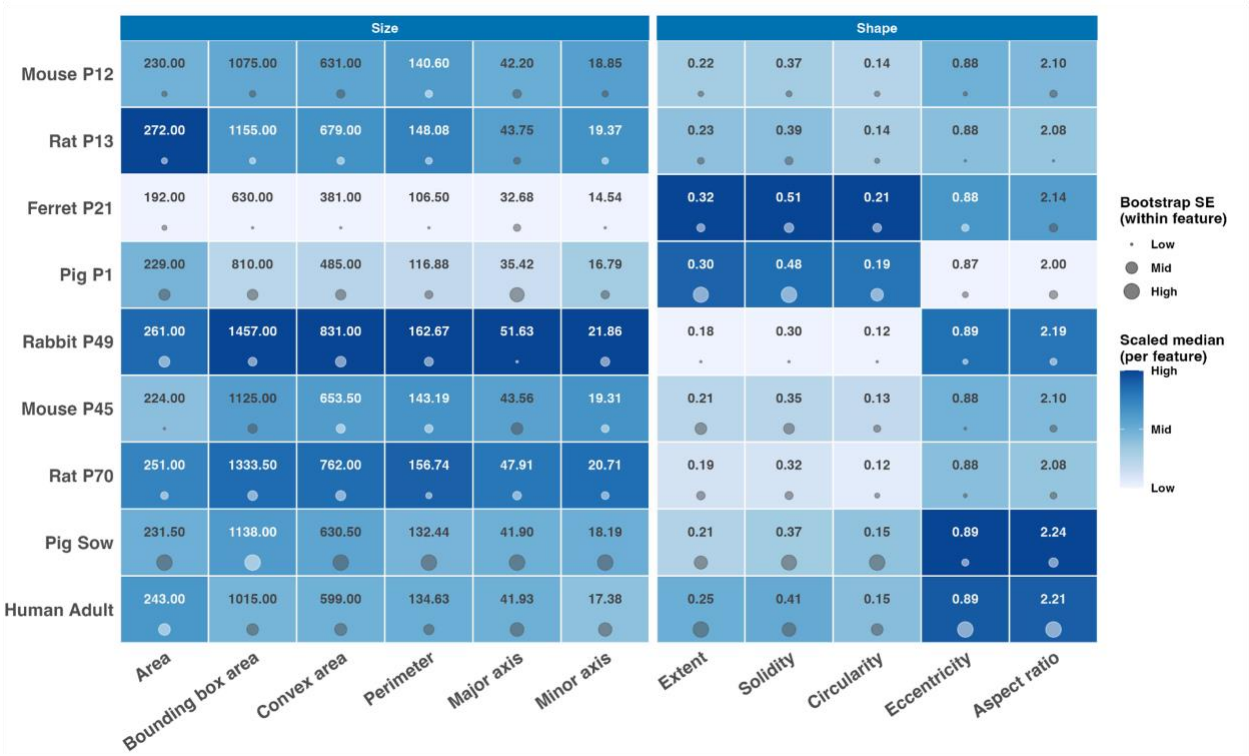

Figure 4.1 Geometric feature analysis across term equivalent and human sexual maturity equivalent

Eleven geometric features – area, bounding box area, convex area, perimeter, extent, solidity, circularity, eccentricity, aspect ratio, major axis length, and minor axis length - for the mouse, rat, pig, ferret, rabbit and human are displayed at the human-term equivalent age or the human sexual maturity equivalent age. The values in each box are the median value of the morphological feature for that species and age. Median values were calculated by bootstrapping over 1000 iterations with replacement at the animal level. Darker blue indicates that the scaled median value is high compared to other species, while light blue indicates a low scaled median value. The bootstrapped standard errors are indicated by the gray dot under each value, with a larger circle indicating larger standard errors. With 1000 bootstraps the range of values captured by the median value +/- the standard errors are the 95% confidence intervals for the median value of the feature.

To determine which parameters differed between species, we used a linear mixed effects model to test for differences in parameters between each species at term and at sexual maturity, accounting for fixed effects of region and sex and random effects of slice and image (**Figure 4.2**). At term, we did not detect differences between mouse and pig, suggesting that the differences in microglia parameters between these species may be region or sex dependent. Mouse and rat only differed in measures of area, suggesting that while the size of microglia

between these species may be different, the actual morphologies present are similar. Mouse and rat were both significantly different from the ferret across most morphological parameters. Ferret microglia appear to be smaller compared to both rat and mouse microglia since convex area and bounding box are smaller and statistically different in the ferret, and more amoeboid and less branch as they had higher circularity and solidity. Rat and pig also differed in measures of area and circularity. Rat microglia were larger in measures of area compared to pig microglia with higher aspect ratio and eccentricity, while pig microglia had higher circularity and solidity. At sexual maturity the only species that had statistically significant differences were the mouse and rat, where rat microglia had higher measures of area and perimeter, suggesting that similar to rat and mouse at term the primary difference of microglia between the two species is size rather than branching.

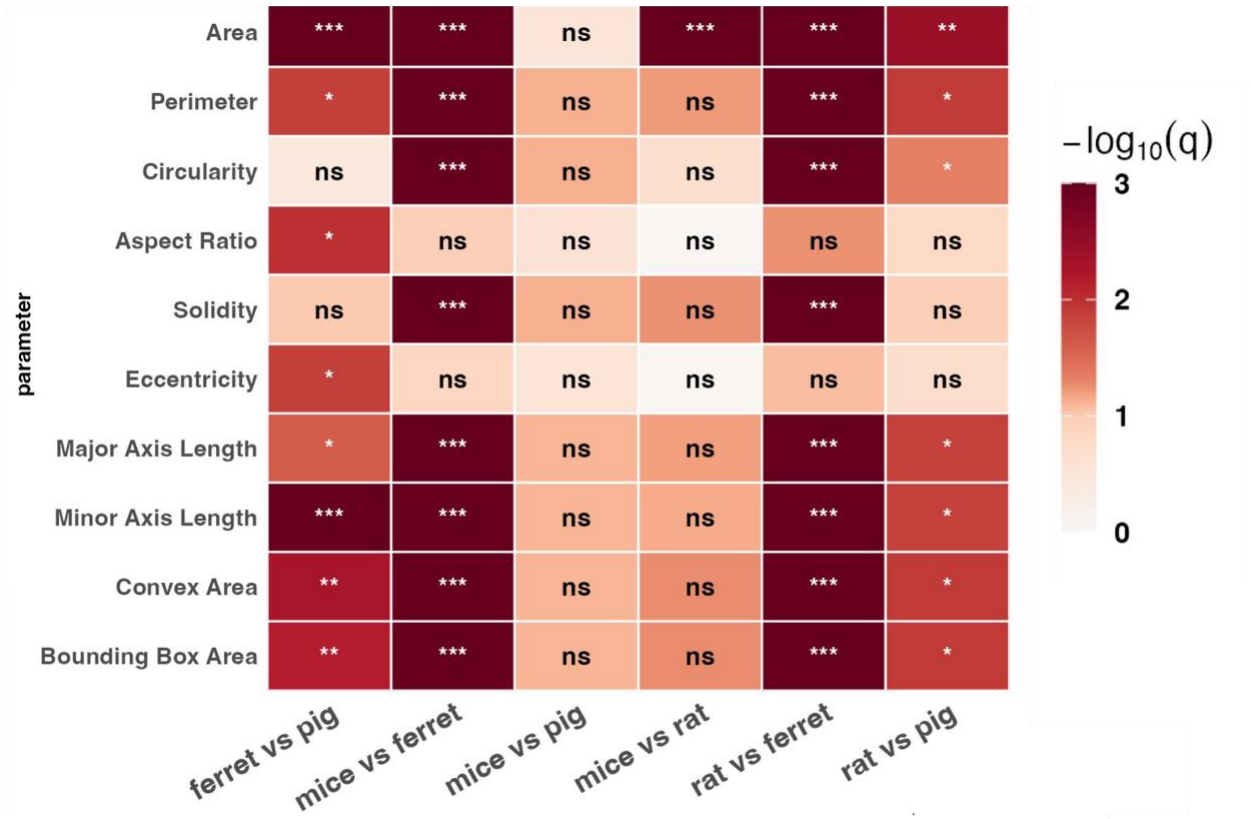

Figure 4.2 Linear mixed effects model results for comparing geometric features between species at term.
Heatmap of pairwise statistical comparisons of the difference in estimated means for 11 geometric features was tested for statistical significance between the mouse, rat, ferret, and pig. Each cell represents the significance between two species for a given morphological feature. Color intensity represents the degree of statistical significance: * $p < 0.05$, ** $p < 0.01$, *** $p < 0.001$, ns = not significant

4.3.2 Determination of optimal number of shape mode clusters for VAMPIRE

Four metrics – inertia, gap statistic, Davies-Bouldin, and Silhouette score - were used to determine the potential range of clusters to use for VAMPIRE. Determining K based on inertia is done by visual assessment of an elbow, where the inertia value drops rapidly with K before plateauing. Over the range of K values for our data, there was no clear elbow and instead a gradual decrease in inertia. (**Figure 4.3A)**. A higher value of the gap statistic suggests better clustering, but similarly the gradual increase of the curve indicates the increase in the value is not

actually finding the optimal K (**Figure 4.3B)**. For the Davis-Bouldin plot, the values near the minimum for 5, 6, and 7 clusters suggests a potential range that should be evaluated (**Figure 4.3C**). However, the range of Davies-Bouldin values is narrow from the maximum value near 2.8 to the minimum value at 2.2, suggesting that the metric is not capturing large improvement in clustering. Similarly, the silhouette value starts at 0.11 (**Figure 4.3D**) where the maximum value using the silhouette metric is 1.0, suggesting that even though the value decreases with K, the changes are not indicative of significantly worse clustering. Overall, these narrow ranges of all metrics suggest that using these methods may be useful for determining a potential range of K values, but do not provide a specific, optimal K for our data.

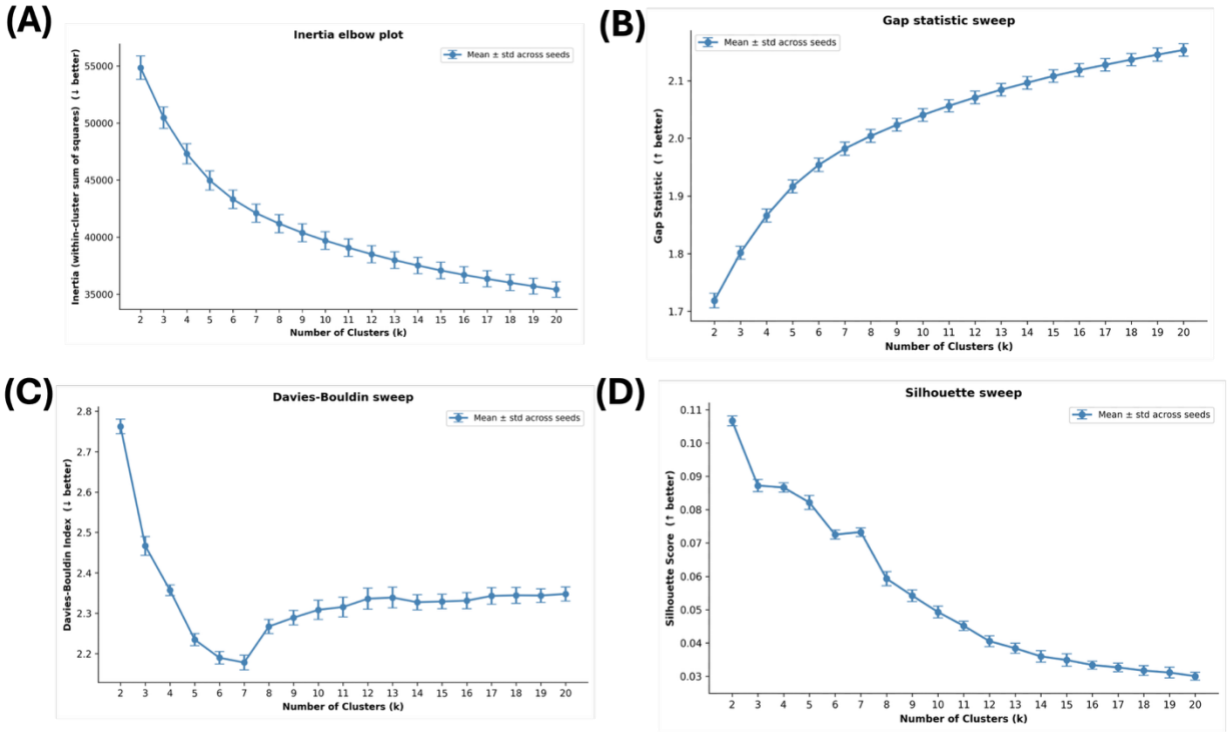

Figure 4.3 Cluster metrics for VAMPIRE shape modes from 2 to 20 clusters

Evaluation of clustering quality metrics across K = 2 to 20 clusters to determine the optimal number of microglia shape modes. (A) Inertia elbow plot showing within-cluster sum of squares decreasing monotonically as K increases. (B) Gap statistic increasing monotonically with K, with

no clear peak. (C) Davies-Bouldin index reaches a minimum around K = 7. (D) Silhouette score decreasing monotonically with K, favoring lower values of K. All metrics are shown as mean ± standard deviation across 20 random seeds.

One of the benefits of microglia morphology data is the inherent ability to visualize the morphologies. By visualizing the morphological shape modes determined by VAMPIRE at each K over multiple runs on different subsets of the data, it is possible to determine at which K values there are distinct shape modes, as well as how adding another cluster changes the morphologies determined by VAMPIRE. With 4 clusters, there are four morphologically distinct shape modes (**Figure 4.4A**). At 5 clusters, there were two pairs of shape modes – SM2 and SM5, and SM3 and SM4 – that were visually similar (**Figure 4.4B**), suggesting that the model is dividing shape modes instead of finding a new one. Going to 6 shape modes does add a distinct shape mode, SM7 (**Figure 4.4C),** compared to the shape modes at 5. However, this shape mode is similar to SM3 from the four-cluster model. At 7 clusters, multiple shape modes become unstable, highlighting that the model is not finding distinct shape modes (**Figure 4.4D**). For the final VAMPIRE, we chose to use 4 clusters as the shape modes show the greatest visual distinction.

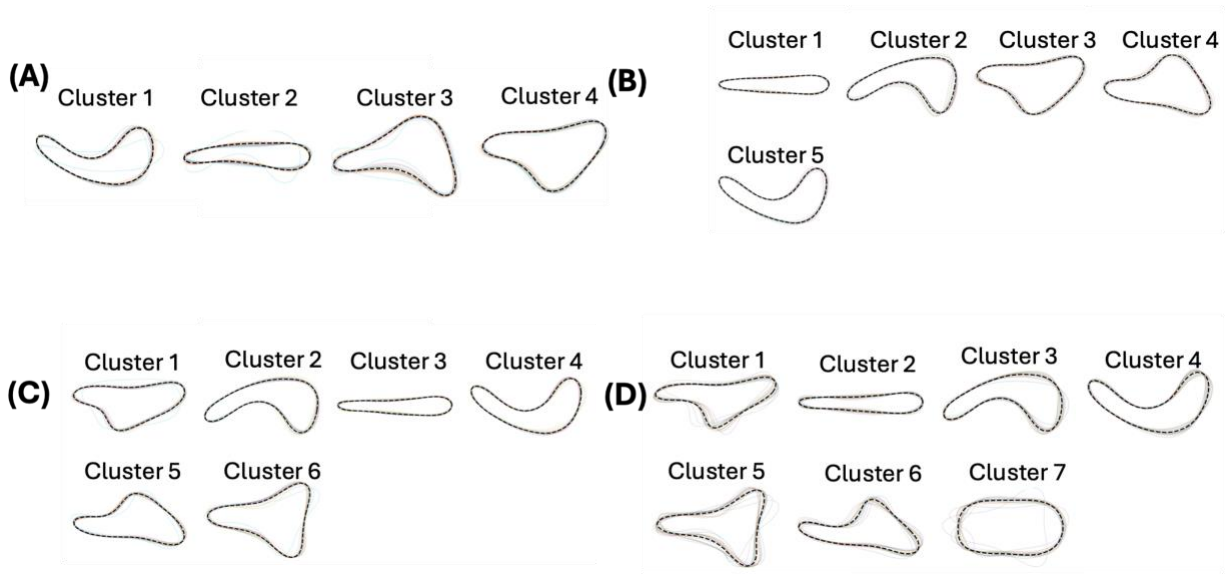

Figure 4.4 Mean and overlaid contours across 20 seed for K values of 4, 5, 6, and 7

Representative mean cell shapes for each cluster identified by VAMPIRE analysis at K = 4 (A), K = 5 (B), K = 6 (C), and K = 7 (D). Dashed lines indicate the mean cell boundary for each shape mode, with shaded regions representing the mean cell outlines across 20 random seeds used during clustering.

To investigate the morphological differences in the four shape modes, we tested for statistical significance of all features between each pair of shape modes. (**Figure 4.4A**) and visualized 7 morphological features on radar plots **(Figure 4.4B).** SM1 was visually most similar to SM2 but the differences in eccentricity and aspect ratio were statistically significant between the two shape modes. SM1 had the lowest aspect ratio and eccentricity and the highest minor axis length, indicating a more ameboid shape. SM3 had a higher aspect ratio and eccentricity compared to SM1 and SM2 but was lower than SM4 for both parameters. SM4 additionally had the highest major axis length and lowest minor axis length. Circularity was a key parameter for distinguishing between SM1 and SM2 compared to SM3 and SM4, where SM1 and SM2 both had higher circularities, further indicating a more ameboid shape.

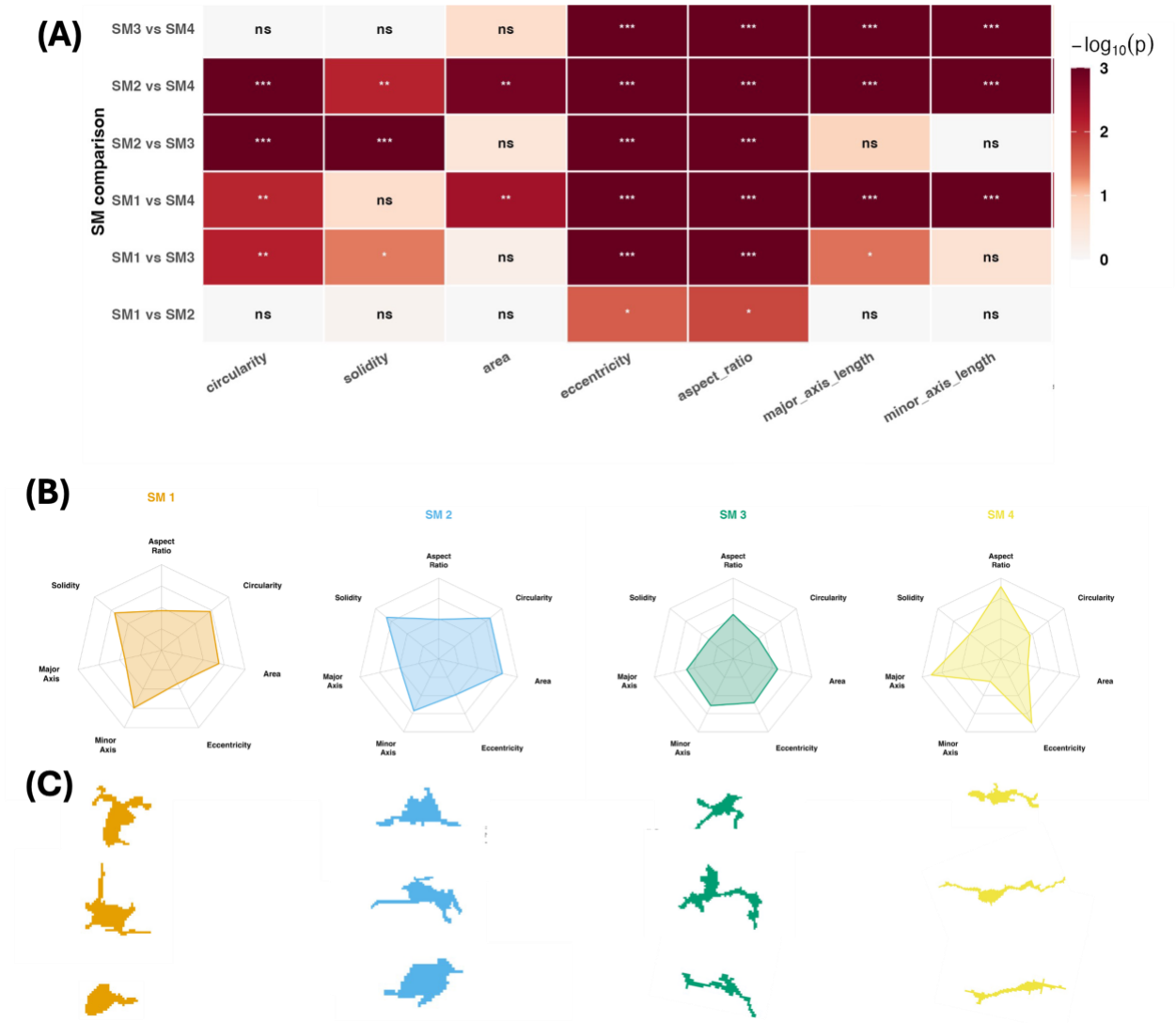

Figure 4.5 Mean contours and morphological parameters of VAMPIRE shape modes

(A) Statistical analyses of features between each shape mode, where the pairwise test was calculated between animal level means of each feature. Means for each feature for each shape mode were calculated using a linear mixed effects model accounting for fixed effects. Bonferroni correction for multiple comparisons was applied when testing for statistical significance. P value < 0.05 was considered statistically significant **(B)** Radial plots of 7 features – solidity, aspect ratio, area, circularity, eccentricity, major axis length, and minor axis length – for each of the four shape modes. (**C**) Example masks of microglia from each of the four shape modes determined by VAMPIRE.

4.3.3 Sex and Region based changes to Microglia during development.

To further investigate the role of microglia and the effect of sex and region during development, we analyzed the change in microglia features from term equivalent to sexual maturity across regions and separated by sex in the mouse, rat, and pig. We used a linear mixed model approach to determine whether the mean of each of the ten geometric features were significantly different in each region between animals at term equivalent and at sexual maturity (**Figure 4.6)**. We then calculated the effect size of the difference in the means to see whether features were higher or lower at each time point (**Figure 4.6)**.

By analyzing trends in which regions showed changes in morphological parameters, we can assess similarities and differences during development across species of the same sex and between species of different sexes. Male and female mice showed very different developmental trends in terms of critical regions (**Figure 4.6A, Figure 4.6B**). Only the cortex in female mice had multiple morphological parameters that were significantly different between the two ages, while in male mice the thalamus, hippocampus, striatum, and pallidum all showed significant changes in morphological parameters. The regional variation was less stark comparing the data between male and female rats. In the male rat the most changes were seen in the thalamus, hippocampus, striatum, and cerebellum (**Figure 4.6C)**, while in the female rat the most differences were seen in the hippocampus, striatum, and corpus callosum (**Figure 4.6D)**. The trends during development in the striatum were similar between the female pig and rat, where solidity and extent were both lower at the older time point (**Figure 4.6E)**. Comparing the female pig and mouse data, area was higher at sexual maturity in the pallidum in both species.

While the regions with differences in morphological features varied, the direction of the change in the means from term equivalent to sexual maturity was consistent. Solidity, extent, and circularity were all lower in the sexual maturity timepoints in the female rat and male mouse and

rat. Major axis length, minor axis length, bounding box area, and convex area were higher at the sexually mature time points. However, these trends were the opposite in the female rat cortex data. Solidity and extent were both higher at p45 and circularity, bounding box area, convex area, and major axis length were all lower.

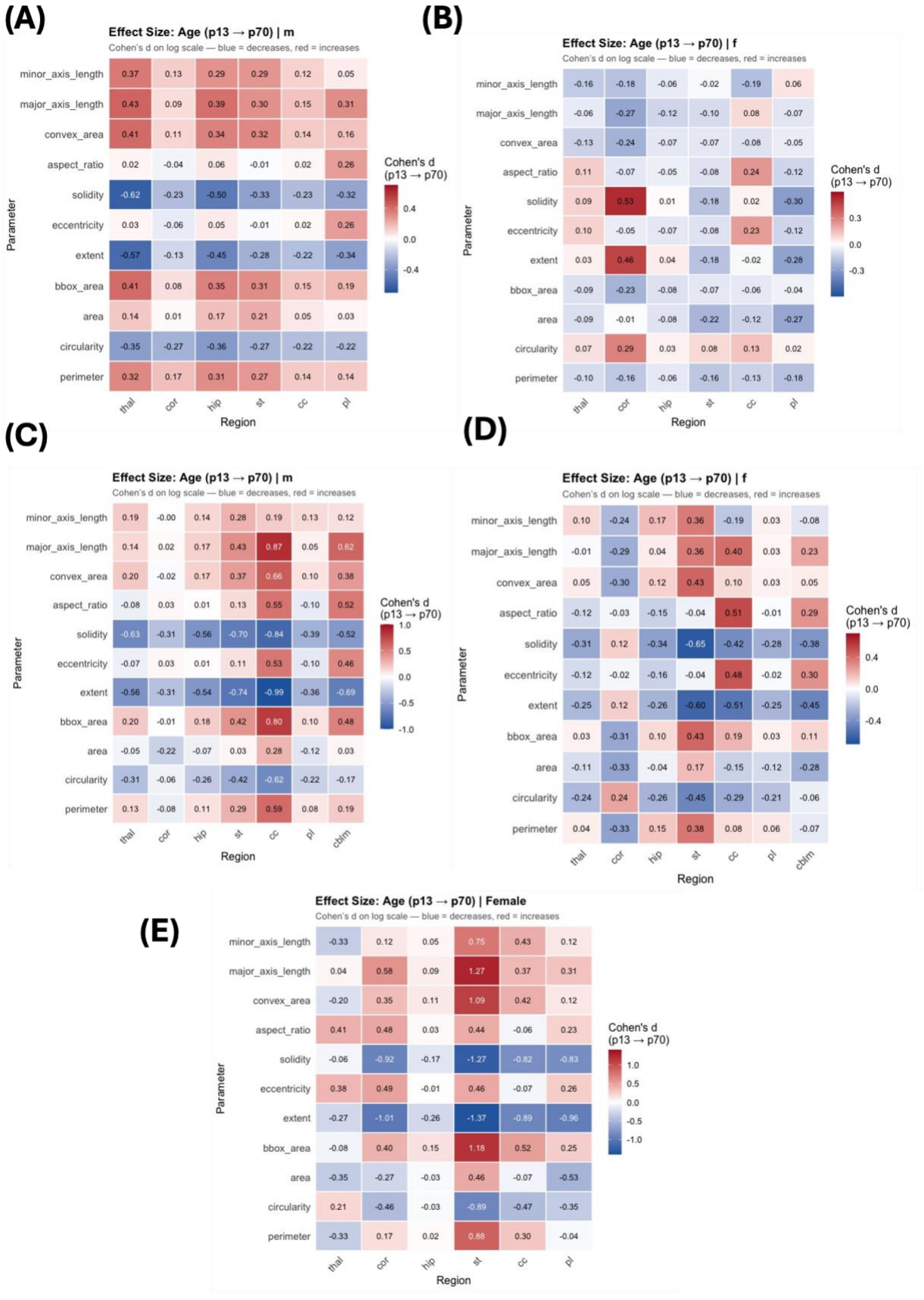
(A)
Effect Size: Age (p13 → p70) | m
Cohen's d on log scale — blue = decreases, red = increases
minor_axis_length 0.37 0.13 0.29 0.29 0.12 0.05
major_axis_length 0.43 0.09 0.39 0.30 0.15 0.31
convex_area 0.41 0.11 0.34 0.32 0.14 0.16
aspect_ratio 0.02 -0.04 0.06 -0.01 0.02 0.26
solidity -0.62 -0.23 -0.50 -0.33 -0.23 -0.32
eccentricity 0.03 -0.06 0.05 -0.01 0.02 0.26
extent -0.57 -0.13 -0.45 -0.28 -0.22 -0.34
bbox_area 0.41 0.08 0.35 0.31 0.15 0.19
area 0.14 0.01 0.17 0.21 0.05 0.03
circularity -0.35 -0.27 -0.36 -0.27 -0.22 -0.22
perimeter 0.32 0.17 0.31 0.27 0.14 0.14
Parameter
thal cor hip st cc pl
Region
Cohen's d (p13 → p70)
0.4
0.0
-0.4
(B)
Effect Size: Age (p13 → p70) | f
Cohen's d on log scale — blue = decreases, red = increases
minor_axis_length -0.16 -0.18 -0.06 -0.02 -0.19 0.06
major_axis_length -0.06 -0.27 -0.12 -0.10 0.08 -0.07
convex_area -0.13 -0.24 -0.07 -0.07 -0.08 -0.05
aspect_ratio 0.11 -0.07 -0.05 -0.08 0.24 -0.12
solidity 0.09 0.53 0.01 -0.18 0.02 -0.30
eccentricity 0.10 -0.05 -0.07 -0.08 0.23 -0.12
extent 0.03 0.46 0.04 -0.18 -0.02 -0.28
bbox_area -0.09 -0.23 -0.08 -0.07 -0.06 -0.04
area -0.09 -0.01 -0.08 -0.22 -0.12 -0.27
circularity 0.07 0.29 0.03 0.08 0.13 0.02
perimeter -0.10 -0.16 -0.06 -0.16 -0.13 -0.18
Parameter
thal cor hip st cc pl
Region
Cohen's d (p13 → p70)
0.3
0.0
-0.3
(C)
Effect Size: Age (p13 → p70) | m
Cohen's d on log scale — blue = decreases, red = increases
minor_axis_length 0.19 -0.00 0.14 0.28 0.19 0.13 0.12
major_axis_length 0.14 0.02 0.17 0.43 0.87 0.05 0.62
convex_area 0.20 -0.02 0.17 0.37 0.66 0.10 0.38
aspect_ratio -0.08 0.03 0.01 0.13 0.55 -0.10 0.52
solidity -0.63 -0.31 -0.56 -0.70 -0.84 -0.39 -0.52
eccentricity -0.07 0.03 0.01 0.11 0.53 -0.10 0.46
extent -0.56 -0.31 -0.54 -0.74 -0.99 -0.36 -0.69
bbox_area 0.20 -0.01 0.18 0.42 0.80 0.10 0.48
area -0.05 -0.22 -0.07 0.03 0.28 -0.12 0.03
circularity -0.31 -0.06 -0.26 -0.42 -0.62 -0.22 -0.17
perimeter 0.13 -0.08 0.11 0.29 0.59 0.08 0.19
Parameter
thal cor hip st cc pl cblm
Region
Cohen's d (p13 → p70)
1.0
0.5
0.0
-0.5
-1.0
(D)
Effect Size: Age (p13 → p70) | f
Cohen's d on log scale — blue = decreases, red = increases
minor_axis_length 0.10 -0.24 0.17 0.36 -0.19 0.03 -0.08
major_axis_length -0.01 -0.29 0.04 0.36 0.40 0.03 0.23
convex_area 0.05 -0.30 0.12 0.43 0.10 0.03 0.05
aspect_ratio -0.12 -0.03 -0.15 -0.04 0.51 -0.01 0.29
solidity -0.31 0.12 -0.34 -0.65 -0.42 -0.28 -0.38
eccentricity -0.12 -0.02 -0.16 -0.04 0.48 -0.02 0.30
extent -0.25 0.12 -0.26 -0.60 -0.51 -0.25 -0.45
bbox_area 0.03 -0.31 0.10 0.43 0.19 0.03 0.11
area -0.11 -0.33 -0.04 0.17 -0.15 -0.12 -0.28
circularity -0.24 0.24 -0.26 -0.45 -0.29 -0.21 -0.06
perimeter 0.04 -0.33 0.15 0.38 0.08 0.06 -0.07
Parameter
thal cor hip st cc pl cblm
Region
Cohen's d (p13 → p70)
0.4
0.0
-0.4
(E)
Effect Size: Age (p13 → p70) | Female
Cohen's d on log scale — blue = decreases, red = increases
minor_axis_length -0.33 0.12 0.05 0.75 0.43 0.12
major_axis_length 0.04 0.58 0.09 1.27 0.37 0.31
convex_area -0.20 0.35 0.11 1.09 0.42 0.12
aspect_ratio 0.41 0.48 0.03 0.44 -0.06 0.23
solidity -0.06 -0.92 -0.17 -1.27 -0.82 -0.83
eccentricity 0.38 0.49 -0.01 0.46 -0.07 0.26
extent -0.27 -1.01 -0.26 -1.37 -0.89 -0.96
bbox_area -0.08 0.40 0.15 1.18 0.52 0.25
area -0.35 -0.27 -0.03 0.46 -0.07 -0.53
circularity 0.21 -0.46 -0.03 -0.89 -0.47 -0.35
perimeter -0.33 0.17 0.02 0.88 0.30 -0.04
Parameter
thal cor hip st cc pl
Region
Cohen's d (p13 → p70)
1.0
0.5
0.0
-0.5
-1.0

Figure 4.6 Morphological features across region per species

Heatmaps showing the change based on Cohen's D from early to mature timepoints across brain regions for morphological features in male mice **(A),** female mice **(B**), male rats **(C**), female rats **(D),** and female pigs **(E)** Color intensity reflects the magnitude and direction of change, with red indicating an increase and blue indicating a decrease in the feature value from term to sexual maturity.

A consistent trend in the SM data was that regions where the SM distribution was different between term and sexual maturity became less ameboid and more rod like (**Figure 4.7)**, and these regions agreed with the linear mixed model results. The combination of the linear mixed model results and the shape mode data suggest that the microglia morphologies critical for neurodevelopment are conserved across species, but the regions where these changes occur is based on sex and species. Our results suggest that the distribution of microglia morphologies is age dependent and follows similar patterns across species, where are more common at term and rod-like microglia are more common at sexual maturity.

Analysis of the transcriptome and morphology of developing microglia has found stages of microglia development[23,183], where microglia are ameboid-like at the start of development and become ramified at juvenile, early adult ages[184]. The parameter and shape mode changes we detected in the rat align with previous literature. In the cerebral hemisphere, morphological analysis of microglia from P1 to P30 showed that microglia shifted from round and ameboid to branched and ramified, with increases in convex hull area and decreased solidity[185]. A study of microglia in the developing rat cerebellum found that round, ameboid microglia decreased from P5 to P21, while microglia with thin processes increased beginning and P5 were the most common morphology at P21[186]. In the corpus callosum, the change from ameboid to branched, ramified was detected as well[187]. Our findings in the rat strongly align with these previous findings, where solidity was lower in the hippocampus, corpus callosum, and cerebellum while

measures of size increased. The increase in SM4 in the corpus callosum and cerebellum further highlights that microglia are more branched at sexual maturity and are more ameboid at term.

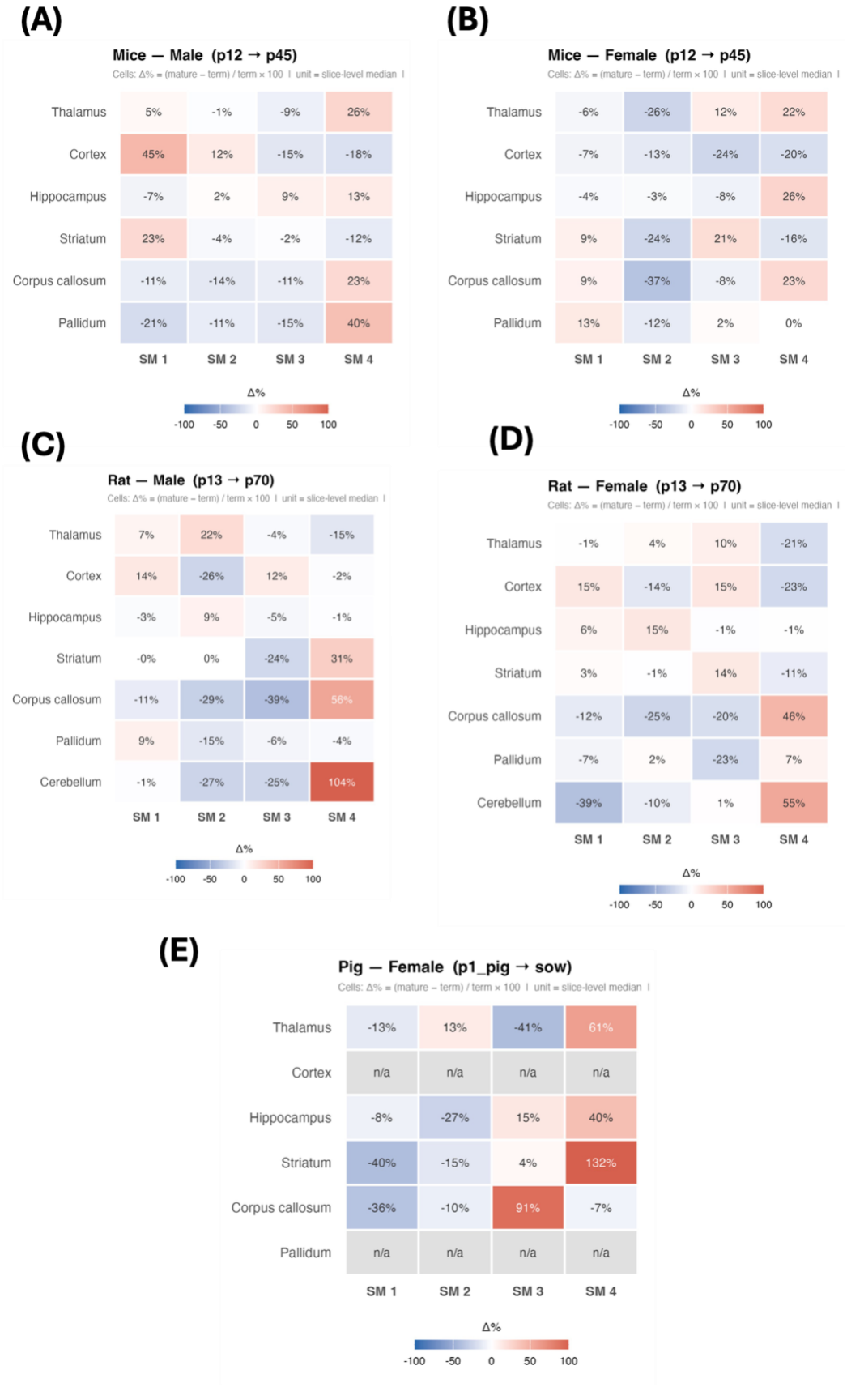
(A)
Mice — Male (p12 → p45)
Cells: Δ% = (mature − term) / term × 100 | unit = slice-level median |
Thalamus 5% -1% -9% 26%
Cortex 45% 12% -15% -18%
Hippocampus -7% 2% 9% 13%
Striatum 23% -4% -2% -12%
Corpus callosum -11% -14% -11% 23%
Pallidum -21% -11% -15% 40%
SM 1 SM 2 SM 3 SM 4
Δ%
-100 -50 0 50 100
(B)
Mice — Female (p12 → p45)
Cells: Δ% = (mature − term) / term × 100 | unit = slice-level median |
Thalamus -6% -26% 12% 22%
Cortex -7% -13% -24% -20%
Hippocampus -4% -3% -8% 26%
Striatum 9% -24% 21% -16%
Corpus callosum 9% -37% -8% 23%
Pallidum 13% -12% 2% 0%
SM 1 SM 2 SM 3 SM 4
Δ%
-100 -50 0 50 100
(C)
Rat — Male (p13 → p70)
Cells: Δ% = (mature − term) / term × 100 | unit = slice-level median |
Thalamus 7% 22% -4% -15%
Cortex 14% -26% 12% -2%
Hippocampus -3% 9% -5% -1%
Striatum -0% 0% -24% 31%
Corpus callosum -11% -29% -39% 56%
Pallidum 9% -15% -6% -4%
Cerebellum -1% -27% -25% 104%
SM 1 SM 2 SM 3 SM 4
Δ%
-100 -50 0 50 100
(D)
Rat — Female (p13 → p70)
Cells: Δ% = (mature − term) / term × 100 | unit = slice-level median |
Thalamus -1% 4% 10% -21%
Cortex 15% -14% 15% -23%
Hippocampus 6% 15% -1% -1%
Striatum 3% -1% 14% -11%
Corpus callosum -12% -25% -20% 46%
Pallidum -7% 2% -23% 7%
Cerebellum -39% -10% 1% 55%
SM 1 SM 2 SM 3 SM 4
Δ%
-100 -50 0 50 100
(E)
Pig — Female (p1_pig → sow)
Cells: Δ% = (mature − term) / term × 100 | unit = slice-level median |
Thalamus -13% 13% -41% 61%
Cortex n/a n/a n/a n/a
Hippocampus -8% -27% 15% 40%
Striatum -40% -15% 4% 132%
Corpus callosum -36% -10% 91% -7%
Pallidum n/a n/a n/a n/a
SM 1 SM 2 SM 3 SM 4
Δ%
-100 -50 0 50 100

Figure 4.7 Change in shape mode percentage during neurodevelopment

Heatmaps showing the percent change in microglia shape mode distribution (Δ%) from early to mature timepoints across brain regions and shape modes (SM1–SM4) in male mice **(A),** female mice **(B**), male rats **(C**), female rats **(D),** and female pigs **(E)** Each cell represents the median percent change in the proportion of cells assigned to a given shape mode within a brain region, calculated as (mature − term) / term × 100. Color intensity reflects the magnitude and direction of change, with red indicating an increase and blue indicating a decrease in the proportion of cells in a given shape mode at maturity.

While these trends were the same between female and male rats, we saw sex-based differences in the mouse. The trends for the male mouse aligned with those from the rat and pig, whereas in the female mouse the statistically significant changes moved in the opposite direction. RNA-seq data of microglia from male and female mice showed that genes related to apoptosis and inflammation were higher in female mice[188]. The same study found that there were no statistically significant differences between male and female rats at 3 weeks in the hippocampus, cortex, amygdala, striatum, and cerebellum, but that at 13 weeks the soma a size of microglia and microglia were larger in the cortex, hippocampus, and amygdala.

Our findings highlight a sex-based effect of microglia during neurodevelopment that is not seen comparing rats of different sex. Another potential factor is the timing of microglia development. Single-cell analysis of microglia during development showed region-specific differences in microglial populations[189]. It is possible that the windows of development between male and female mice differ, leading to the differences in morphology we saw. In fact, Hanamsagar et al showed that in the mouse hippocampus, microglial development plateaued earlier compared in male mice[190].

Our results show that regional morphology can vary with maturation in a species dependent manner, highlighting the necessity of regional assessment and comparison. In a previously reported study, the homeostatic role of microglia and impact on morphology was different across species but independent of phylogenetic tree[191]. The same study noted cell size

differences in branching patterns were different across species and impacted by maturation and presence of pathology. In our study, the changes identified by individual cell morphology geometric feature analysis and shape modes highlight the regional heterogeneity of species. The mouse displayed more regional heterogeneity during maturation than the rat. Regional heterogeneity in the mouse has been noticed by several researchers; one review even discusses the independence of microglial morphology heterogeneity from transcriptome heterogeneity during development suggesting other factors such brain environment impacts dominate morphological changes[192].

Our results also demonstrated that not all regions show the hallmark changes of shifting from an ameboid to ramified morphology across neurodevelopment. One reason could be differences between white and gray matter during neurodevelopment. Activated microglia that have an ameboid morphology accumulate near the ventricles and in white matter regions, shown in rodents[193,194] and humans[195]. Bulk RNA sequencing analysis in white and gray matter regions of mice at P7 and P10 microglia showed that cerebellum and corpus callosum microglia were clustered separately from cortex microglia[196], but at P42 became similar across all regions. In the same study, corpus callosum and cerebellum microglia had ameboid, activated shape but in cortex they were ramified.

4.3.4 White and Gray matter differences across species at sexual maturity

A critical aspect of researching microglia is understanding the similarities between human physiology and that of animal models at similar ages. Using the images collected from humans aged 21-38 years, we investigated differences in microglia morphology at sexual maturity in the human, rat, mouse, and pig to identify species and sex specific trends in cortex and corpus callosum. We split by sex to understand the distribution of microglia in white and gray matter.

We used linear mixed models and random forest models to compare the difference in 6 morphological features – solidity, circularity, aspect ratio, area, major axis length, and minor axis length – between the two regions. The set of 6 morphological features were chosen to reduce interdependence between features.

When comparing the effect sizes of the differences of parameters between the two regions, the male data showed differences between the rodent data and the human data **(Figure 4.8).** In both the rat and mouse, aspect ratio and major axis length were lower in the cortex compared to the corpus callosum while in the human data the major axis length and area were higher in the cortex and aspect ratio was not different between the two regions. Solidity and circularity were both higher in the human corpus callosum while being higher in the mouse cortex. Interestingly, minor axis length was the only morphological parameter that was statistically significant in one of the rodent models and the human data where the direction of the effect size was the same. In the female data, aspect ratio was lower in the cortex for the rat, mouse and pig. Differences in sex also appeared to be species specific. In both the mouse and rat, both sexes had a lower aspect ratio in the cortex compared to the corpus callosum. In the human data, the morphological differences between the two regions were much more significant in the male human compared to the female human.

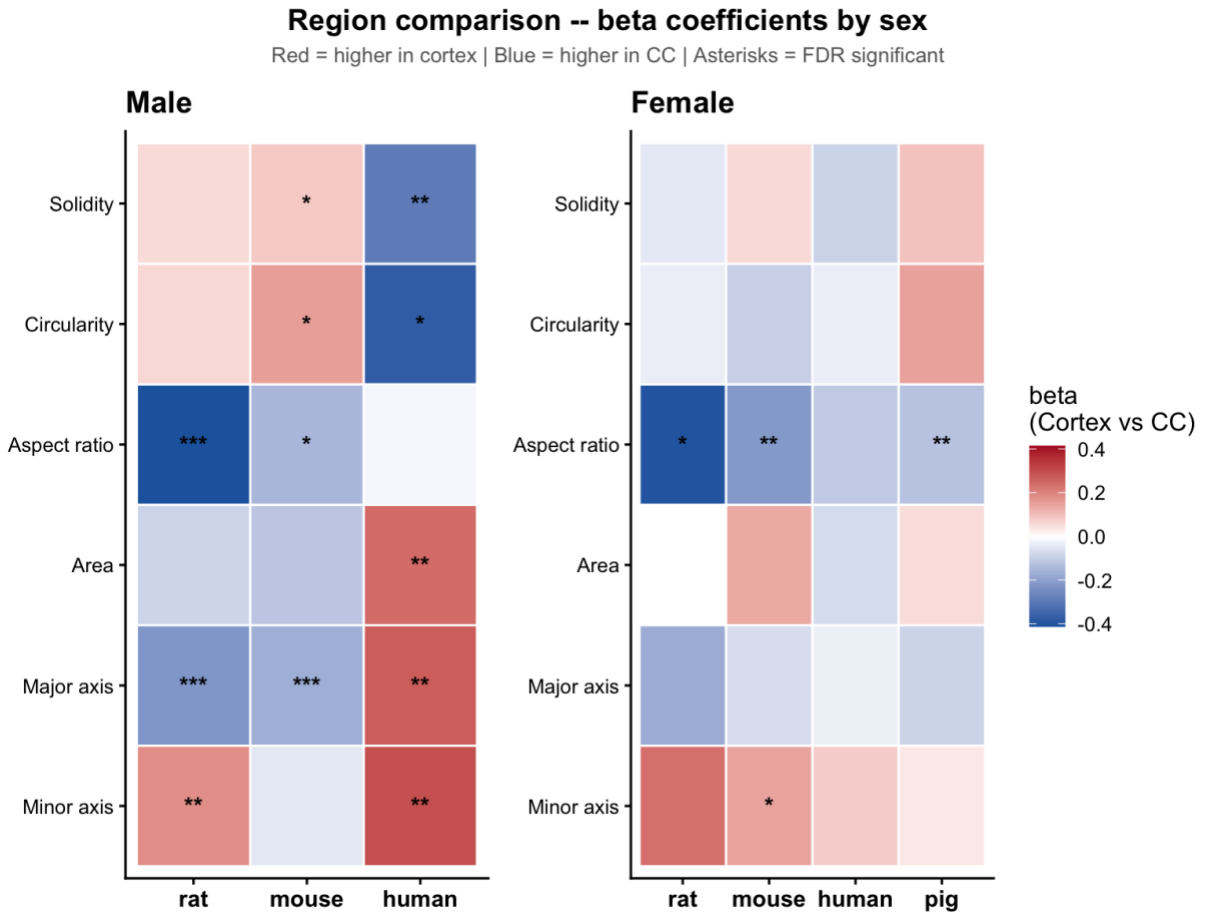

Figure 4.8 Statistical significance of beta coefficients between cortex and corpus callosum

Heatmaps of beta coefficients from region comparison models (cortex vs. corpus callosum) for microglia morphological features in males (left) and females (right) across species. Positive beta coefficients (red) indicate higher values in the cortex, while negative beta coefficients (blue) indicate higher values in the corpus callosum. Asterisks denote FDR-corrected significance (* $p < 0.05$, ** $p < 0.01$, *** $p < 0.001$).

VAMPIRE SM analysis also demonstrated species specific differences in white and gray matter microglia populations. The corpus callosum in the rat in both male and female animals had the highest proportion of microglia from the SM4 cluster, at 51% and 46.4% (**Figure 4.9**). In the female mouse and pig SM4 was also at a higher proportion in the corpus callosum compared to the cortex but was nearly identical in the female human. Across all female animals the distribution of shape modes was most similar between the cortex and corpus callosum in the human. In the male mouse SM4 has also higher in the corpus callosum corresponding to the

importance of aspect ratio and major axis length, but the difference in proportions was lower compared to the rat. The similarity of the SM distributions between the cortex and corpus callosum in the male human suggests that the microglia between the regions are similar in morphological type.

(A)

Female

Species	Region	SM 1	SM 2	SM 3	SM 4	Var
Mice	Cortex	28.4	26.6	22.8	22.2	8.9
	Corpus Callosum	27.4	20.2	18.1	34.3	54.3
Rat	Cortex	28.0	19.2	26.2	26.6	15.5
	Corpus Callosum	19.9	17.1	16.6	46.4	205.6
Human	Cortex	17.2	17.8	25.4	39.6	108.7
	Corpus Callosum	19.8	16.7	22.6	40.9	118.2
Pig	Cortex	17.8	27.0	27.6	27.6	23.1
	Corpus Callosum	23.0	15.5	25.0	36.5	75.5

(B)

Male

Species	Region	SM 1	SM 2	SM 3	SM 4	Var
Mice	Cortex	30.0	21.3	22.9	25.8	14.6
	Corpus Callosum	24.0	22.9	22.0	31.0	16.8
Rat	Cortex	31.1	21.6	22.4	24.9	18.5
	Corpus Callosum	17.4	19.0	12.6	51.0	307.8
Human	Cortex	27.6	25.0	24.1	23.3	3.5
	Corpus Callosum	26.7	27.2	19.1	27.0	15.5

Figure 4.9 Shape mode distributions between cortex and corpus callosum across species and sex at sexual maturity

VAMPIRE shape mode distributions for the cortex and corpus callosum in the mouse, rat, human, and pig at human sexual maturity equivalent. Red values indicate that the proportion of that shape mode was higher than 25%, and blue values indicate that the proportion was less than 25%.

Our results demonstrate that species play a critical role in morphological differences between white and gray matter regions. In both rodent models and the pig, cells in the corpus callosum had higher aspect ratios compared to the cortex, which suggests distinct populations of microglia between the two regions. Microglia specific to white matter have been shown in the mouse corpus callosum[197] that play a critical role in myelin clearance, and were not present in the cortex. Similar trends have been found in the rodent brain, and there have also been differences shown in the viscoelastic properties of white and gray matter microglia[194]. Microglia branching likely also plays a role in differentiation of microglia between white and gray matter, as white matter regions have been shown exhibit complex branching patterns, whereas gray matter microglia tend to be less ramified[198].

Our data also suggest that male human microglia differ between white and gray matter regions in a manner distinct from rodent data. The difference between white and gray matter microglia aligns with transcriptomic analysis that has shown region-specific gene expression profiles[199]. While sex differences between microglia have been shown in humans[200], it is unclear whether the differences between male and female microglia in the human we show are due to true biological differences or a limited number of human samples. The differences between rodent and human microglia across morphological parameters and shape mode may partly be driven by differences in microglia density. In humans, microglia density is higher in white matter relative to gray matter[201], which is the opposite trend seen in rodents[198]. A limitation with this study is that separating into distinct clusters does not capture the continuous nature of microglia morphology. Using a rank-based method, such as fuzzy K-means[202], could potentially improve our ability to capture changes in morphological distribution and has recently been used for microglia morphology analysis[186]. A fuzzy clustering methodology would allow for microglia to

be within multiple clusters at once, which could lead to a better understanding of microglia transitioning between states, and a better separation between microglia which are in distinct clusters compared to on the border of multiple clusters.

4.4 Conclusion

In this study, we provide one of the first investigations into microglia morphology heterogeneity across species. Cross species assessments are critical for translational research to choose the most representative animal models of human microglial diversity as well as understand potential biases or important differences when developing treatments with the goal of translating to human studies. Our results demonstrate that the shift from an ameboid to ramified morphology during neurodevelopment is consistent across species, but that species is a key factor for the regions where the changes. We then look at differences between white and gray matter microglia morphologies, showing that while both rodents and humans have distinct morphologies in white and gray regions, the differences are not consistent between rodents and humans. Overall, our work demonstrates an important step in mapping the heterogeneity of microglia across age, region, and species.

CHAPTER 5 RHEOLOGICAL MIMICS USING A HYDROGEL-BASED BRAIN MICROENIVORNMENT TO INVESTIGATE MICROGLIA-ECM INTERACTIONS

This chapter is being prepared for publication, with contributions from Nels Schimek, Ryan Brady, Sydney Floryanzia, Cole DeForest, and Elizabeth Nance

5.1 INTRODUCTION

The Nance Lab has been a driver of research towards understanding and treating neonatal hypoxic ischemia, primarily through the use of organotypic whole hemisphere brain slices. Quantitative assessment of changes to the tissue microenvironment has primarily used multiple particle tracking (Chapter 3) and microglia morphology analysis (Chapter 4). Previous work from the lab has also correlated shifts in microglia morphology and changes to microrheology as measured by changes in nanoparticle diffusion in non-treated control (NC) and 0.5 h OGD-exposed slices[97]. Specifically, the effective diffusion coefficient as well as the percentage of superdiffusive and normally diffusive nanoparticles were higher in slices that had been exposed to OGD (**Figure 5.1A-B**) compared to NC slices, which corresponded to higher microglia circularity in 0.5h OGD exposed slices compared to NC slices (**Figure 5.1C**). However, these datasets were collected in separate brain slices and are only correlative at best, limiting the ability to evaluate how microglia directly modulate their local environment.

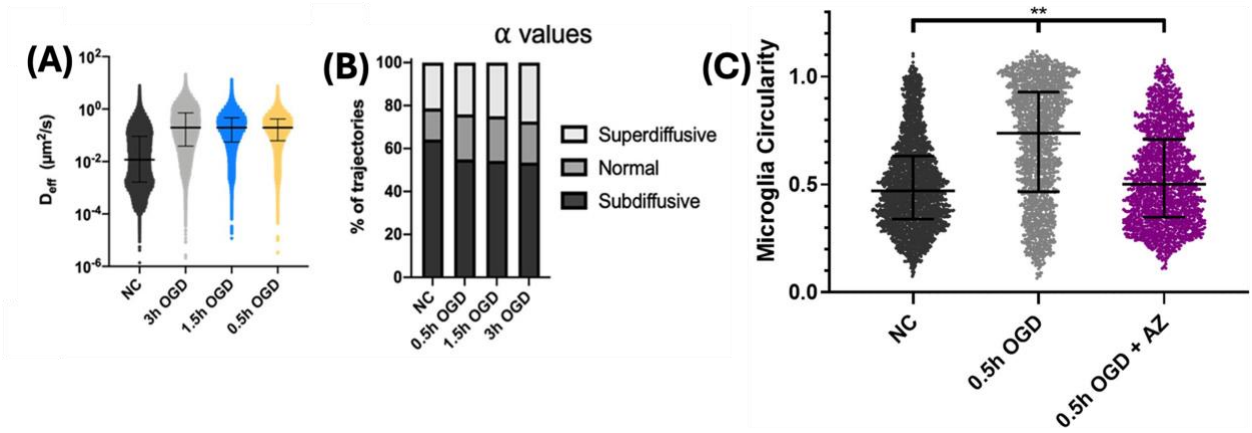

Figure 5.1 Measures of diffusion and microglia circularity in healthy and OGD exposed OWH brain slices, adapted from Joseph et al.

(A) Diffusion coefficient, calculated at 0.33s from nanoparticle trajectories was higher in all OGD timepoints compared to the non-treated control. **(B)** Alpha value was used to estimate the distribution of diffusion modes, based on the percentage of trajectories. Alpha values greater than 1.1 were considered superdiffusive, below 0.9 were considered subdiffusive, and between 0.9 and 1.1 were considered normal or Brownian motion. The percentage of superdiffusive and normal trajectories was lowest in the non-treated control group. **(C)** Violin plots of microglia circularity, with each point representing a cell, showed that the median microglia circularity increased with OGD treatment as well as a change in the shape of the distribution.

The need for methods to probe ECM-microglia interactions is highlighted by the current known roles that microglia have in modulating the ECM. Models of microglia depletion have shown increased perineuronal networks (PNNs), a specialized ECM structure, in the mouse visual cortex[49] and striatal volume loss and prevention of PNN degradation in Huntington's disease in mice[203]. Microglial activation has also resulted in PNN loss in Alzheimer's brain models in human and mice[204], altered PNN assembly in the aged brains of rhesus macaques[205], and mediated the degradation of PNNs after peripheral nerve injury[50]. Additionally, microglia can engulf the ECM to promote synaptic plasticity in response to neuronal signaling[206]. Despite these findings, two recent review papers have highlighted the need for more insight into the interactions between microglia and the ECM[207,208], with the most recent review article coining

the term “the microglial-ECM interactome” and specifying the need for hydrogel-based ECM systems that can complement *in vivo* studies[207].

The knowledge gap of the ECM-interactome motivated the development of a platform where MPT and microglia morphology analysis could be applied in the exact same space to better capture changes to the microenvironment. Biomaterials have become exceedingly popular as tools to understand the ECM and cell interactions[209]. Hydrogels with 3D cell culture have been shown to mimic the ECM and enable the study of soft tissue mechanics, cell adhesion, and protein sequestration[210] and can be engineered to have specific biophysical properties that mimic a cell’s extracellular environment[100]. Hyaluronic acid hydrogels have been used to assess cell-material interactions and secreted matrix components[211] and hydrogels have been used to asses microglial morphology[106], including the immortalized BV2 microglial cell line in 3D collagen gels in LPS injury condition[212].

In this chapter, we demonstrate the use of primary glial-seeded gels for spatial and temporally aligned MPT and microglia morphology. First, we measure the rheological properties of OWH brain tissue to compare the rheological properties of the gels. Next, we demonstrate that microglia can be seeded and stay alive in these gels. We then show that in non-cell seeded gels, MPT measures changes in diffusion that are modulated by changing collagen concentrations. Due to the differences in image acquisition required to capture the time scale of diffusion via MPT and the microglia morphology shifts via confocal, we also verify that MPT and cell morphology can be captured in the same area. Using gels seeded with either fibroblasts or microglia, we demonstrate that diffusion is higher in gels seeded with fibroblasts compared to microglia. Lastly, we measure changes to nanoparticle diffusion as a function of distance to a cell to determine the utility of spatial analysis in the platform.

5.2 MATERIALS AND METHODS

5.2.1 OWH rheology

Organotypic whole hemisphere (OWH) brain slices were isolated from postnatal day 10 (P10) Sprague-Dawley rats and sliced to 300μm as we have previously described[96]. Slices were cultured in normal slice culture conditions and measured at 1-hour post-slicing (acute), 1DIV, 3DIV, and 6DIV.

Brain slice storage moduli (G') was analyzed on a Physica MCR-301 rheometer (Anton Paar; Graz, AT) at 25 °C with 8 mm parallel plate geometry (0.5 mm gap, 1 Hz, 1% strain). Slices were gently removed from their culture membranes intact, then were floated in a PBS droplet on the rheometer plate, and PBS was slowly removed to allow the slice to adhere onto rheometer for analysis. The frequency and strain were determined to fall within the viscoelastic range via frequency and amplitude sweeps.

5.2.2 Glial cell isolation

Primary microglia were obtained within mixed glial cultures isolated from P5-P7 rats. After extraction, surface vessels were removed from the brain, and successive mechanical dissociation was performed. The whole brain tissue solution was then passed through a 70μm nylon cell strainer. The solution was washed then plated on Poly-D-Lysine (PDL) or Poly-L-Lysine (PLL) flasks. Cells were kept in an incubator at 37°C and 5% CO2 with media changes (DMEM-F12, 10% FBS, and 1% penicillin/streptomycin) performed every 2-3 days throughout the duration of culture as previously described[213]. In this study, primary glia were used only at passage number 1-3.

5.2.3 Collagen gel formation and cell seeding

3D collagen domes were formed using rat tail type 1 collagen (Corning, High Concentration, 9.6 mg mL^{-1}). Final collagen formulations were made by mixing 0.5 M NaOH, 10 mM HEPES, and PBS on ice. Solution was pipetted onto rheometer or glass well plate for gel formation. To initiate polymerization gels were left at 25 °C for 10 min and then transferred to 37 °C for 30 min. Gels were then submerged in PBS or cell culture media. For cellularized gels, fibroblasts or glial cells were added to collagen pre-polymer solution at a concentration of $5*10^6$ cells mL^{-1}. Cellularized gels were cultured in DMEM F12 with half media exchanges daily for 6 days.

5.2.4 Immunofluorescent staining and nanoparticle application

On day 6 after cell seeding in gels, gels were blocked with 2% FBS in Hank's Balanced Salt Solution (HBSS) for 2 hours at 37 °C. Subsequently, glial cells were labeled with 1:200 FITC-CD11b/c (Biolegend 201805) and 1:1000 NucBlue (2% FBS, HBSS, 37 °C). Gels were washed with supplemented Fluorobright DMEM (10% FBS, 1x P/S) for 2 hours. Nanoparticles were applied to gels in supplemented Fluorobright DMEM 12 hours prior to imaging (2% w/w).

5.2.5 Nanoparticle formation

100 nm fluorescent-labeled polystyrene (PS) carboxylate particle beads modified with polyethylene glycol (PEG) were made according to previous lab protocols[141].

5.2.6 Spatially aligned confocal microscopy imaging and multiple particle tracking

All imaging was done on a Nikon A1R confocal microscope. Brightfield was used to ensure that we were within the gel when imaging. A CMOS camera was used for MPT using a TRITC laser. Collected videos were 10 seconds long at 67 frames per second at 60x magnification. Immediately after video collection, the confocal was used to take a Z-stack centered at the plane of the video with five 5-micron steps on either side for a total of 11 stacks. We collected data from 2 fibroblast-seeded gels and 3 microglia seeded gels. We collected 3 videos at different locations for each gel.

5.2.7 Data processing

MPT videos were processed using the FIJI plugin Trackmate to find nanoparticle trajectories. Diff_classifier was used to calculate mean squared displacement, diffusion coefficient, and geometric features of the trajectories. The image segmentation modules of TURMorIC were used to create binary masks of the microglia and fibroblasts in each gel. Using the trajectory data from diff_classifier and the masks from TURMorIC, SAFFRON was used to align the trajectories with the segmented cells from the same location and calculate the distances between the centroid of each trajectory and the nearest cell boundary.

5.3 Results and Discussion

5.3.1 Rheological properties of OWH brain slice

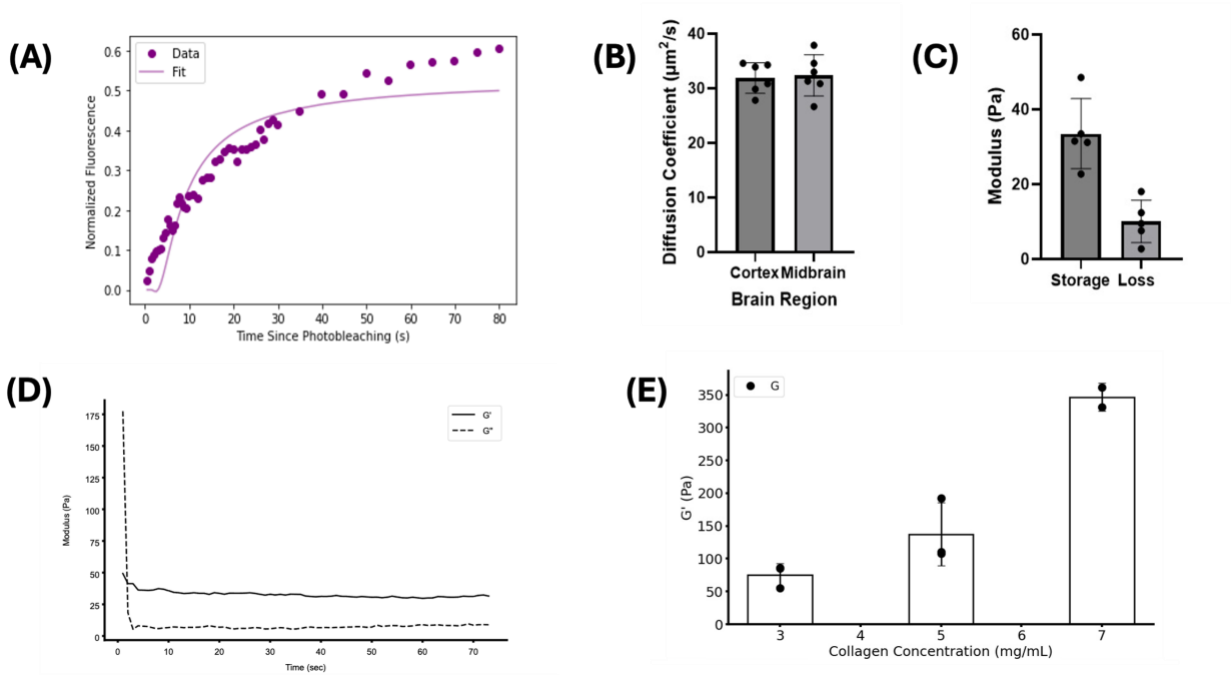

Figure 5.2 Rheological properties of OWH brain slices and collagen gels

Assessment of the rheological properties of organotypic whole hemisphere brain slices and collagen cells. (A) FRAP data points and model fit for OWH brain slice. (B) Diffusion coefficient calculated from rheometer for cortex and midbrain OWH slices. (C) Storage modulus and loss modulus for OWH brain slices. (D) Storage modulus and loss modulus in OWH brain slice measured over 75 seconds. (E) Storage modulus for collagen gels at 3mg/ml, 5mg/ml, and 7 mg/ml

To ensure that the hydrogel platform would be a rheological mimic to brain slices, we determined rheological properties for OWH brain slices and collagen gels at varying collagen concentrations. The FRAP curve showed an increase in normalized fluorescence over the course of the experiment, increasing the most up to 20 seconds (**Figure 5.2A**). The model fit well to the data up to 30 seconds, then plateaued while the true data continued to increase. Based on diffusion coefficient, we did not see a difference in stiffness (**Figure 5.2B**). We determined the mean storage modulus of the brain slice to be near 30, and the loss modulus to be near 10 (**Figure 5.2C**). Storage and modulus were consistent over the course of 75 seconds of continuous measurement (**Figure 5.2D**). To determine the best choice of collagen concentration, we also

measured the storage modulus at of collagen gels at 3, 5, and 7mg/ml. The collagen concentration with the storage modulus closest to that of OWH brain slices was 3mg/ml (**Figure 5.2E)** and was therefore chosen as the primary concentration for the study. The rheological values demonstrate that collagen gels can be designed to have a storage modulus near that of OWH brain slices, and that we are able to tune the rheological properties if needed by changing the concentration and providing a baseline for future tuning of rheological mimics. One limitation of this platform is that collagen is minimally expressed in the brain ECM compared to the ECM of other organs[214,215]. Based on our results bulk rheology within a range relevant to OWH brain slices is achievable, although it may more accurately represent the basement membrane compared to the interstitial ECM[214]. Our rheological data of OWH slices agrees with previous calculations done by Li et al[216]. In their study, they measured the ratio of G' and G" and showed a range of 0.3 to 0.7.

5.3.2 NucBlue and CD11b stains in gels show successful glial culture

After seeding collagen gels with the glial mixture and staining as described in section 5.2, we imaged gels with no nanoparticles to confirm the cells were alive after 72 hours (**Figure 5.3A)**. The NucBlue stain demonstrated well-distributed nuclei across the region of interest (**Figure 5.3A, left)**. The CD11b stain showed clear cell boundaries and intact membranes (**Figure 5.3A, center)**. The overlay of the two stains confirmed that we had specific staining of microglia as they aligned with the NucBlue stain (**Figure 5.3A, right)**. The segmentation and trajectory overlay of fibroblast gels (**Figure 5.3B**) and microglia gels (**Figure 5.3C**) demonstrate clean segmentation of individual cells and successful co-registration of cell boundaries and

nanoparticle trajectories. Cellular and trajectory density appeared comparable by visual inspection between fibroblast and microglia-seeded gels.

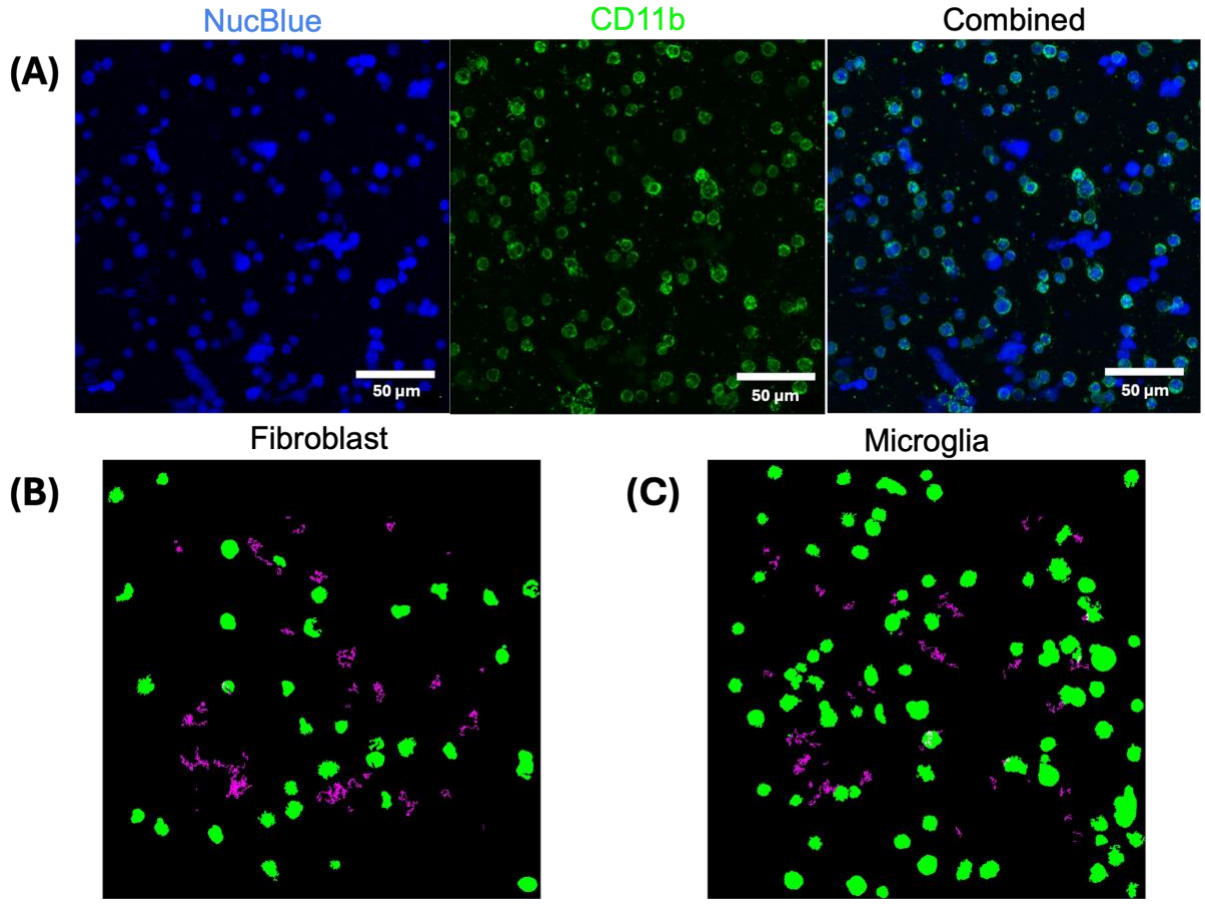

Figure 5.3 Representative confocal microscopy images and trajectory overlay
Representative images of glial mixture gels. **(A)**: NucBlue nuclear stain (left), CD11b microglia marker (center), and merged channel overlay (right). Scale bars = 50 µm. **(B)** Representative image of segmented fibroblast mask (green) overlaid with nanoparticle trajectory data (purple). **(C)** Representative image of segmented microglia mask (green) overlaid with nanoparticle trajectory data (purple).

5.3.3 Mean Squared Displacement and Diffusion differ between fibroblast and microglia seeded gels

In order for the platform to be useful, it needs to detect differences in mean squared displacement and diffusion in collagen that has not been disturbed compared to disturbed networks. For this

analysis we seeded cells with microglia and others with fibroblasts that are known to break down the matrix. Mean squared displacement and diffusion coefficient values were higher in the fibroblast gels compared to glial-seeded gels, indicating that particles were moving faster and covering greater distances in the fibroblast gels. The difference in effective the diffusion coefficient (Deff1) and the coefficient of the anomalous diffusion equation between fibroblast and microglia seeded gels is consistent with the degradation of collagen by fibroblast mediated release of MMPs[217]. When comparing other geometric features between gels of the two cell-types, no other features had distinctly different median values. These results suggest that with the current experimental, the changes we can detect are at the scale of bulk rheology rather than individual trajectories. We could address this by determining the effect of nanoparticle size or collagen concentration on geometric features. Studies of nanoparticle diffusion in collagen gels have demonstrated that nanoparticle MSD and diffusion increase as pore size increases and as collagen gel density decreases[218]. Overall, our results demonstrate that the collagen gel platform combined with MPT can be used to detect changes to extracellular dynamics consistent with matrix remodeling, making it a useful platform to study cellular-extracellular interaction in injury conditions where matrix remodeling is known to occur.

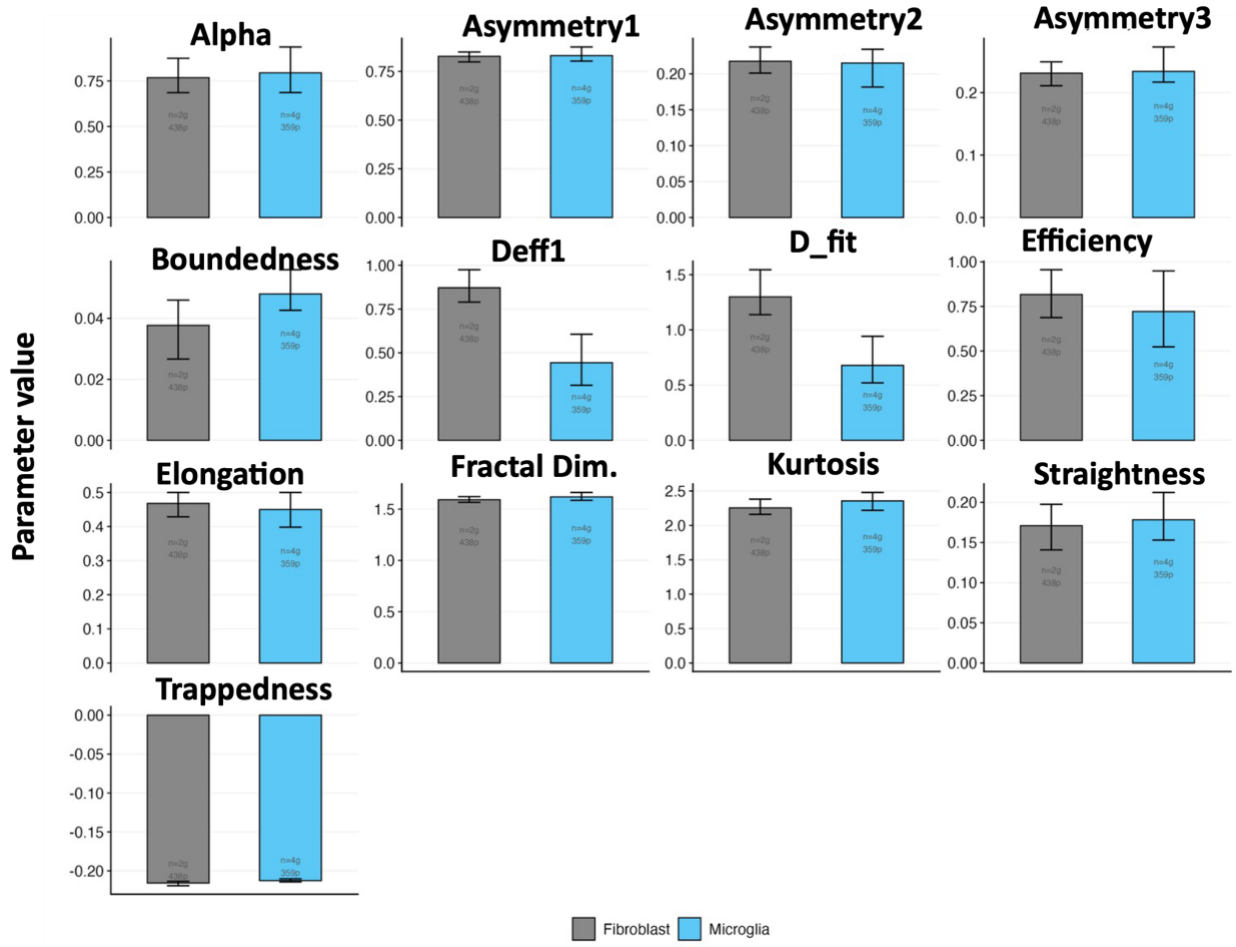

Figure 5.4 Geometric properties of nanoparticle diffusion between fibroblast and microglia seeded gels.

Geometric properties of nanoparticle diffusion between fibroblast and microglia seeded gels. 13 geometric features – Deff1 (mean diffusion coefficient at 0.33 seconds), alpha, D_fit (fitted diffusion coefficient), kurtosis, asymmetry1, asymmetry2, asymmetry3, elongation, boundedness, fractal dimension, trappedness, efficiency, straightness – were calculated for all trajectories from each multiple particle tracking video. Medians and 95% confidence intervals were calculated by bootstrapping for 10,000 iterations.

5.3.4 Spatial analysis of microglia and nanoparticle diffusion

A benefit of the cell-seeded collagen gel is that we can assess spatial relationships between cells and nanoparticle diffusion. We additionally fit a linear model to each feature to find the slope.

We hypothesized that features of diffusion such as the effective diffusion coefficient and alpha,

as well as geometric features such as straightness or boundedness, would change as a function of distance from the nearest cell. Specifically, we hypothesized that the effective diffusion coefficient, alpha, and straightness would be higher closer to fibroblasts and microglia because of matrix breakdown due to the release of matrix degrading enzymes, while boundedness would be higher farther away from cells, as there would be more complex structures for nanoparticles to become confined in. Across those four features and all other features in **Figure 5.4**, we did not detect any effect of distance on feature value. Deff1 showed no relationship with distance from the cell boundary, with an R^2 value 0.0002 in fibroblast gels and 0.000 in microglia gels (**Figure 5.5A**). Similarly, alpha had an R^2 value of 0.0001 in fibroblast gels and 0.0049 in microglia gels (**Figure 5.5B**). Straightness had an R^2 value of 0.0026 in fibroblast gels and 0.0133 in microglia gels (**Figure 5.5C**), while boundedness had R^2 values of 0.0097 in fibroblast gels and 0.0042 in microglia gels. Overall, the low values of R^2 across all features suggests that distance from the cell membrane is not predictive of nanoparticle behavior in our collagen gel platform.

A few reasons could explain that lack of any effect. Looking at the alpha values in the fibroblast and microglia gels, the fact that the fitted line is close to 1 across the range of distance, and is evenly distributed above and below, highlighting that the diffusion modes of nanoparticle trajectories are evenly distributed across the gel. If there is no effect of distance from the cell on any feature of diffusion, it could be due to the fact that at the time of data collection, the cells are not remodeling the matrix, and it already exists in a state that is consistent across the gel. This effect has been shown in relation to fibroblasts. QCRT-PCR analysis of fibroblast-mediated lattice contraction in collagen gels showed high levels of MMPs secreted from fibroblasts on day 1, which progressively decreased through day 7[219]. One potential cause for the lack of differences in microglia seeded gels specifically could be the interaction with collagen.

Researchers showed that microglia seeded in collagen only hydrogels displayed reduced motility, activation, and existed primarily in a rounded morphology[106]. Notably, when the authors used hydrogels that contained collagen-like peptides (CLPs) conjugated to a polyethylene glycol (PEG) core and saw increased activation and more complex morphologies. Alterations to microglia function in our collagen could be playing a role in why there are no trends related to distance in the microglia cells. Future work should focus on investigating whether changes to the system can enable detection of distance to cell relationships of features. This could be done through changing the composition of our hydrogel platform, collecting data at different time points during culturing, or immediately after perturbation that is known to degrade the ECM or lead to matrix remodeling.

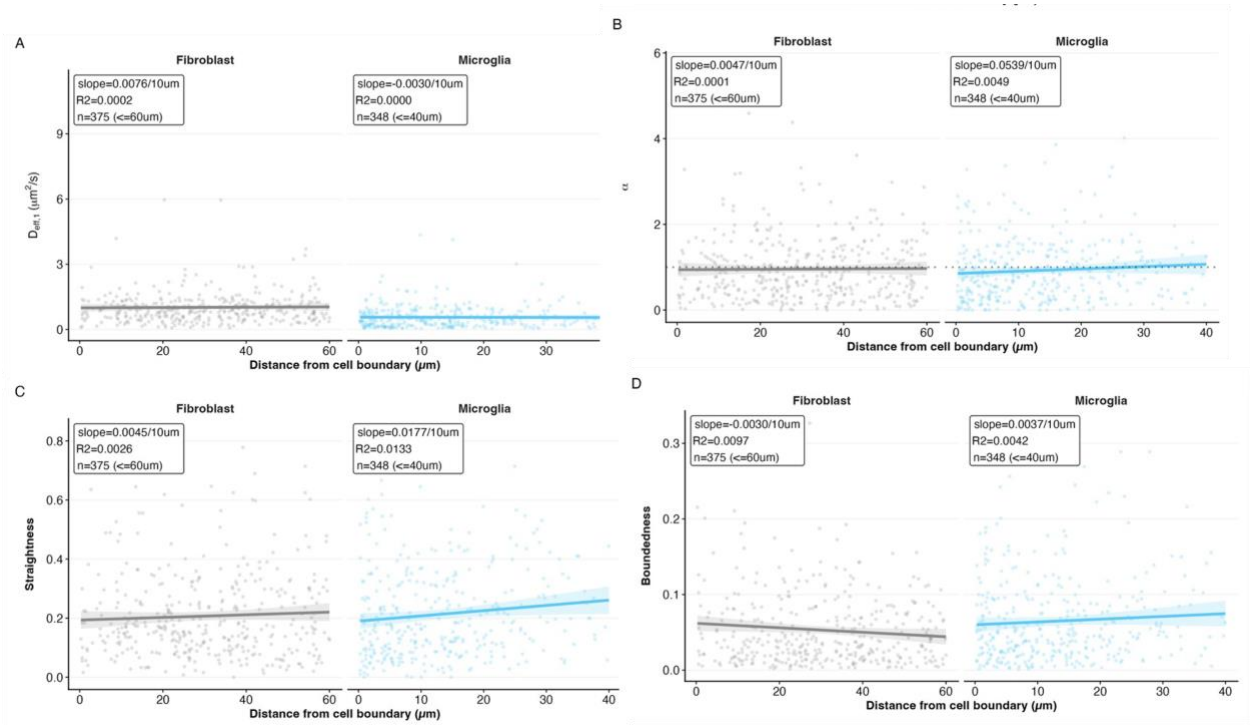

Figure 5.5 Linear fit of geometric features and distance from cell boundary

Slope and R^2 of linear models for **(A)** Deff1, **(B)** alpha, **(C)** straightness, and **(D)** boundedness. Models were fitted for distance data between 0 and 60 microns for fibroblast gel data which accounted for 86% of trajectories, and between 0 and 40 microns for microglia gel data which

accounted for 97% of trajectories. The cutoffs were chosen based on the distance when trajectory counts began to plateau.

5.4 Conclusion

Our results show that the collagen-based hydrogel is a rheological mimic of OWH brain slices when at a concentration of 3mg/ml, demonstrated by the storage modulus values comparable to that of OWH brain slices. The platform can be combined with multiple particle tracking and confocal microscopy to detect statistically significant differences in nanoparticle diffusion between fibroblast and microglia seeded gels that are aligned with fibroblast mediated matrix degradation. We did not detect any spatial relationship between statistical and geometric features of MPT and the distance of a trajectory to a cell boundary. We successfully demonstrated the feasibility of simultaneous and spatially aligned MPT and microglia morphology analysis, and future work should leverage this methodology to examine spatial relationships at different time points, with methods of ECM and cellular perturbation, and in other brain-mimetic hydrogel systems.

CHAPTER 6 CONCLUSION AND FUTURE WORK

6.1 SUMMARY AND CONCLUSION

The goals of this dissertation are to improve the understanding of the brain microenvironment by developing and applying data science methodologies to multiple modalities of data that can be collected in OWH brain slices, as well as developing a brain microenvironment mimic that can be used to collect multimodal datasets. With this intent, machine learning and statistical analysis methods were used on multiple particle tracking data and microglia morphology data collected in OWH brain slices, and both modalities of data were simultaneously collected in gel-seeded hydrogels to enable spatial analysis and an unmet need of directly studying microglia-ECM interactions.

In Chapter 3, we demonstrate that explainable machine learning can reliably be applied to multiple particle data collected in OWH brain slices to make accurate predictions of different biological variables, specifically brain age, region, and treatment condition. We additionally show that explainable machine learning can detect changes to geometric features of diffusion that are distinct based on brain region and treatment severity. In Chapter 4, we show the first analysis of microglia morphology across species and demonstrate statistical and machine learning tools that can be used to key similarities and differences in microglia distribution based on region and species. This work highlights the importance of using animal models that have representative microglia populations when doing translational research. In Chapter 5, we present the first approach of simultaneous and spatially aligned MPT and microglia analysis, demonstrating a platform and method of data collection that can be used to investigate complex microglia-ECM interactions.

6.2 RECOMMENDED FUTURE WORK

Characterization of the ECM with MPT done in OWH brain slices models of pathology informs the microstructural changes that occur within brain tissue after injury, which can be used to determine the key changes that therapeutics should target, as well as giving insight into the microenvironment that nanotherapeutics need to navigate in order to reach their target. In the Nance lab, we have demonstrated these changes in OWH brain slice models of OGD and rotenone[220,221]. While we have assessed changes in microglia morphology due to injury and also in response to treatment[114,220], we have yet to run MPT in OWH brain slices exposed to OGD or rotenone that were then treated with neuroprotective drugs. In Joseph et al, nanoparticle uptake by microglia was assessed within OGD brain slices with and without Azithromycin treatment, but nanoparticle diffusion was not analyzed in the Azithromycin treatment. To address this gap, we could first collect MPT data in OWH brain slices exposed to OGD and then treated with nanotherapeutics. Our studies on neuroprotection have demonstrated less cell death and similar morphology distributions between healthy and treated slice[220,222,111]. Collecting MPT data in injured slices treated with drugs we know are neuroprotective for brain cells would inform whether the neuroprotection from ECM degradation. Collecting MPT at multiple time points after injury and treatment could inform temporal dynamics of ECM degradation and remodeling.

Brains with high gyrification are more representative of human brain tissue due to the complex folds and white-gray matter ratios. For example, the ferret brain slices have been exposed to OGD to study the microglial response to injury and treatment specifically because the white matter content is more similar to humans[114]. While we have studied changes to diffusion in OGD conditions, these studies have been done exclusively in rat models[220], which have a lower

ratio of white matter to gray matter compared to humans and ferrets. Future work could look at multiple particle tracking in OWH brain slices from gyrified tissue, such as ferret or pig. Current imaging modalities are limited in their ability to capture ECM changes in white matter because white matter regions are not superficial. By using OWH brain slices from the ferret, we could specifically investigate analysis of the ECM in white matter and determine differences in the response to aging and injury compared to previously assessed animal models. Because we have only collected MPT in rat models, it is unclear whether the changes to diffusion due to age, region, and treatment represent responses that are conserved across species or are species-specific. Characterizing baseline diffusion in multiple species across neurodevelopment, region, and sex would give insight into the heterogeneity of the ECM across species with respect to neurodevelopment, region, and sex. Identifying ECM properties that are either conserved across species or specific to white matter could identify potential therapeutic targets as well as informing whether the microenvironment that nanoparticle-based therapeutics diffuse and distribute through will accurately represent the environment of human brain tissue.

We have previously used RT-qPCR data to investigate the gene expression profile of microglia in response to OGD in brain slices. Studies done in hydrogels have demonstrated the feasibility of analyzing gene expression of cells in these gels. To better characterize our hydrogel system, we should collect RT-qPCR data in hydrogels to understand how gene expression of microglia changes with different molecular weights of collagen, different concentrations of collagen, and then compare the gene response to gels that undergo OGD exposure. Varying the molecular weights and concentrations of collagen gels while collecting RT-qPCR data would allow us to characterize gene expression signatures directly related to changes in rheological properties of the microenvironment, and in OGD expose gels characterize the specific gene

upregulated during injury. By comparing the gene expression data in these conditions to the MPT data collected in the same gels, we would be able to directly relate changes to gene expression to alterations in microstructure and diffusion.

The spatial and temporally aligned microglia imaging and MPT could be done next in OWH brain slices. A first study should determine whether there is a relationship between distance to microglia in a more complex microenvironment. Collecting the aligned data in OWH brain slices would also enable deeper investigation of whether microglia morphology is a factor in modulating local diffusivity, as the microglia in OWH brain slices would display more complex morphologies than the microglia seeded in the collagen gels. It would then also enable us to collect aligned data across different regions and ages, allowing us to investigate the heterogeneity of cellular-extracellular interactions as a function of region and neurodevelopment.

Our collagen-based rheological mimics could be used to study cellular interactions of delivery vehicles used for drug or gene delivery. While our initial study only used one type of non-biodegradable, non-payload carrying nanoparticle probe, it would be feasible to use nanoparticles that are fluorescently labeled and designed for cellular uptake and drug delivery instead. Because of their role in modulating pathological environments discussed in Chapter 1, microglia are a promising therapeutic target. The cells in gel platform could be used for initial translational work investigating the diffusive properties of potential nanotherapeutics and simultaneously be used to monitor the interaction with microglia.

CHAPTER 7. SUMMARY OF CONTRIBUTIONS

Schimek, N., Beck, D., Wood, T., Mckenna, M., Nance, E*. High fidelity predictions of diffusion in the brain microenvironment. Biophys J. (2024), Vol 123, Issue 22, 3935 – 3950. doi: 10.1016/j.bpj.2024.10.005

Multiple-particle tracking (MPT) is a microscopy technique capable of simultaneously tracking hundreds to thousands of nanoparticles in a biological sample and has been used extensively to characterize biological microenvironments, including the brain extracellular space (ECS). Machine learning techniques have been applied to MPT data sets to predict the diffusion mode of nanoparticle trajectories as well as more complex biological variables, such as biological age. In this study, we develop a machine learning pipeline to predict and investigate changes to the brain ECS due to injury using supervised classification and feature importance calculations. We first validate the pipeline on three related but distinct MPT data sets from the living brain ECS—age differences, region differences, and enzymatic degradation of ECS structure. We predict three ages with 86% accuracy, three regions with 90% accuracy, and healthy versus enzyme-treated tissue with 69% accuracy. Since injury across groups is normally compared with traditional statistical approaches, we first used linear mixed effects models to compare features between healthy control conditions and injury induced by two different oxygen glucose deprivation exposure times. We then used machine learning to predict injury state using MPT features. We show that the pipeline predicts between the healthy control, 0.5 h OGD treatment, and 1.5 h OGD treatment with 59% accuracy in the cortex and 66% in the striatum, and identifies nonlinear relationships between trajectory features that were not evident from traditional linear models. Our work demonstrates that machine learning applied to MPT data is effective across multiple experimental conditions and can find unique biologically relevant features of nanoparticle diffusion.

McKenna M., Filteau J., Sluis K., Chungyoun M., Butler B., **Schimek N**., Nance E.* Organotypic whole hemisphere brain slice models to study the effects of donor age and oxygen-glucose-deprivation on the extracellular properties of cortical and striatal tissue; *Journal of Biological Engineering* (2022); 16:14; doi: 10.1186/s13036-022-00293-w

Background: The brain extracellular environment is involved in many critical processes associated with neurodevelopment, neural function, and repair following injury. Organization of the extracellular matrix and properties of the extracellular space vary throughout development and across different brain regions, motivating the need for platforms that provide access to multiple brain regions at different stages of development. We demonstrate the utility of organotypic whole hemisphere brain slices as a platform to probe regional and developmental changes in the brain extracellular environment. We also leverage whole hemisphere brain slices to characterize the impact of cerebral ischemia on different regions of brain tissue.

Results: Whole hemisphere brain slices taken from postnatal (P) day 10 and P17 rats retained viable, metabolically active cells through 14 days in vitro (DIV). Oxygen-glucose-deprivation (OGD), used to model a cerebral ischemic event in vivo, resulted in reduced slice metabolic activity and elevated cell death, regardless of slice age. Slices from P10 and P17 brains showed

an oligodendrocyte and microglia-driven proliferative response after OGD exposure, higher than the proliferative response seen in DIV-matched normal control slices. Multiple particle tracking in oxygen-glucose-deprived brain slices revealed that oxygen-glucose-deprivation impacts the extracellular environment of brain tissue differently depending on brain age and brain region. In most instances, the extracellular space was most difficult to navigate immediately following insult, then gradually provided less hindrance to extracellular nanoparticle diffusion as time progressed. However, changes in diffusion were not universal across all brain regions and ages.

Conclusions: We demonstrate whole hemisphere brain slices from P10 and P17 rats can be cultured up to two weeks in vitro. These brain slices provide a viable platform for studying both normal physiological processes and injury associated mechanisms with control over brain age and region. Ex vivo OGD impacted cortical and striatal brain tissue differently, aligning with preexisting data generated in in vivo models. These data motivate the need to account for both brain region and age when investigating mechanisms of injury and designing potential therapies for cerebral ischemia.

Olivia C. Brandon, Kylie A. Corry, Zheyu (Ruby) Jin, Kate F. DiNucci, Matthew J. Magoon, **Nels Schimek**, Daniel H. Moralejo, Sandra E. Juul, Patrick M. Boyle, Elizabeth A. Nance, Thomas R. Wood, Sarah E. Kolnik* Effect of Caffeine on Cell Death, Oxidative Stress, and Microglial Morphology in a Ferret Organotypic Brain Slice Model of Hypoxia-Ischemia *Submitted.*

Brain injury after hypoxia-ischemia (HI) is the leading cause of morbidity and mortality in term and near-term neonates worldwide. The ferret is a promising translational model to study HI due to its gyrified brain and white-to-gray matter ratio that more closely resembles humans compared to rodents. Caffeine shows neuroprotective potential after HI, but its mechanisms, including antioxidant and anti-inflammatory effects via adenosine A2A receptor antagonism, remain incompletely understood. We sought to evaluate caffeine's effect on neuronal cell death, cytotoxicity, and inflammatory and oxidative stress markers in a term-equivalent ferret organotypic brain slice model of HI. 300 μm slices were cultured for 72 hours, exposed to two hours of oxygen-glucose deprivation (OGD), and randomized to OGD alone, OGD with caffeine (20 or 50 mg/L), or OGD with caffeine and an A2AR agonist. Healthy slices served as controls. Outcomes included LDH release, pyknotic nuclei counts, and microglial morphology. Caffeine 50mg/L, alone or with the agonist, significantly reduced LDH compared to OGD but did not change regional pyknotic nuclei counts. Caffeine altered microglial morphology, increasing the proportion of microglia with features characteristic of control conditions. In summary, caffeine partially reversed global cell death after OGD and altered microglial morphology. Larger, higher-powered studies in diverse preclinical models are needed to further investigate caffeine's effects on neonatal HI.

Schimek, N., Filteau J., Butler, B., Nance, E.* (2022). Nano-Based Probes for the Brain Extracellular Environment. In: Nance, E. (eds) Engineering Biomaterials for Neural Applications. Springer, Cham. https://doi.org/10.1007/978-3-031-11409-0_2

The brain is our most complex organ and governs all physiological function, from cognition and emotion to movement and stress response. Much of the brain's function is determined by complex interactions of cells within the brain parenchyma, the functional unit of brain tissue critical for supporting and protecting cells. In fact, trauma or disease to the brain parenchyma can result in a loss of cognitive function and, in severe cases, death (Bonkhoff et al., Brain Commun 3(2):fcab110, 2021; Szarka et al., Int J Mol Sci 20(13), 2019; Thal et al., J Cell Mol Med 12(5B):1848–62, 2008;Smith et al., eLife 6, 2017). Several studies have shown microstructural changes to the brain parenchyma resulting from a variety of injury and disease states, such as traumatic brain injury (TBI), Alzheimer's and Parkinson's diseases, depression, and aging (Ayad et al., Philos Trans R Soc Lond Ser B Biol Sci 374(1779):20180215, 2019). As a result, brain microstructure has garnered significant attention in recent years from scientists and engineers as a neurological and micromechanical sink – an unexplored frontier for disease progression and a critical barrier to therapeutic delivery in the brain.

CHAPTER 6 CURRICULUM VITAE

Education

2022- 2026 Ph.D. in Chemistry, University of Washington, Seattle
Disease Directed Engineering lab in the Department of Chemical Engineering; PI: Dr. Elizabeth Nance
Expected thesis defense: Spring 2026

2020- 2022 M.Sc. in Applied Chemical Science and Technology, University of Washington, Seattle
Thesis title: Machine Learning Methods for Analyzing Biological Multiple Particle
Tracking Data

2016-2020 B.S. in Biochemistry. University of Washington, Seattle

Skills:

Technical: MS Office suite, Adobe Creative Suite, Programming/Scripting (Python, R, MATLAB, Bash), Git, Unit testing, Cloud Computing and Deployment (Azure), Database and Data Pipeline Design, Web App Framework (Streamlit), ML/Deep-learning, High Performance Cluster Computing, and Project management (GitHub Projects, Trello)

Organizational: Public speaking, scientific writing, interdisciplinary communication, mentorship

Research Experience

Doctoral Researcher, University of Washington **Sept 2022 - Present**

- Developed diff_viz, an open-source software package and web application to improve, reproducibility, efficiency, and accessibility of visualizing multiple particle tracking data
- Developed an open-source software package to automate processing of nanoparticle tracking data, leading to decreased processing time and increased reproducibility.
- Performed statistical and visual analysis to identify sources of experimental noise in multiple particle tracking.
- Leveraged explainable machine learning, cloud computing, and data visualization to find statistically significant differences and non-linear effects in multiple particle tracking data from healthy brain slices compared to two disease conditions and across regions.

- Used unsupervised learning, tree-based methods, and linear mixed effects models to characterize how microglia morphologies change during development across age, species, and sex.
- Designed and implemented a method of collecting nanoparticle diffusion data near microglia in cell-seeded gels to understand the role of microglia in modulating the local microenvironment.
- Developed pipelines in Python to quantify the spatial relationship of mitochondria and nanoparticle diffusion to microglia in healthy and diseased states.

Masters Researcher, University of Washington **Sept 2020 - 2022**

- Development and testing of diff_predictor, an open-source software package for machine learning analysis of multiple particle tracking data
- Applied diff_predictor to generate machine learning predictions and feature importance values to gain insight into age, region, and treatment-based biological changes in the brain extracellular space.
- Used Tensorflow to train Convolutional Neural Networks to classify multiple particle tracking trajectories

Undergraduate research assistant, University of Washington **Sept 2016 - Sept 2020**
Department of Neurosurgery; PI: Dr. Pierre Mourad

- Design and execution of neuromodulation experiments in rodents and human using medical ultrasound to probe the visual cortex
- Developed MATLAB scripts to visualize and perform statistical analysis on EEG data

Work Experience

Student assistant, University of Washington Department of Biology **Oct 2021 – Feb 2022**

- Integration and unit testing of SEIRS+, an open-source python package for dynamic epidemiological modeling.
- Deployment of SEIRS+ package for simulation-based case studies on spread and methods of intervention for COVID19

Publications

Schimek, N., Beck, D., Wood, T., Mckenna, M., Nance, E*. High fidelity predictions of diffusion in the brain microenvironment. Biophys J. (2024), Vol 123, Issue 22, 3935 – 3950. doi: 10.1016/j.bpj.2024.10.005

McKenna M., Filteau J., Sluis K., Chungyoun M., Butler B., **Schimek N**., Nance E.* Organotypic whole hemisphere brain slice models to study the effects of donor age and oxygen-glucose-deprivation on the extracellular properties of cortical and striatal tissue; *Journal of Biological Engineering* (2022); 16:14; doi: 10.1186/s13036-022-00293-w

Schimek, N., Filteau J., Butler, B., Nance, E.* (2022). Nano-Based Probes for the Brain Extracellular Environment. In: Nance, E. (eds) Engineering Biomaterials for Neural Applications. Springer, Cham. https://doi.org/10.1007/978-3-031-11409-0_2

Schimek, N., Burke-Conte, Z., Abernethy, J., Schimek, M., Burke-Conte, C., Bobola, M., Stocco, A., Mourad, P *. (2020). Repeated Application of Transcranial Diagnostic Ultrasound Towards the Visual Cortex Induced Illusory Visual Percepts in Healthy Participants. *Front. Hum. Neurosci.* 14, 66. doi:10.3389/fnhum.2020.00066.

Bobola, M. S., Chen, L., Ezeokeke, C. K., Kuznetsova, K., Lahti, A. C., Lou, W., **Schimek, N.,** Mourad, P *. (2018). A Review of Recent Advances in Ultrasound, Placed in the Context of Pain Diagnosis and Treatment. *Curr. Pain Headache Rep.* 22, 60. doi:10.1007/s11916-018-0711-7.

Presentations

Schimek, N., M., Beck, D., Wood, T., Mckenna, M., Nance, E. High fidelity predictions of diffusion in the brain microenvironment. Oral presentation given at: 2024 AIChE Annual Meeting; October 2024; San Diego, CA

Schimek, N., Butler, B., Calmidi, M., Yamada-Heidner, M., Beck, D., Mckenna, M., Nance, E. Multiple particle tracking data analyzed with machine learning to predict complex biological variables. Oral presentation given at: 2023 BMES Annual Meeting; October 2023; Seattle, WA

Schimek, N., Butler, B., Calmidi, M., Yamada-Heidner, M., Beck, D., Mckenna, M., Nance, E. Multiple particle tracking data analyzed with machine learning to predict complex biological variables. Oral presentation given at: 2023 ACES Graduate Student Symposium; September 2023; Seattle, WA

Schimek, N., Butler, B., Beck, D., Mckenna, M., Nance, E. Multiple particle tracking data analyzed with machine learning to predict complex biological variables. Poster presented at: 2023 Machine Learning for Computational Biology; November 2023; Seattle, WA.

Mentoring

Undergraduate mentor, Nance Lab, University of Washington **June 2021 - Present**

Continuously mentored undergraduate students in the Nance Lab in software development and data science.

Manasvini Calmidi: Database development and data visualization for experimental nanoparticle data
Mia Yamada-Heidner: Development of software to compare many ML model architectures on particle tracking data
Ali Toghani: Applications of Transformer-based neural networks for Multiple Particle Tracking data

Mia Onodera: Development of open software package for pre-processing of cell morphology data
Sanjana: Data pipeline design and image analysis of pericyte morphology data
Assaf Golan: Contrastive Learning and Autoencoders networks applied to microglia images

Teaching

Hackathon tutorial instructor, UW Department of Chemical Engineering
Assisted Chemical Engineering undergraduates in learning introductory Python and data science topics.

TEXTILE, UW Department of Chemical Engineering
Taught and developed new learning modules for TEXTILE, a lab developed framework for teaching data science to high school, undergraduate, and graduate researchers in the summer of 2022 and 2023.

Teaching Assistant, UW Department of Chemical Engineering
Led office hours and graded homework and projects for 150+ graduate students across three courses: UW CSE 583, UW ChemE 545, UW ChemE 546.

Leadership

Cloud Computing Officer, University of Washington Research Computing Club. Dec 2023 – August 2025

Funding and Awards

UW ITHS TL1 Translational Research Fellowship. June 2025 to June 2026
UW Institute of Translational Health and Sciences

UW Azure Cloud Computing Credits for Research. Dec. 2022 - June 2023
UW eScience Institute

UW Azure Cloud Computing Credits for Research. Dec. 2021 - June 2022
UW eScience Institute

UW Azure Cloud Computing Credits for Research. Dec. 2020 - June 2021
UW eScience Institute

Summer Undergraduate Research Program grant. June 2018 - Aug. 2018
Washington NASA Space Grant Consortium

REFERENCES

1. Oberheim, N. A., Goldman, S. A. & Nedergaard, M. Heterogeneity of astrocytic form and function. *Methods Mol Biol* **814**, 23–45 (2012).
2. Hahn, J., Wang, X. & Margeta, M. Astrocytes increase the activity of synaptic GluN2B NMDA receptors. *Front Cell Neurosci* **9**, 117 (2015).
3. Ma, Y. *et al.* Targeting blood brain barrier-Remote ischemic conditioning alleviates cognitive impairment in female APP/PS1 rats. *CNS Neurosci Ther* **30**, e14613 (2024).
4. Piaton, G., Gould, R. M. & Lubetzki, C. Axon-oligodendrocyte interactions during developmental myelination, demyelination and repair. *J Neurochem* **114**, 1243–1260 (2010).
5. Philips, T. & Rothstein, J. D. Oligodendroglia: metabolic supporters of neurons. *J Clin Invest* **127**, 3271–3280 (2017).
6. Koreman, E., Sun, X. & Lu, Q. R. Chromatin remodeling and epigenetic regulation of oligodendrocyte myelination and myelin repair. *Mol Cell Neurosci* **87**, 18–26 (2018).
7. Nimmerjahn, A., Kirchhoff, F. & Helmchen, F. Resting microglial cells are highly dynamic surveillants of brain parenchyma in vivo. *Science* **308**, 1314–1318 (2005).
8. Davalos, D. *et al.* ATP mediates rapid microglial response to local brain injury in vivo. *Nat Neurosci* **8**, 752–758 (2005).
9. Long, K. R. & Huttner, W. B. How the extracellular matrix shapes neural development. *Open Biol.* **9**, 180216 (2019).
10. Suttkus, A., Morawski, M. & Arendt, T. Protective Properties of Neural Extracellular Matrix. *Mol Neurobiol* **53**, 73–82 (2016).
11. Barros, C. S., Franco, S. J. & Müller, U. Extracellular matrix: functions in the nervous system. *Cold Spring Harb Perspect Biol* **3**, a005108 (2011).

12. Syková, E. & Nicholson, C. Diffusion in brain extracellular space. *Physiol Rev* **88**, 1277–1340 (2008).

13. Kamali-Zare, P. & Nicholson, C. Brain extracellular space: geometry, matrix and physiological importance. *Basic Clin Neurosci* **4**, 282–286 (2013).

14. Ruoslahti, E. Brain extracellular matrix. *Glycobiology* **6**, 489–492 (1996).

15. Jenkins, H. G. & Bachelard, H. S. Developmental and age-related changes in rat brain glycosaminoglycans. *J Neurochem* **51**, 1634–1640 (1988).

16. Novak, U. & Kaye, A. H. Extracellular matrix and the brain: components and function. *J Clin Neurosci* **7**, 280–290 (2000).

17. Yamaguchi, Y. Lecticans: organizers of the brain extracellular matrix. *Cell Mol Life Sci* **57**, 276–289 (2000).

18. Margolis, R. K. & Margolis, R. U. Nervous tissue proteoglycans. *Experientia* **49**, 429–446 (1993).

19. Fawcett, J. W. *et al.* The extracellular matrix and perineuronal nets in memory. *Mol Psychiatry* **27**, 3192–3203 (2022).

20. Brückner, G. *et al.* Extracellular matrix organization in various regions of rat brain grey matter. *J Neurocytol* **25**, 333–346 (1996).

21. Dauth, S. *et al.* Extracellular matrix protein expression is brain region dependent. *J Comp Neurol* **524**, 1309–1336 (2016).

22. Barry-Carroll, L. *et al.* Microglia colonize the developing brain by clonal expansion of highly proliferative progenitors, following allometric scaling. *Cell Reports* **42**, 112425 (2023).

23. Matcovitch-Natan, O. *et al.* Microglia development follows a stepwise program to regulate brain homeostasis. *Science* **353**, aad8670 (2016).

24. Ginhoux, F. *et al.* Fate Mapping Analysis Reveals That Adult Microglia Derive from Primitive Macrophages. *Science* **330**, 841–845 (2010).

25. Zusso, M. *et al.* Regulation of postnatal forebrain amoeboid microglial cell proliferation and development by the transcription factor Runx1. *J Neurosci* **32**, 11285–11298 (2012).

26. Hammond, B. P., Manek, R., Kerr, B. J., Macauley, M. S. & Plemel, J. R. Regulation of microglia population dynamics throughout development, health, and disease. *Glia* **69**, 2771–2797 (2021).

27. Mehl, L. C., Manjally, A. V., Bouadi, O., Gibson, E. M. & Tay, T. L. Microglia in brain development and regeneration. *Development* **149**, dev200425 (2022).

28. Lehmenkühler, A., Syková, E., Svoboda, J., Zilles, K. & Nicholson, C. Extracellular space parameters in the rat neocortex and subcortical white matter during postnatal development determined by diffusion analysis. *Neuroscience* **55**, 339–351 (1993).

29. McKenna, M., Shackelford, D., Pontes, C., Ball, B. & Nance, E. Multiple Particle Tracking Detects Changes in Brain Extracellular Matrix and Predicts Neurodevelopmental Age. *ACS Nano* **15**, 8559–8573 (2021).

30. Sirko, S., Von Holst, A., Wizenmann, A., Götz, M. & Faissner, A. Chondroitin sulfate glycosaminoglycans control proliferation, radial glia cell differentiation and neurogenesis in neural stem/progenitor cells. *Development* **134**, 2727–2738 (2007).

31. Hall, P. E., Lathia, J. D., Caldwell, M. A. & Ffrench-Constant, C. Laminin enhances the growth of human neural stem cells in defined culture media. *BMC Neurosci* **9**, 71 (2008).

32. Hohenester, E. & Yurchenco, P. D. Laminins in basement membrane assembly. *Cell Adh Migr* **7**, 56–63 (2013).

33. Chen, Z.-L., Haegeli, V., Yu, H. & Strickland, S. Cortical deficiency of laminin gamma1 impairs the AKT/GSK-3beta signaling pathway and leads to defects in neurite outgrowth and neuronal migration. *Dev Biol* **327**, 158–168 (2009).

34. Tsuda, S. *et al.* FAK-mediated extracellular signals are essential for interkinetic nuclear migration and planar divisions in the neuroepithelium. *J Cell Sci* **123**, 484–496 (2010).

35. Long, K. R. *et al.* Extracellular Matrix Components HAPLN1, Lumican, and Collagen I Cause Hyaluronic Acid-Dependent Folding of the Developing Human Neocortex. *Neuron* **99**, 702-719.e6 (2018).

36. Bahia, C. P., Houzel, J., Picanço-Diniz, C. W. & Pereira, A. Spatiotemporal distribution of proteoglycans in the developing rat's barrel field and the effects of early deafferentation. *J of Comparative Neurology* **510**, 145–157 (2008).

37. Yue, L., Craig, M. T. & Morris, B. J. Glucocorticoids Modulate Expression of Perineuronal Net Component Genes and Parvalbumin During Development of Mouse Cortical Neurons. *Mol Neurobiol* **63**, 205 (2025).

38. Van't Spijker, H. M. & Richter, J. D. FMRP regulation of aggrecan mRNA translation controls perineuronal net development. *J Neurochem* **168**, 1909–1922 (2024).

39. Barros, D., Amaral, I. F. & Pêgo, A. P. Laminin-Inspired Cell-Instructive Microenvironments for Neural Stem Cells. *Biomacromolecules* **21**, 276–293 (2020).

40. Leivo, I., Vaheri, A., Timpl, R. & Wartiovaara, J. Appearance and distribution of collagens and laminin in the early mouse embryo. *Developmental Biology* **76**, 100–114 (1980).

41. Sertie, A. L. Collagen XVIII, containing an endogenous inhibitor of angiogenesis and tumor growth, plays a critical role in the maintenance of retinal structure and in neural tube closure (Knobloch syndrome). *Human Molecular Genetics* **9**, 2051–2058 (2000).

42. Fox, M. A. Novel roles for collagens in wiring the vertebrate nervous system. *Current Opinion in Cell Biology* **20**, 508–513 (2008).

43. Wilson, E., Knudson, W. & Newell-Litwa, K. Hyaluronan regulates synapse formation and function in developing neural networks. *Sci Rep* **10**, 16459 (2020).

44. Baier, C. *et al.* Hyaluronan is organized into fiber-like structures along migratory pathways in the developing mouse cerebellum. *Matrix Biology* **26**, 348–358 (2007).

45. Safaiyan, S. *et al.* White matter aging drives microglial diversity. *Neuron* **109**, 1100-1117.e10 (2021).

46. Pereira-Iglesias, M. *et al.* Microglia as hunters or gatherers of brain synapses. *Nat Neurosci* **28**, 15–23 (2025).

47. Holtman, I. R. *et al.* Induction of a common microglia gene expression signature by aging and neurodegenerative conditions: a co-expression meta-analysis. *Acta Neuropathol Commun* **3**, 31 (2015).

48. Kettenmann, H., Hanisch, U.-K., Noda, M. & Verkhratsky, A. Physiology of Microglia. *Physiological Reviews* **91**, 461–553 (2011).

49. Liu, Y.-J. *et al.* Microglia Elimination Increases Neural Circuit Connectivity and Activity in Adult Mouse Cortex. *J Neurosci* **41**, 1274–1287 (2021).

50. Tansley, S. *et al.* Microglia-mediated degradation of perineuronal nets promotes pain. *Science* **377**, 80–86 (2022).

51. Yang, S. *et al.* Chondroitin 6-sulphate is required for neuroplasticity and memory in ageing. *Mol Psychiatry* **26**, 5658–5668 (2021).

52. Sugitani, K. *et al.* Hyaluronan degradation and release of a hyaluronan-aggrecan complex from perineuronal nets in the aged mouse brain. *Biochim Biophys Acta Gen Subj* **1865**, 129804 (2021).

53. D'Agostino, A. *et al.* Is molecular size a discriminating factor in hyaluronan interaction with human cells? *Carbohydr Polym* **157**, 21–30 (2017).

54. Hawkes, C. A. *et al.* Regional differences in the morphological and functional effects of aging on cerebral basement membranes and perivascular drainage of amyloid-β from the mouse brain. *Aging Cell* **12**, 224–236 (2013).

55. Imamura, K. *et al.* Distribution of major histocompatibility complex class II-positive microglia and cytokine profile of Parkinson's disease brains. *Acta Neuropathologica* **106**, 518–526 (2003).

56. Bourne, J. H. *et al.* Microglia are prominent producers of inflammatory cytokines during the hyperacute phase of ischemic stroke. *Commun Biol* **8**, 1193 (2025).

57. Obukohwo, O. M., Oreoluwa, O. A., Andrew, U. O. & Williams, U. E. Microglia-mediated neuroinflammation in traumatic brain injury: a review. *Mol Biol Rep* **51**, 1073 (2024).

58. De Bilbao, F. *et al. In vivo* over-expression of interleukin-10 increases resistance to focal brain ischemia in mice. *Journal of Neurochemistry* **110**, 12–22 (2009).

59. Rauti, R. *et al.* BDNF impact on synaptic dynamics: extra or intracellular long-term release differently regulates cultured hippocampal synapses. *Mol Brain* **13**, 43 (2020).

60. Madinier, A. *et al.* Microglial involvement in neuroplastic changes following focal brain ischemia in rats. *PLoS One* **4**, e8101 (2009).

61. del Zoppo, G. J. *et al.* Microglial cell activation is a source of metalloproteinase generation during hemorrhagic transformation. *J Cereb Blood Flow Metab* **32**, 919–932 (2012).

62. Rosell, A. *et al.* Increased brain expression of matrix metalloproteinase-9 after ischemic and hemorrhagic human stroke. *Stroke* **37**, 1399–1406 (2006).

63. Chan, T. Y. H., Ma, B. D. Y., Hung, T. K., Wong, J. S. Y. & Lo, B. W. Y. Microglial Polarization and Therapeutic Strategies in Post-stroke Neuroinflammation. *Neurol Ther* **14**, 2277–2293 (2025).

64. Dal Bianco, A. *et al.* Multiple sclerosis and Alzheimer's disease. *Ann Neurol* **63**, 174–183 (2008).

65. Dickson, D. W. Parkinson's disease and parkinsonism: neuropathology. *Cold Spring Harb Perspect Med* **2**, a009258 (2012).

66. d'Errico, P. *et al.* Microglia contribute to the propagation of Aβ into unaffected brain tissue. *Nat Neurosci* **25**, 20–25 (2022).

67. Binnion, P. F. & Das Gupta, R. Prophylactic antiarrhythmic drug therapy in acute myocardial infarction. *Cardiovasc Clin* **7**, 203–217 (1975).

68. Gordon, R. *et al.* Inflammasome inhibition prevents α-synuclein pathology and dopaminergic neurodegeneration in mice. *Sci Transl Med* **10**, eaah4066 (2018).

69. Haque, M. E. *et al.* Targeting the microglial NLRP3 inflammasome and its role in Parkinson's disease. *Mov Disord* **35**, 20–33 (2020).

70. Choi, I. *et al.* Microglia clear neuron-released α-synuclein via selective autophagy and prevent neurodegeneration. *Nat Commun* **11**, 1386 (2020).

71. Bartels, T., De Schepper, S. & Hong, S. Microglia modulate neurodegeneration in Alzheimer's and Parkinson's diseases. *Science* **370**, 66–69 (2020).

72. Lyall, A. E. *et al.* Greater extracellular free-water in first-episode psychosis predicts better neurocognitive functioning. *Mol Psychiatry* **23**, 701–707 (2018).

73. Seitz-Holland, J. *et al.* Matrix metalloproteinase 9 (MMP-9) activity, hippocampal extracellular free water, and cognitive deficits are associated with each other in early phase psychosis. *Neuropsychopharmacol.* **49**, 1140–1150 (2024).

74. Syková, E. *et al.* Changes in extracellular space size and geometry in APP23 transgenic mice: A model of Alzheimer's disease. *Proc. Natl. Acad. Sci. U.S.A.* **102**, 479–484 (2005).

75. Tureckova, J. *et al.* Compromised Astrocyte Swelling/Volume Regulation in the Hippocampus of the Triple Transgenic Mouse Model of Alzheimer's Disease. *Front. Aging Neurosci.* **13**, 783120 (2022).

76. Shen, T. *et al.* Diffusion along perivascular spaces as marker for impairment of glymphatic system in Parkinson's disease. *npj Parkinsons Dis.* **8**, 174 (2022).

77. McKnight, C. D. *et al.* Diffusion along perivascular spaces reveals evidence supportive of glymphatic function impairment in Parkinson disease. *Parkinsonism & Related Disorders* **89**, 98–104 (2021).

78. Ma, X. *et al.* Diffusion Tensor Imaging Along the Perivascular Space Index in Different Stages of Parkinson's Disease. *Front. Aging Neurosci.* **13**, 773951 (2021).

79. Sun, Y. *et al.* Role of the Extracellular Matrix in Alzheimer's Disease. *Front. Aging Neurosci.* **13**, 707466 (2021).

80. Griffiths, D. R., Jenkins, T. M., Addington, C. P., Stabenfeldt, S. E. & Lifshitz, J. Extracellular matrix proteins are time-dependent and regional-specific markers in experimental diffuse brain injury. *Brain and Behavior* **10**, e01767 (2020).

81. George, N. & Geller, H. M. Extracellular matrix and traumatic brain injury. *J of Neuroscience Research* **96**, 573–588 (2018).

82. Nicholson, C. & Syková, E. Extracellular space structure revealed by diffusion analysis. *Trends in Neurosciences* **21**, 207–215 (1998).

83. Syková, E. Extrasynaptic volume transmission and diffusion parameters of the extracellular space. *Neuroscience* **129**, 861–876 (2004).

84. Vorísek, I. & Syková, E. Evolution of anisotropic diffusion in the developing rat corpus callosum. *J Neurophysiol* **78**, 912–919 (1997).

85. Kume-Kick, J. *et al.* Independence of extracellular tortuosity and volume fraction during osmotic challenge in rat neocortex. *The Journal of Physiology* **542**, 515–527 (2002).

86. Hrabětová, S., Hrabe, J. & Nicholson, C. Dead-Space Microdomains Hinder Extracellular Diffusion in Rat Neocortex during Ischemia. *J. Neurosci.* **23**, 8351–8359 (2003).

87. Rice, M. E. & Nicholson, C. Diffusion characteristics and extracellular volume fraction during normoxia and hypoxia in slices of rat neostriatum. *J Neurophysiol* **65**, 264–272 (1991).

88. Syková, E., Voříšek, I., Mazel, T., Antonova, T. & Schachner, M. Reduced extracellular space in the brain of tenascin-R- and HNK-1-sulphotransferase deficient mice. *Eur J of Neuroscience* **22**, 1873–1880 (2005).

89. Syková, E., Svoboda, J., Šimonová, Z., Lehmenkühler, A. & Lassmann, H. X-irradiation-induced changes in the diffusion parameters of the developing rat brain. *Neuroscience* **70**, 597–612 (1996).

90. Nance, E. A. *et al.* A dense poly(ethylene glycol) coating improves penetration of large polymeric nanoparticles within brain tissue. *Sci Transl Med* **4**, 149ra119 (2012).

91. Paviolo, C. *et al.* Nanoscale exploration of the extracellular space in the live brain by combining single carbon nanotube tracking and super-resolution imaging analysis. *Methods* **174**, 91–99 (2020).

92. Manzo, C. & Garcia-Parajo, M. F. A review of progress in single particle tracking: from methods to biophysical insights. *Rep Prog Phys* **78**, 124601 (2015).

93. Godin, A. G. *et al.* Single-nanotube tracking reveals the nanoscale organization of the extracellular space in the live brain. *Nature Nanotech* **12**, 238–243 (2017).

94. Paviolo, C. & Cognet, L. Near-infrared nanoscopy with carbon-based nanoparticles for the exploration of the brain extracellular space. *Neurobiol Dis* **153**, 105328 (2021).

95. Soria, F. N. *et al.* Synucleinopathy alters nanoscale organization and diffusion in the brain extracellular space through hyaluronan remodeling. *Nat Commun* **11**, 3440 (2020).

96. McKenna, M. *et al.* Organotypic whole hemisphere brain slice models to study the effects of donor age and oxygen-glucose-deprivation on the extracellular properties of cortical and striatal tissue. *J Biol Eng* **16**, 14 (2022).

97. Joseph, A. *et al.* Nanoparticle-microglial interaction in the ischemic brain is modulated by injury duration and treatment. *Bioengineering & Transla Med* **5**, e10175 (2020).

98. Caliari, S. R. & Burdick, J. A. A practical guide to hydrogels for cell culture. *Nat Methods* **13**, 405–414 (2016).

99. Prince, E. & Kumacheva, E. Design and applications of man-made biomimetic fibrillar hydrogels. *Nat Rev Mater* **4**, 99–115 (2019).

100. Griffith, L. G. & Swartz, M. A. Capturing complex 3D tissue physiology in vitro. *Nat Rev Mol Cell Biol* **7**, 211–224 (2006).

101. Loebel, C. *et al.* Metabolic labeling of secreted matrix to investigate cell–material interactions in tissue engineering and mechanobiology. *Nat Protoc* **17**, 618–648 (2022).

102. Accardo, A. *et al.* Direct laser fabrication of free-standing PEGDA-hydrogel scaffolds for neuronal cell growth. *Materials Today* **21**, 315–316 (2018).

103. Chapla, R., Katz, R. R. & West, J. L. Neurogenic Cell Behavior in 3D Culture Enhanced Within a Highly Compliant Synthetic Hydrogel Platform Formed via Competitive Crosslinking. *Cell Mol Bioeng* **17**, 35–48 (2024).

104. Her, G. J. *et al.* Control of three-dimensional substrate stiffness to manipulate mesenchymal stem cell fate toward neuronal or glial lineages. *Acta Biomaterialia* **9**, 5170–5180 (2013).

105. Hu, Y., Liu, S., Lu, T., Wei, Z. & Xu, F. Viscoelastic microenvironment as key regulators of astrocyte behavior in brain injury and scar formation. *Acta Mech. Sin.* **42**, 624671 (2026).

106. Balion, Z. *et al.* Comparison of Microglial Morphology and Function in Primary Cerebellar Cell Cultures on Collagen and Collagen-Mimetic Hydrogels. *Biomedicines* **10**, 1023 (2022).

107. Rao, S. S. *et al.* Glioblastoma behaviors in three-dimensional collagen-hyaluronan composite hydrogels. *ACS Appl Mater Interfaces* **5**, 9276–9284 (2013).

108. Cui, Y. *et al.* Evaluating glioblastoma tumour sphere growth and migration in interaction with astrocytes using 3D collagen-hyaluronic acid hydrogels. *J. Mater. Chem. B* **11**, 5442–5459 (2023).

109. Koss, K. M. *et al.* Improved 3D Hydrogel Cultures of Primary Glial Cells for In Vitro Modelling of Neuroinflammation. *J Vis Exp* 56615 (2017) doi:10.3791/56615.

110. Haw, R. T. Y. *et al.* A three-dimensional collagen construct to model lipopolysaccharide-induced activation of BV2 microglia. *J Neuroinflammation* **11**, 134 (2014).

111. Nguyen, N. P. *et al.* Brain Tissue-Derived Extracellular Vesicle Mediated Therapy in the Neonatal Ischemic Brain. *IJMS* **23**, 620 (2022).

112. Gähwiler, B. H., Capogna, M., Debanne, D., McKinney, R. A. & Thompson, S. M. Organotypic slice cultures: a technique has come of age. *Trends Neurosci* **20**, 471–477 (1997).

113. Humpel, C. Organotypic brain slice cultures: A review. *Neuroscience* **305**, 86–98 (2015).

114. Wood, T. R. *et al.* A ferret brain slice model of oxygen–glucose deprivation captures regional responses to perinatal injury and treatment associated with specific microglial phenotypes. *Bioengineering & Transla Med* **7**, e10265 (2022).

115. Liao, R., Wood, T. R. & Nance, E. Superoxide dismutase reduces monosodium glutamate-induced injury in an organotypic whole hemisphere brain slice model of excitotoxicity. *J Biol Eng* **14**, 3 (2020).

116. Curtis, C. *et al.* Predicting *in situ* nanoparticle behavior using multiple particle tracking and artificial neural networks. *Nanoscale* **11**, 22515–22530 (2019).

117. Kowalek, P., Loch-Olszewska, H. & Szwabiński, J. Classification of diffusion modes in single-particle tracking data: Feature-based versus deep-learning approach. *Phys. Rev. E* **100**, 032410 (2019).

118. Wagner, T., Kroll, A., Haramagatti, C. R., Lipinski, H.-G. & Wiemann, M. Classification and Segmentation of Nanoparticle Diffusion Trajectories in Cellular Micro Environments. *PLoS One* **12**, e0170165 (2017).

119. Kaler, L., Joyner, K. & Duncan, G. Machine learning-informed timescale dependent modes of nanoparticle diffusion through human mucus. *Biophysical Journal* **121**, 121a (2022).

120. Helmbrecht, H., Lin, T.-J., Janakiraman, S., Decker, K. & Nance, E. Prevalence and practices of immunofluorescent cell image processing: a systematic review. *Front. Cell. Neurosci.* **17**, 1188858 (2023).

121. Maya-Arteaga, J. P., Martínez-Orozco, H. & Diaz-Cintra, S. MorphoGlia, an interactive method to identify and map microglia morphologies, demonstrates differences in hippocampal subregions of an Alzheimer's disease mouse model. *Front. Cell. Neurosci.* **18**, 1505048 (2024).

122. Reddaway, J., Richardson, P. E., Bevan, R. J., Stoneman, J. & Palombo, M. Microglial morphometric analysis: so many options, so little consistency. *Front. Neuroinform.* **17**, 1211188 (2023).

123. Hsu, C.-H. *et al.* StainAI: quantitative mapping of stained microglia and insights into brain-wide neuroinflammation and therapeutic effects in cardiac arrest. *Commun Biol* **8**, 462 (2025).

124. Soltys, Z. *et al.* Quantitative morphological study of microglial cells in the ischemic rat brain using principal component analysis. *Journal of Neuroscience Methods* **146**, 50–60 (2005).

125. Benkeder, S. *et al.* MorphoCellSorter is an Andrews plot-based sorting approach to rank microglia according to their morphological features. *Elife* **13**, RP101630 (2025).

126. Fernández-Arjona, M. D. M., Grondona, J. M., Granados-Durán, P., Fernández-Llebrez, P. & López-Ávalos, M. D. Microglia Morphological Categorization in a Rat Model of

Neuroinflammation by Hierarchical Cluster and Principal Components Analysis. *Front. Cell. Neurosci.* **11**, 235 (2017).

127. Leyh, J. *et al.* Classification of Microglial Morphological Phenotypes Using Machine Learning. *Front. Cell. Neurosci.* **15**, 701673 (2021).

128. Clarke, D., Crombag, H. S. & Hall, C. N. An open-source pipeline for analysing changes in microglial morphology. *Open Biol* **11**, 210045 (2021).

129. Sumberg, L. *et al.* A Semi-Automated and Unbiased Microglia Morphology Analysis Following Mild Traumatic Brain Injury in Rats. *IJMS* **26**, 8149 (2025).

130. Phillip, J. M., Han, K.-S., Chen, W.-C., Wirtz, D. & Wu, P.-H. A robust unsupervised machine-learning method to quantify the morphological heterogeneity of cells and nuclei. *Nat Protoc* **16**, 754–774 (2021).

131. Begley, C. G. & Ioannidis, J. P. A. Reproducibility in science: improving the standard for basic and preclinical research. *Circ Res* **116**, 116–126 (2015).

132. Feger, S. S. & Woźniak, P. W. Reproducibility: A Researcher-Centered Definition. *MTI* **6**, 17 (2022).

133. Barba, L. A. Defining the Role of Open Source Software in Research Reproducibility. *Computer* **55**, 40–48 (2022).

134. Ivie, P. & Thain, D. Reproducibility in Scientific Computing. *ACM Comput. Surv.* **51**, 1–36 (2019).

135. Chue Hong, N. P. *et al.* FAIR Principles for Research Software (FAIR4RS Principles). https://doi.org/10.15497/RDA00068 (2021) doi:10.15497/RDA00068.

136. Barker, M. *et al.* Introducing the FAIR Principles for research software. *Sci Data* **9**, 622 (2022).

137. Benureau, F. C. Y. & Rougier, N. P. Re-run, Repeat, Reproduce, Reuse, Replicate: Transforming Code into Scientific Contributions. *Front. Neuroinform.* **11**, 69 (2018).

138. Bowman, R. W. Improving instrument reproducibility with open source hardware. *Nat Rev Methods Primers* **3**, 27 (2023).

139. Dozmorov, M. G. GitHub Statistics as a Measure of the Impact of Open-Source Bioinformatics Software. *Front Bioeng Biotechnol* **6**, 198 (2018).

140. Thorne, R. G. & Nicholson, C. *In vivo* diffusion analysis with quantum dots and dextrans predicts the width of brain extracellular space. *Proc. Natl. Acad. Sci. U.S.A.* **103**, 5567–5572 (2006).

141. Nance, E. Brain-Penetrating Nanoparticles for Analysis of the Brain Microenvironment. *Methods Mol Biol* **1570**, 91–104 (2017).

142. Chen, T. & Guestrin, C. XGBoost: A Scalable Tree Boosting System. in *Proceedings of the 22nd ACM SIGKDD International Conference on Knowledge Discovery and Data Mining* 785–794 (ACM, San Francisco California USA, 2016). doi:10.1145/2939672.2939785.

143. Lundberg, S. M. *et al.* From local explanations to global understanding with explainable AI for trees. *Nat Mach Intell* **2**, 56–67 (2020).

144. Nguyen, N. P. *et al.* Brain Tissue-Derived Extracellular Vesicle Mediated Therapy in the Neonatal Ischemic Brain. *IJMS* **23**, 620 (2022).

145. Lensjø, K. K., Christensen, A. C., Tennøe, S., Fyhn, M. & Hafting, T. Differential Expression and Cell-Type Specificity of Perineuronal Nets in Hippocampus, Medial Entorhinal Cortex, and Visual Cortex Examined in the Rat and Mouse. *eNeuro* **4**, ENEURO.0379-16.2017 (2017).

146. Margolis, R. U., Margolis, R. K., Chang, L. B. & Preti, C. Glycosaminoglycans of brain during development. *Biochemistry* **14**, 85–88 (1975).

147. Mengler, L. *et al.* Brain maturation of the adolescent rat cortex and striatum: changes in volume and myelination. *Neuroimage* **84**, 35–44 (2014).

148. Budin, F. *et al.* Fully automated rodent brain MR image processing pipeline on a Midas server: from acquired images to region-based statistics. *Front Neuroinform* **7**, 15 (2013).

149. Furube, E., Kawai, S., Inagaki, H., Takagi, S. & Miyata, S. Brain Region-dependent Heterogeneity and Dose-dependent Difference in Transient Microglia Population Increase during Lipopolysaccharide-induced Inflammation. *Sci Rep* **8**, 2203 (2018).

150. Cavaglia, M. *et al.* Regional variation in brain capillary density and vascular response to ischemia. *Brain Res* **910**, 81–93 (2001).

151. Chen, R. J., Lu, M. Y., Chen, T. Y., Williamson, D. F. K. & Mahmood, F. Synthetic data in machine learning for medicine and healthcare. *Nat Biomed Eng* **5**, 493–497 (2021).

152. Katz, M. J. & George, E. B. Fractals and the analysis of growth paths. *Bull Math Biol* **47**, 273–286 (1985).

153. Zoremba, N., Homola, A., Rossaint, R. & Syková, E. Brain metabolism and extracellular space diffusion parameters during and after transient global hypoxia in the rat cortex. *Exp Neurol* **203**, 34–41 (2007).

154. Girard, S. *et al.* Microglia and macrophages differentially modulate cell death after brain injury caused by oxygen-glucose deprivation in organotypic brain slices. *Glia* **61**, 813–824 (2013).

155. Hrabetova, S., Cognet, L., Rusakov, D. A. & Nägerl, U. V. Unveiling the Extracellular Space of the Brain: From Super-resolved Microstructure to In Vivo Function. *J Neurosci* **38**, 9355–9363 (2018).

156. Granik, N. *et al.* Single-Particle Diffusion Characterization by Deep Learning. *Biophys J* **117**, 185–192 (2019).

157. Schneider, C. S. *et al.* Nanoparticles that do not adhere to mucus provide uniform and long-lasting drug delivery to airways following inhalation. *Sci Adv* **3**, e1601556 (2017).

158. Kaler, L. *et al.* Influenza A virus diffusion through mucus gel networks. *Commun Biol* **5**, 249 (2022).

159. Lukens, J. R. & Eyo, U. B. Microglia and Neurodevelopmental Disorders. *Annu. Rev. Neurosci.* **45**, 425–445 (2022).

160. Liu, Y.-J., Green, K. N., Holmes, T. C. & Xu, X. Commentary: How Do Microglia Regulate Neural Circuit Connectivity and Activity in the Adult Brain? *J Exp Neurosci* **17**, 26331055211071124 (2022).

161. Cowan, M. & Petri, W. A. Microglia: Immune Regulators of Neurodevelopment. *Front. Immunol.* **9**, 2576 (2018).

162. Bernis, M. E. *et al.* Temporal Characterization of Microglia-Associated Pro- and Anti-Inflammatory Genes in a Neonatal Inflammation-Sensitized Hypoxic-Ischemic Brain Injury Model. *Oxidative Medicine and Cellular Longevity* **2022**, 2479626 (2022).

163. Mallard, C. *et al.* Astrocytes and microglia in acute cerebral injury underlying cerebral palsy associated with preterm birth. *Pediatr Res* **75**, 234–240 (2014).

164. Mendes, M. S. & Majewska, A. K. An overview of microglia ontogeny and maturation in the homeostatic and pathological brain. *Eur J of Neuroscience* **53**, 3525–3547 (2021).

165. Zhan, L. *et al.* Proximal recolonization by self-renewing microglia re-establishes microglial homeostasis in the adult mouse brain. *PLoS Biol* **17**, e3000134 (2019).

166. Wu, Y., Dissing-Olesen, L., MacVicar, B. A. & Stevens, B. Microglia: Dynamic Mediators of Synapse Development and Plasticity. *Trends Immunol* **36**, 605–613 (2015).

167. Chen, J. Q. A. *et al.* Inflammatory microglia correlate with impaired oligodendrocyte maturation in multiple sclerosis. *Front Immunol* **15**, 1522381 (2024).

168. Han, T., Xu, Y., Sun, L., Hashimoto, M. & Wei, J. Microglial response to aging and neuroinflammation in the development of neurodegenerative diseases. *Neural Regen Res* **19**, 1241–1248 (2024).

169. Hu, Y. *et al.* Replicative senescence dictates the emergence of disease-associated microglia and contributes to Aβ pathology. *Cell Reports* **35**, 109228 (2021).

170. Trainor, A. R., MacDonald, D. S. & Penney, J. Microglia: roles and genetic risk in Parkinson's disease. *Front. Neurosci.* **18**, 1506358 (2024).

171. Li, Q. *et al.* Developmental heterogeneity of microglia and brain myeloid cells revealed by deep single-cell RNA sequencing. *Neuron* **101**, 207-223. e10 (2019).

172. Tsai, A. P. *et al.* Spatial and single-cell transcriptomics reveal the reorganization of cerebellar microglia with aging. *Cell Reports* **44**, 116624 (2025).

173. Androvic, P. *et al.* Spatial Transcriptomics-correlated Electron Microscopy maps transcriptional and ultrastructural responses to brain injury. *Nat Commun* **14**, 4115 (2023).

174. Tucker, E. W. *et al.* Microglia activation in a pediatric rabbit model of tuberculous meningitis. *Disease Models & Mechanisms* **9**, 1497–1506 (2016).

175. Garman, G. *et al.* An Automated Analysis Pipeline for Microglia Morphology in Nikon NIS-Elements. *Journal of Biomolecular Techniques* **36**, (2025).

176. Fernández-Arjona, M. D. M., Grondona, J. M., Fernández-Llebrez, P. & López-Ávalos, M. D. Microglial Morphometric Parameters Correlate With the Expression Level of IL-1β, and Allow Identifying Different Activated Morphotypes. *Front. Cell. Neurosci.* **13**, 472 (2019).

177. Bahng, H. *et al.* Unveiling CNS cell morphology with deep learning: A gateway to anti-inflammatory compound screening. *PLoS ONE* **20**, e0320204 (2025).

178. Shih, B. B. *et al.* Defining the pig microglial transcriptome reveals its core signature, regional heterogeneity, and similarity with human and rodent microglia. *Glia* **71**, 334–349 (2023).

179. Geirsdottir, L. *et al.* Cross-Species Single-Cell Analysis Reveals Divergence of the Primate Microglia Program. *Cell* **179**, 1609-1622.e16 (2019).

180. Carr, L. M. *et al.* Cross-species characterisation of microglial morphology and proliferation during ageing. *GeroScience* https://doi.org/10.1007/s11357-026-02254-3 (2026) doi:10.1007/s11357-026-02254-3.

181. Prater, K. E. *et al.* Human microglia show unique transcriptional changes in Alzheimer's disease. *Nat Aging* **3**, 894–907 (2023).

182. van der Walt, S. *et al.* scikit-image: image processing in Python. *PeerJ* **2**, e453 (2014).

183. Godeanu, S. *et al.* Microglial morphology in the somatosensory cortex across lifespan. A quantitative study. *Developmental Dynamics* **252**, 1113–1129 (2023).

184. Godeanu, S. & Cătălin, B. The Complementary Role of Morphology in Understanding Microglial Functional Heterogeneity. *IJMS* **26**, 3811 (2025).

185. Orłowski, D., Sołtys, Z. & Janeczko, K. Morphological development of microglia in the postnatal rat brain: A quantitative study. *Intl J of Devlp Neuroscience* **21**, 445–450 (2003).

186. Perez-Pouchoulen, M., VanRyzin, J. W. & McCarthy, M. M. Morphological and Phagocytic Profile of Microglia in the Developing Rat Cerebellum. *eneuro* **2**, ENEURO.0036-15.2015 (2015).

187. Wu, C. H., Wen, C. Y., Shieh, J. Y. & Ling, E. A. A quantitative and morphometric study of the transformation of amoeboid microglia into ramified microglia in the developing corpus callosum in rats. *J Anat* **181 (Pt 3)**, 423–430 (1992).

188. Guneykaya, D. *et al.* Transcriptional and Translational Differences of Microglia from Male and Female Brains. *Cell Reports* **24**, 2773-2783.e6 (2018).

189. Masuda, T. *et al.* Spatial and temporal heterogeneity of mouse and human microglia at single-cell resolution. *Nature* **566**, 388–392 (2019).

190. Hanamsagar, R. *et al.* Generation of a microglial developmental index in mice and in humans reveals a sex difference in maturation and immune reactivity. *Glia* **65**, 1504–1520 (2017).

191. Carvalho-Paulo, D. *et al.* Microglial Morphology Across Distantly Related Species: Phylogenetic, Environmental and Age Influences on Microglia Reactivity and Surveillance States. *Front. Immunol.* **12**, 683026 (2021).

192. Coomey, R., Stowell, R., Majewska, A. & Tropea, D. The Role of Microglia in Neurodevelopmental Disorders and their Therapeutics. *CTMC* **20**, 272–276 (2020).

193. Hristova, M. *et al.* Activation and deactivation of periventricular white matter phagocytes during postnatal mouse development. *Glia* **58**, 11–28 (2010).

194. Van Wageningen, T. A. *et al.* Viscoelastic properties of white and gray matter-derived microglia differentiate upon treatment with lipopolysaccharide but not upon treatment with myelin. *J Neuroinflammation* **18**, 83 (2021).

195. Rezaie, P. & Male, D. Colonisation of the developing human brain and spinal cord by microglia: a review. *Microsc Res Tech* **45**, 359–382 (1999).

196. Staszewski, O. & Hagemeyer, N. Unique microglia expression profile in developing white matter. *BMC Res Notes* **12**, 367 (2019).

197. Safaiyan, S. *et al.* White matter aging drives microglial diversity. *Neuron* **109**, 1100-1117.e10 (2021).

198. De Biase, L. M. & Bonci, A. Region-Specific Phenotypes of Microglia: The Role of Local Regulatory Cues. *Neuroscientist* **25**, 314–333 (2019).

199. van der Poel, M. *et al.* Transcriptional profiling of human microglia reveals grey-white matter heterogeneity and multiple sclerosis-associated changes. *Nat Commun* **10**, 1139 (2019).

200. Villa, A., Della Torre, S. & Maggi, A. Sexual differentiation of microglia. *Frontiers in Neuroendocrinology* **52**, 156–164 (2019).

201. Amor, S. *et al.* White matter microglia heterogeneity in the CNS. *Acta Neuropathol* **143**, 125–141 (2022).

202. Ferraro, M. B. Fuzzy k-Means: history and applications. *Econometrics and Statistics* **30**, 110–123 (2024).

203. Crapser, J. D. *et al.* Microglial depletion prevents extracellular matrix changes and striatal volume reduction in a model of Huntington's disease. *Brain* **143**, 266–288 (2020).

204. Crapser, J. D. *et al.* Microglia facilitate loss of perineuronal nets in the Alzheimer's disease brain. *EBioMedicine* **58**, 102919 (2020).

205. Gray, D. T. *et al.* Retrosplenial cortex microglia and perineuronal net densities are associated with memory impairment in aged rhesus macaques. *Cereb Cortex* **33**, 4626–4644 (2023).

206. Nguyen, P. T. *et al.* Microglial Remodeling of the Extracellular Matrix Promotes Synapse Plasticity. *Cell* **182**, 388-403.e15 (2020).

207. Wareham, L. K. & Calkins, D. J. Making tracks: microglia and the extracellular matrix. *Mol Neurodegeneration* **20**, 101 (2025).

208. Crapser, J. D., Arreola, M. A., Tsourmas, K. I. & Green, K. N. Microglia as hackers of the matrix: sculpting synapses and the extracellular space. *Cell Mol Immunol* **18**, 2472–2488 (2021).

209. Caliari, S. R. & Burdick, J. A. A practical guide to hydrogels for cell culture. *Nat Methods* **13**, 405–414 (2016).

210. Tibbitt, M. W. & Anseth, K. S. Hydrogels as extracellular matrix mimics for 3D cell culture. *Biotechnol Bioeng* **103**, 655–663 (2009).

211. Loebel, C. *et al.* Metabolic labeling of secreted matrix to investigate cell–material interactions in tissue engineering and mechanobiology. *Nat Protoc* **17**, 618–648 (2022).

212. Haw, R. T. Y. *et al.* A three-dimensional collagen construct to model lipopolysaccharide-induced activation of BV2 microglia. *J Neuroinflammation* **11**, 134 (2014).

213. Floryanzia, S. D. & Nance, E. Applications and Considerations for Microfluidic Systems To Model the Blood–Brain Barrier. *ACS Appl. Bio Mater.* **6**, 3617–3632 (2023).

214. Faisal, S. M. *et al.* The complex interactions between the cellular and non-cellular components of the brain tumor microenvironmental landscape and their therapeutic implications. *Front Oncol* **12**, 1005069 (2022).

215. Ucar, B. Natural biomaterials in brain repair: A focus on collagen. *Neurochemistry International* **146**, 105033 (2021).

216. Li, W., Shepherd, D. E. T. & Espino, D. M. Dynamic mechanical characterization and viscoelastic modeling of bovine brain tissue. *Journal of the Mechanical Behavior of Biomedical Materials* **114**, 104204 (2021).

217. Lee, H., Overall, C. M., McCulloch, C. A. & Sodek, J. A Critical Role for the Membrane-type 1 Matrix Metalloproteinase in Collagen Phagocytosis. *MBoC* **17**, 4812–4826 (2006).

218. He, X. *et al.* Extracellular matrix physical properties govern the diffusion of nanoparticles in tumor microenvironment. *Proc. Natl. Acad. Sci. U.S.A.* **120**, e2209260120 (2023).

219. Daniels, J. T. *et al.* Matrix Metalloproteinase Inhibition Modulates Fibroblast-Mediated Matrix Contraction and Collagen Production In Vitro. *Invest. Ophthalmol. Vis. Sci.* **44**, 1104 (2003).

220. Joseph, A. *et al.* Nanoparticle-microglial interaction in the ischemic brain is modulated by injury duration and treatment. *Bioengineering & Transla Med* **5**, e10175 (2020).

221. Butler, B., Renney, M., Bennett, K., Charpentier, G. & Nance, E. A rotenone organotypic whole hemisphere slice model of mitochondrial abnormalities in the neonatal brain. *J Biol Eng* **18**, 67 (2024).

222. Kolnik, S. *et al.* Vitamin E Decreases Cytotoxicity and Mitigates Inflammatory and Oxidative Stress Responses in a Ferret Organotypic Brain Slice Model of Neonatal Hypoxia-Ischemia. *Dev Neurosci* **44**, 233–245 (2022).

APPENDICES

Appendix A. Supplemental to Chapter 3

Feature	Model Abbreviation	Description	How it is determined
Alpha (α)	alpha	Exponent of the anomalous diffusion equation.	Non-linear least squares is used to fit raw MSD vs lag time (τ) data to the anomalous diffusion equation: $\mathrm{MSD} = 4D_{\mathrm{fit}}\tau^{\alpha}$
Effective diffusion coefficient (D_{fit})	D_fit	Coefficient of the anomalous diffusion equation	Non-linear least squares is used to fit raw MSD vs lag time (τ) data to the anomalous diffusion equation: $\mathrm{MSD} = 4D_{\mathrm{fit}}\tau^{\alpha}$
Kurtosis (K)	kurtosis	The fourth moment of the projected positions on the dominant eigenvector of the radius gyration tensor (T).	$\mathrm{K} = \frac{1}{N}\sum_{i=0}^{N-1}\left(\frac{\left(x_i^P - \overline{x^P}\right)^4}{\sigma_{x^P}^4}\right)$
Asymmetry1 (α)	asymmetry1	Characterizes the asymmetry of the trajectory. Asymmetry1 equals 0 for circularly symmetric trajectories and 1 for linear trajectories.	$\alpha = \frac{(\lambda_1^2 - \lambda_2^2)^2}{(\lambda_1^2 + \lambda_2^2)^2}$ where λ_1 and λ_2 are the eigenvalues of radius of gyration tensor T: $T = \begin{pmatrix} \frac{1}{N}\sum_{j=1}^{N}(x_j - \langle x\rangle)^2 & \frac{1}{N}\sum_{j=1}^{N}(x_j - \langle x\rangle)(y_j - \langle y\rangle) \\ \frac{1}{N}\sum_{j=1}^{N}(x_j - \langle x\rangle)(y_j - \langle y\rangle) & \frac{1}{N}\sum_{j=1}^{N}(y_j - \langle y\rangle)^2 \end{pmatrix}$
Asymmetry2 (α_2)	asymmetry2	The ratio of the smaller to larger principal radius of gyration.	$a_2 = \frac{\lambda_2}{\lambda_1}$
Asymmetry3 (α_3)	asymmetry3	An asymmetry feature that accounts for non-cylindrically symmetric point distributions.	$a_3 = -\log\left(1 - \frac{(\lambda_1 - \lambda_2)^2}{2(\lambda_1 + \lambda_2)^2}\right)$
Aspect ratio (AR)	AR	The ratio of the long and short side of the trajectory's minimum bounding rectangle. Perfectly symmetric trajectories have an aspect ratio of 1, and aspect ratio increases as trajectories become more elongated.	$AR = \begin{cases} \frac{\lvert x_{max} - x_{min}\rvert}{\lvert y_{max} - y_{min}\rvert}, & \lvert y_{max} - y_{min}\rvert < \lvert x_{max} - x_{min}\rvert \\ \frac{\lvert y_{max} - y_{min}\rvert}{\lvert x_{max} - x_{min}\rvert}, & \lvert y_{max} - y_{min}\rvert \geq \lvert x_{max} - x_{min}\rvert \end{cases}$
Elongation	elongation	An estimation of amount of extension of the trajectory from its centroid.	$\mathrm{Elongation} = 1 - \frac{1}{\mathrm{AR}}$
Boundedness (B)	boundedness	Boundedness quantifies how much a particle with diffusion coefficient D_{eff} is restricted by a circular confinement of radius r when diffusing for a period of time $N\Delta\tau$.	$B = \frac{D_{\mathrm{eff}}N\Delta t}{r^2}$
Fractal Dimension (D_f)	fractal_dim	Fractal dimension is a measure of how "complicated" a self similar figure is.	$D_f = \frac{\log(N)}{\log(NdL^{-1})}$
Trappedness (ρ_t)	trappedness	The probability (ρ_t) that a particle with duffusion coefficient D_{eff} is trapped in a region (r_0) for a period of time.	$p_t = 1 - \exp\left(0.2048 - 0.25117\frac{DeffN\Delta t}{r_0^2}\right)$

Feature	Model Abbreviation	Description	How it is determined
Efficiency (E)	efficiency	The ratio of the squared net displacement to the sum of step lengths.	$E = \frac{(x_{N-1} - x_0)^2 + (y_{N-1} - y_0)^2}{\sum_{i=1}^{N-1}((x_i - x_{i-1})^2 + (y_i - y_{i-1})^2)}$
Straightness (S)	straightness	The ratio of the net displacement to the sum of step lengths.	$S = \frac{\sqrt{(x_{N-1} - x_0)^2 + (y_{N-1} - y_0)^2}}{\sum_{i=1}^{N}((x_i - x_{i-1})^2 + (y_i - y_{i-1})^2)}$
MSD Ratio (MSD_{n_1,n_2})	MSD_ratio	MSD ratio characterizes the shape of the MSD curve. For Brownian motion, it is 0; For restricted motion it is < 0; For directed motion it is > 0.	$MSD_{n1,n2} = \frac{MSD_{n1}}{MSD_{n2}} - \frac{n1}{n2}$
Frames	frames	The total number of frames the trajectory spans.	Frames = N
Mean Turning Angle (θ_{mean})	angle_mean	The trajectory mean of the turning angle which is the counterclockwise angle from one point to another	$\frac{1}{N}\sum_{i=1}^{N}\theta_{i,i+1}$
Mean Turning Angle Magnitude (θ_{mag})	angle_mag_mean	The trajectory mean of the magnitude turning angle which is the counterclockwise angle from one point to another	$\frac{1}{N}\sum_{i=1}^{N}\lvert\theta_{i,i+1}\rvert$
Turning Angle Variance (θ_{var})	angle_var	The trajectory variance of the turning angle which is the counterclockwise angle from one point to another	$\frac{\frac{1}{N}\sum_{i=1}^{N}(\theta_{i,i+1} - \bar{\theta})^2}{N}$
Total Distance (d_{total})	dist_tot	Total distance particle travels throughout trajectory	$d_{\text{total}} = \sum_{i=1}^{N}\sqrt{(x_i - x_{i-1})^2 + (y_i - y_{i-1})^2}$
Net Distance (d_{net})	dist_net	Net distance traveled throughout trajectory	$d_{\text{net}} = \sqrt{(x_N - x_0)^2 + (y_N - y_0)^2}$
Progression	progression	The ratio of the net distance traveled, and the total distance traveled	$progression = \frac{d_{net}}{d_{total}}$
Effective Diffusion Coefficient 1	Deff1	Effective diffusion coefficient at 0.33 s.	$Deff1 = \frac{MSD_{\tau=0.1}}{4 * 0.1}$
Effective Diffusion Coefficient 2	Deff2	Effective diffusion coefficient at 3.3 s.	$Deff2 = \frac{MSD_{\tau=1}}{4 * 1}$
Mean values were calculated based on surrounding datapoints for alpha, D_fit, asymmetry1, asymmetry2, asymmetry3, AR, elongation, boundedness, fractal_dim, trappedness, efficiency, straightness, MSD_ratio, Deff1, and Deff2			

MSD: mean squared displacement
N: number of frames
σ_x^p: standard deviation of the projected 2D positions
λ_1, λ_2: eigenvalues of radius of gyration tensor
D_{eff}: effective diffusion coefficient
r: radius of circular confinement
n: frame number
r_0: radius of trapped region
I_{Back}: average background pixel intensity
τ: lag time
x^p: projected 2D position
T: gyration tensor
$\langle x \rangle, \langle y \rangle$: average x and y location
$\Delta\tau$: inverse of frame rate
d: largest distance between any two positions
L: total length (sum over all steplengths) of trajectory
σ_I: standard deviation of pixel intensities

Appendix A. 1 A complete list of all 39 trajectory features calculated by the diff_classifier Python package.

Included for each feature is a brief description and how it is determined. Additional documentation can be found in the TraJ GitHub repository (https://github.com/thorstenwagner/TraJ.git).

	Age	Region	Treatment	OGD
max_depth	4	4	5	5
eta	0.1	0.005	0.05	0.01
min_child_wieght	1	0	0	10
gamma	1.0	5.0	2.0	0.2
subsample	0.5	0.6	0.15	0.6
colsample_bytree	0.6	0.7	0.8	0.9
boost_rounds	804	1157	57	1004

Appendix A. 2 Optimal hyperparameters for XGBoost models

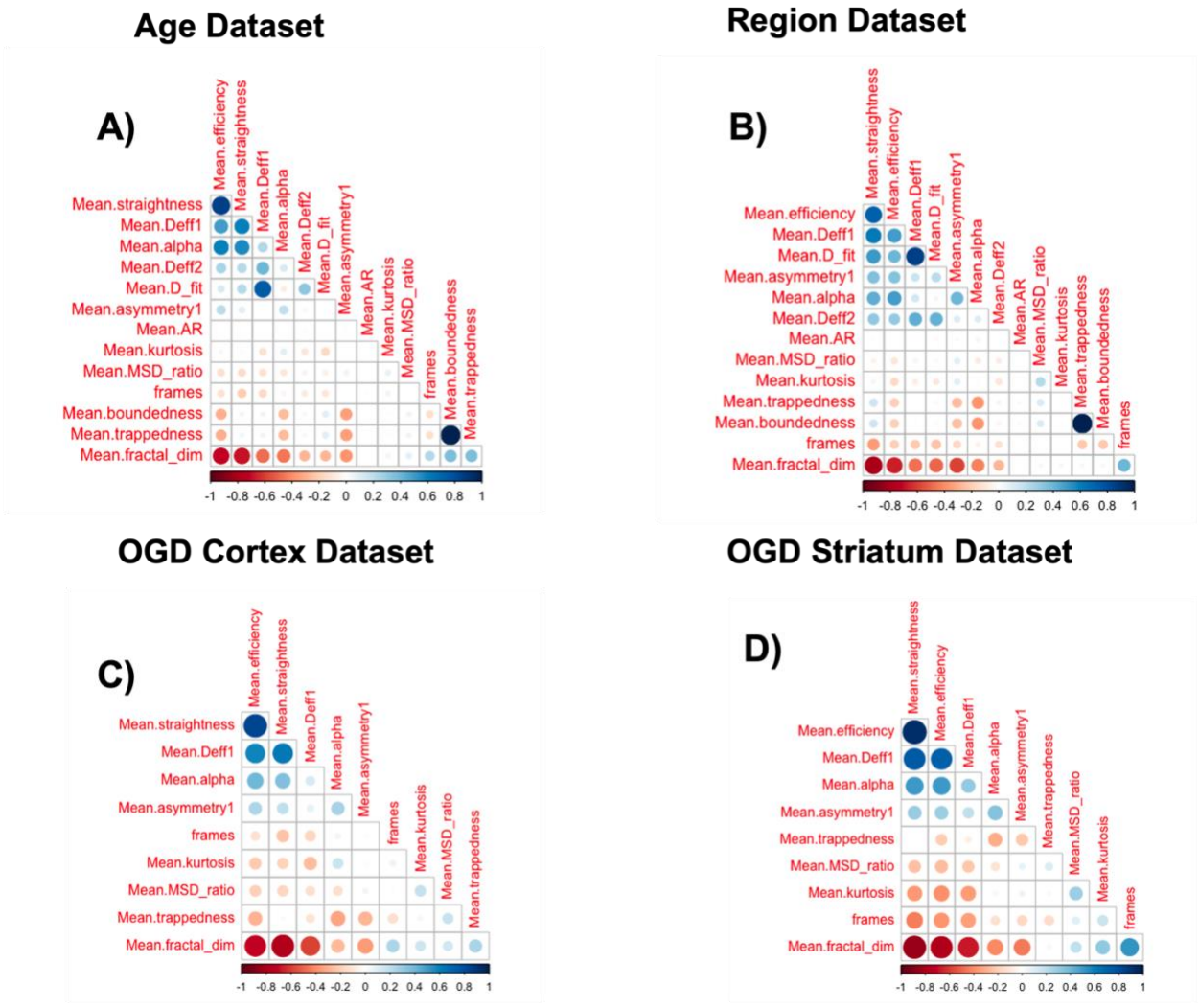

Appendix A. 3 Correlation of all statistical and geometric features used in XGBoost model

A) Correlation plot of features used to train XGBoost model on Age dataset. **B)** Correlation plot of features used to train XGBoost model on Region dataset. **C)** Correlation plot of features used to train XGBoost model on OGD treated data from cortex. **D)** Correlation plot of features used to train XGBoost model on OGD treated data from striatum. Frames feature is the number of video frames the trajectory spanned.

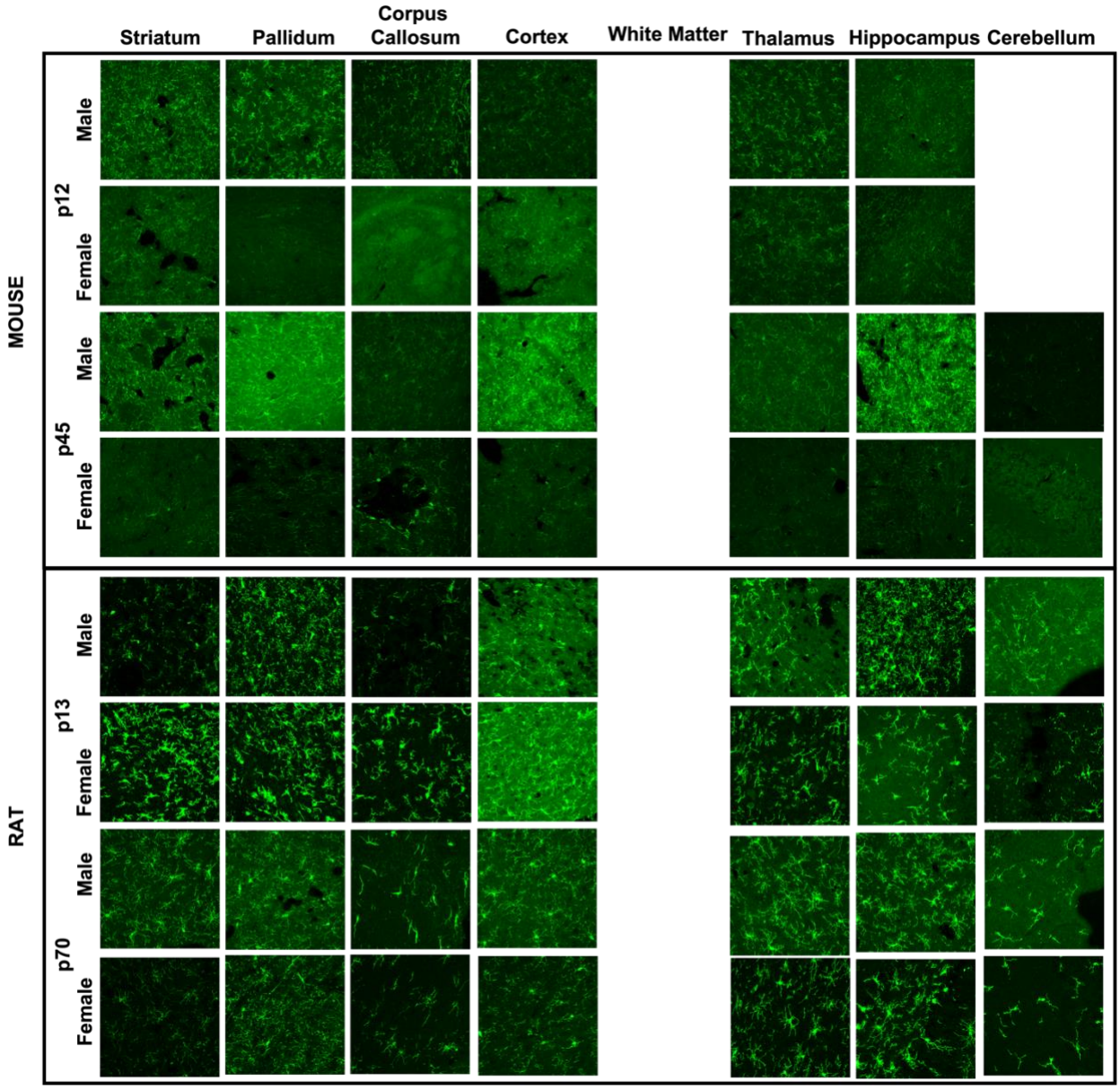

Appendix B. 1 Representative visuals of the mouse and rat models

Representative images of Iba1 stained microglia from the mouse striatum, pallidum, corpus callosum, cortex, thalamus, and hippocampus are displayed for both the male and female animals at human term equivalent (p12 and p13) and human sexual maturity equivalent (p45 and p70) ages.

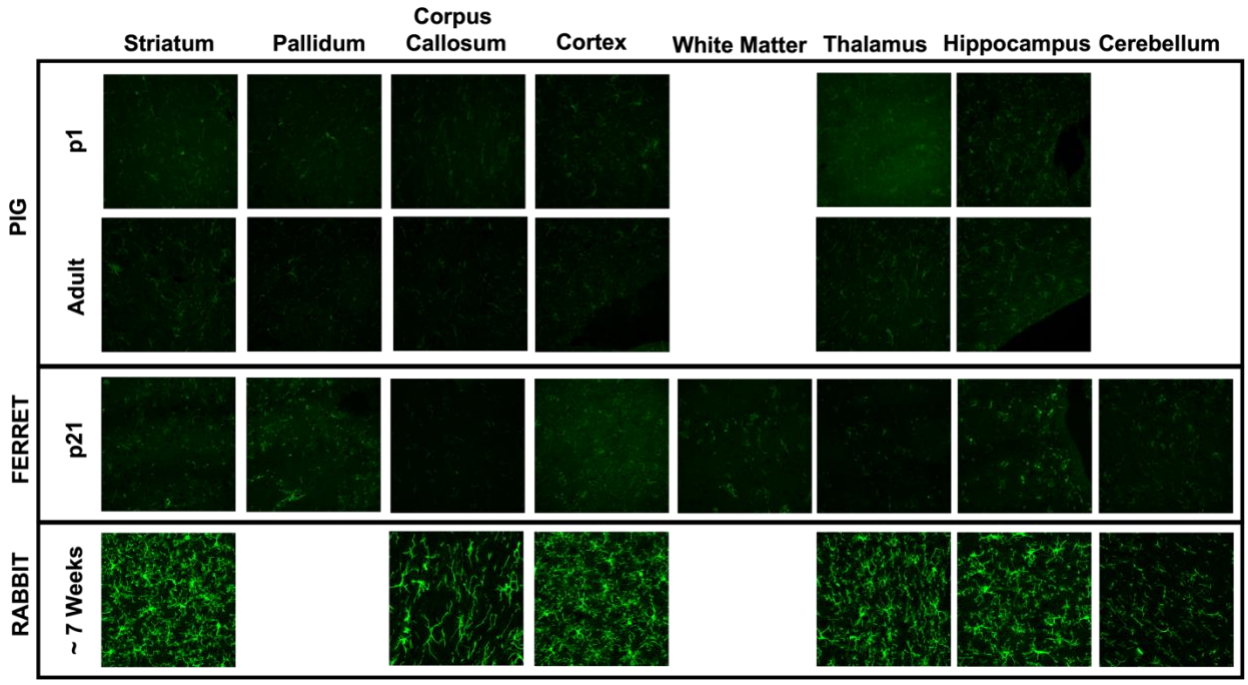

Appendix B. 2 Representative visuals from other animal models

Representative images of Iba1+ microglia are displayed from the pig at human term equivalent and adult animals in the striatum, pallidum, corpus callosum, cortex, thalamus, and hippocampus. For the ferret, representative images are displayed for the striatum, pallidum, corpus callosum, grey and white matter, thalamus, hippocampus, and cerebellum at p21. For the approximately seven-week-old rabbits, images are displayed for the striatum, corpus callosum, cortex thalamus, and hippocampus.